NASA
SPACE VEHICLE
DESIGN CRITERIA
(ENVIRONMENT)

NASA SP-8116

THE EARTH'S TRAPPED RADIATION BELTS

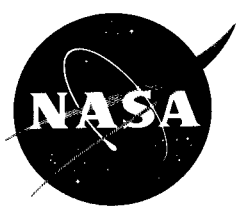

MARCH 1975

NATIONAL AERONAUTICS AND SPACE ADMINISTRATION

FOREWORD

NASA experience has indicated a need for uniform criteria for the design of space vehicles. Accordingly, criteria have been developed in the following areas of technology:

Environment
Structures
Guidance and Control
Chemical Propulsion

Individual components of this work are issued as separate monographs as soon as they are completed. A list of all monographs published in this series can be found on the last pages of this monograph.

These monographs are to be regarded as guides to design and not as NASA requirements except as may be specified in formal project specifications. It is expected, however, that the monographs will be used to develop requirements for specific projects and be cited as the applicable documents in mission studies, or in contracts for the design and development of space vehicle systems.

This monograph was prepared for NASA under the cognizance of the NASA Goddard Space Flight Center with Scott A. Mills as program coordinator. Principal authors were Mr. Richard B. Noll of Aerospace Systems, Inc. and Dr. Michael B. McElroy of Harvard University. The Technical Director was Mr. John Zvara of Aerospace Systems, Inc.

Comments concerning the technical content of these monographs will be welcomed by the National Aeronautics and Space Administration, Goddard Space Flight Center, Systems Reliability Directorate, Greenbelt, Maryland 20771.

March 1975

For sale by the National Technical Information Service
Springfield, Virginia 22151
Price — $4.75

CONTENTS

THE EARTH'S TRAPPED RADIATION BELTS

1. INTRODUCTION

Spacecraft operating in the Earth's trapped radiation belts are subject to damaging effects of charged particles. These particles include protons, electrons, alpha particles (helium nuclei) and heavier nuclei. The effects include degradation of material properties and component performance which can result in reduced performance or failure of spacecraft systems and experiments; and a hazardous radiation environment for manned spacecraft. Hence, mission planners, spacecraft designers and experimenters should consider the effects of the charged particle environment.

Radiation damage from the charged particle environment can be reduced significantly, or eliminated, if the spacecraft is designed so that the crew and radiation sensitive materials and components are housed within an area where the spacecraft structure and major components provide ample shielding in all directions. Because radiation damage is cumulative, damage can be minimized by proper selection of orbits and trajectories to avoid long periods of operation in areas of dense charged particle populations. The Van Allen trapped radiation belts constitute the severest near-Earth charged particle environment and, therefore, are generally avoided if the spacecraft is radiation sensitive and cannot pass quickly through these belts.

This monograph discusses the near-Earth charged particle environment and provides models of the trapped radiation belts that are based on in-situ data obtained from spacecraft. For regions inside the magnetosphere but not within the trapped radiation belts, conservative design parameters can be obtained from the design criteria monograph being prepared on interplanetary charged particles.* More information on the solar proton component in these regions can be obtained from reference 1 which gives the amount that the interplanetary (or solar) proton flux should be reduced for different circular orbits to account for magnetospheric shielding.

Besides the design criteria monograph on interplanetary charged particles being prepared, another related monograph discusses the effects of radiation on materials (ref. 2). Monographs also describe the Earth's magnetic field (ref. 3) and other Earth, planetary, and

*NASA SP-8118, March, 1975.

solar environments as well as facets of space vehicle technology. All titles in the series are listed at the end of this monograph.

2. STATE OF THE ART

Understanding and knowledge of the outer regions of Earth's environment has changed rapidly since the discovery of the Van Allen radiation belts. The Earth has been found to be a magnetized planet traveling through an interplanetary medium that is pervaded by a weakly magnetized plasma of solar origin (solar wind). The solar wind incident on the side of the Earth facing the sun compresses the Earth's magnetic field in such a manner that the interplanetary field is detectable at distances as small as 12 Earth radii (R_E). In the antisolar direction, the terrestrial field is transported by the solar wind to large distances, as depicted in figure 1.

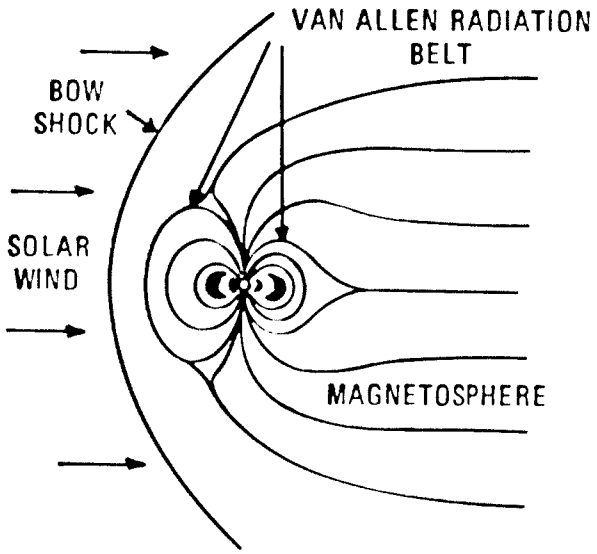

Figure 1.—Interaction of Earth's magnetic field and solar wind.

Close to the Earth, the magnetic field behaves approximately like a dipole, that is, the field lines are closed, and charged particles can be magnetically trapped. Van Allen's discovery of the trapped radiation belts (refs. 4 and 5) was unexpected, however, because knowledge of the magnetosphere was then limited. The spatial distribution of geomagnetically trapped electrons is indicated schematically in figure 2. To a first order, it may be assumed that the high density zones exhibit axial symmetry about the magnetic axis of the Earth.

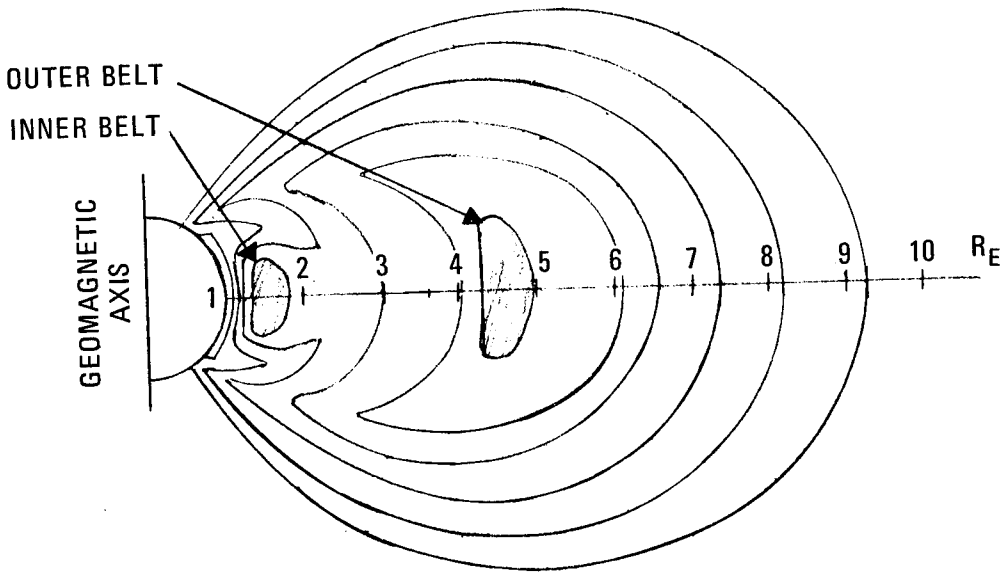

Figure 2.—Van Allen trapped radiation belts (refs. 6 and 7).

Considerable effort has been made to determine the nature of the trapped radiation belts, the solar wind, and the magnetosphere; their relationship with one another; and their relationship to galactic phenomena. These efforts are reviewed in references 8 to 11. Before presenting models of the charged particles in the belts, the general environment within the magnetosphere will be discussed.

2.1 Charged Particle Zones

2.1.1 Magnetosphere

The charged particle environment of the Earth lies within the magnetosphere as shown in figure 3. The magnetosphere is formed when the supersonic solar wind impinges on the Earth's magnetic field. (The solar wind is an electrically neutral plasma consisting mostly of protons and electrons that continuously streams radially from the Sun.) As a result of the interaction, a shock wave is formed that compresses the magnetic field on the solar side and deflects the flow of solar wind around the magnetosphere (e.g., refs. 12 and 13). Variations in the configuration occur because of changing orientation of the Earth's magnetic axis in respect to the solar wind as the Earth rotates and revolves around the Sun.

The component elements of the magnetosphere are discussed in references 3, 9, 14 and 15; brief descriptions follow.

- Bow Shock – the outermost boundary of the magnetosphere created by the magnetogasdynamic interaction of the solar wind and the geomagnetic field.

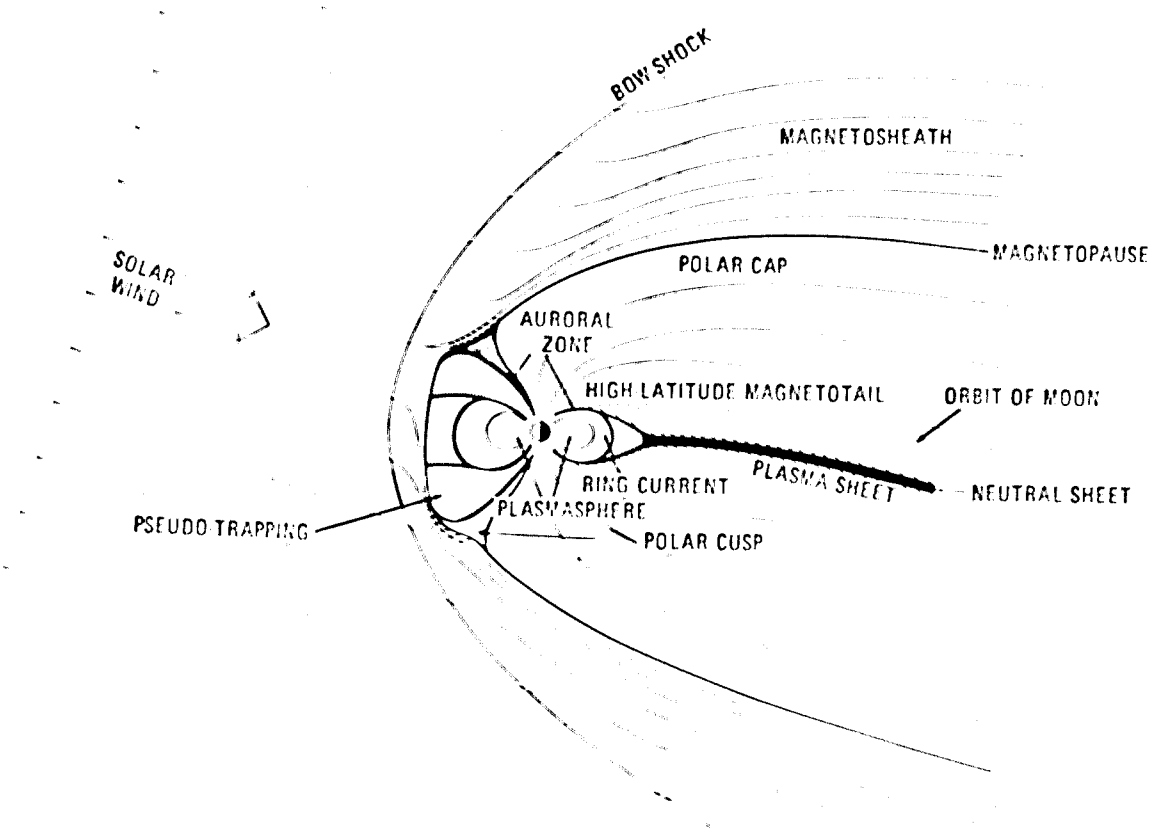

Figure 3.–Regions of the magnetosphere shown in the noon-midnight meridian plane.

- Magnetosheath – the transition zone in which the interplanetary field and the solar wind are deflected after passing through the bow shock.
- Magnetopause – the boundary layer that separates the relatively strong geomagnetic field from the magnetosheath.
- Polar Cusp – regions of the day-side, high-latitude magnetopause through which the magnetosheath plasma has direct access to the magnetosphere.
- Magnetotail – the region where the geomagnetic field lines emanating from the high-latitude, mainly night-time regions of Earth are swept back in the antisolar region.
- Plasma sheet – a region imbedded in the magnetotail that contains low energy electrons and protons.
- Neutral sheet – a region within the magnetotail where abrupt reversal of the magnetic field from the solar to the antisolar direction occurs and in which magnetic intensity decreases to a low value.
- Polar cap – a region about 15 degrees latitude in width that is centered about 5 degrees south of the geomagnetic pole in the antisolar direction. Only very low energy particles from the polar cusp are precipitated into the polar cap except during times when energetic solar cosmic rays are in the interplanetary medium.

- Auroral zone – a high latitude band about 10 to 15 degrees latitude in width in which electrons and protons of energies up to tens of keV from the outer radiation belt, the ring current, and the plasma sheet are precipitated into the atmosphere.

2.1.2 Areas Of Charged Particles

Charged particles, principally electrons and protons introduced at the merging of the interplanetary field and the solar wind with the geomagnetic field, are distributed throughout the magnetosphere. The distributions vary as the magnetosphere changes in response to changes in the interplanetary medium. However, the particle distributions can be discussed on the basis of several zones of the magnetosphere, each of which exhibits varying capability of controlling the charged particle distribution. These zones, depicted in figures 3 and 4, are:

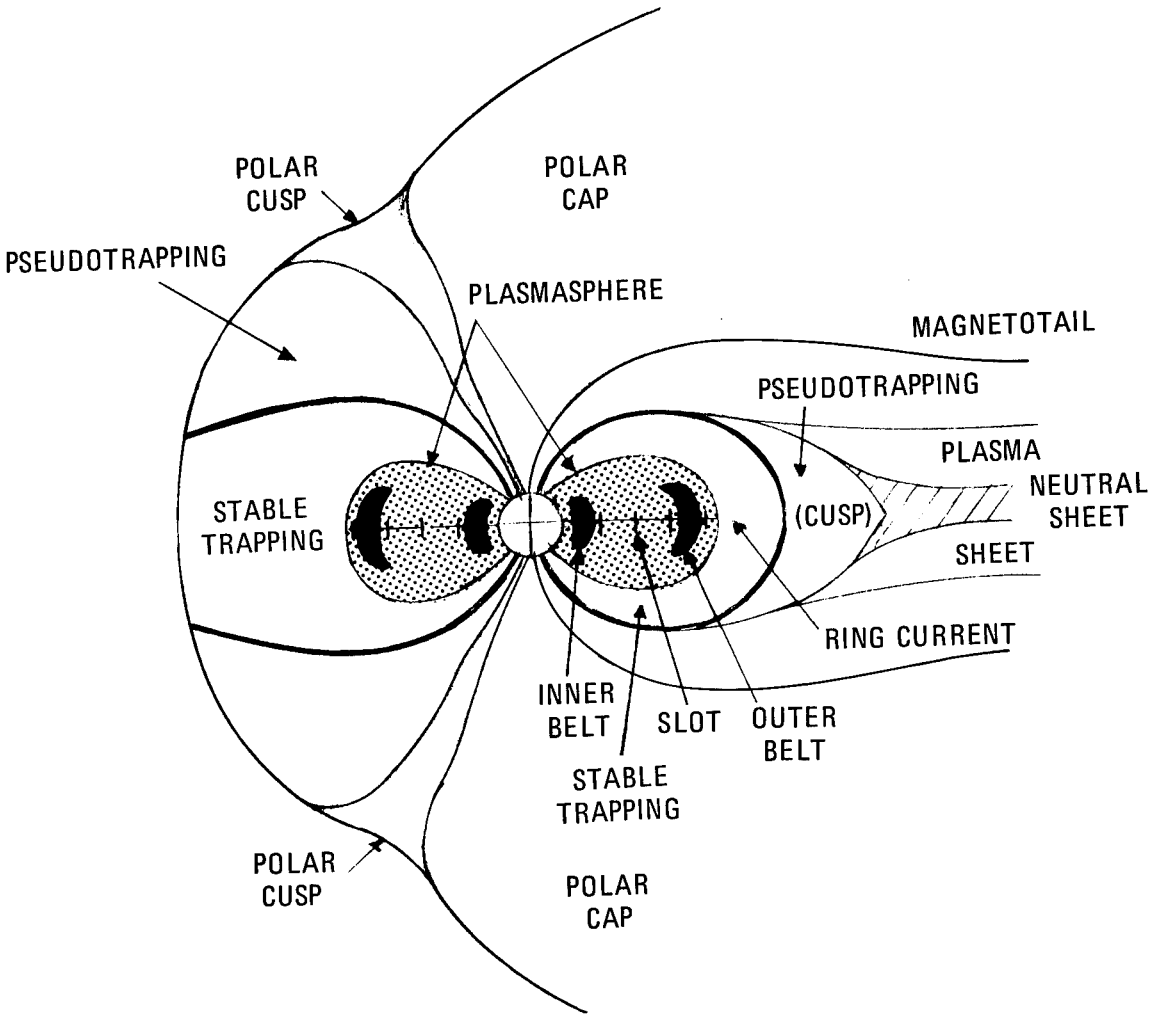

Figure 4.—Trapping regions in the magnetosphere.

- Stable trapping
  - Inner radiation belt
  - Electron slot
  - Outer radiation belt
- Pseudotrapping
- Plasmasphere
- Polar cusp
- Polar cap
- Magnetotail

Of primary importance to spacecraft design are the inner and outer trapped radiation belts. From maximum values in the belts, the electron flux decreases as one moves towards the slot region between the belts where the flux reaches minimum values. The belts lie within the magnetosphere where stable trapping of charged particles occurs, as discussed in section 2.2. As shown in figure 4, the stable trapping regions are adjacent to the pseudotrapping regions. The term, Van Allen trapped radiation belts, is often used to refer to both the stable- and pseudotrapped regions, but in this monograph "belts" will refer to the inner and outer belts which contain charged particle populations and energies that are of greatest concern in spacecraft design. The non-trapping regions, i.e., polar cap regions, polar cusps, and magnetotail, are discussed in references 16 and 17 and briefly described in the following paragraphs.

2.1.2.1 Slot Region

Radial profiles of electron flux measured by the OGO 1 and 3 satellites such as shown in figure 5 (ref. 18) indicate a minimum exists at all energies between 2 and 3 Earth radii at the equator. This region of minimum flux is called the slot region. The position of the minimum is a function of solar cycle activity. It should be noted that the slot applies only to electrons because low energy protons of $0.1 < E < 4$ MeV reach a maximum flux in this region.

2.1.2.2 Pseudotrapping Region

The pseudotrapping regions are shown in figure 4. The noon (day or sunward) side areas are known as the skirt and the midnight (night or antisolar) side area is known as the cusp (not to be confused with the polar cusp). Particle populations in the pseudotrapping region are large, such as shown in figure 6, and include low energy electrons ($E > 200$ eV) as detected by the Soviet Luna spacecraft (ref. 20). Reference 19 is an earlier report on the large particle populations in these regions (fig. 6). Reference 20 includes many later results and provides information on low energy electrons ($E > 200$ eV).

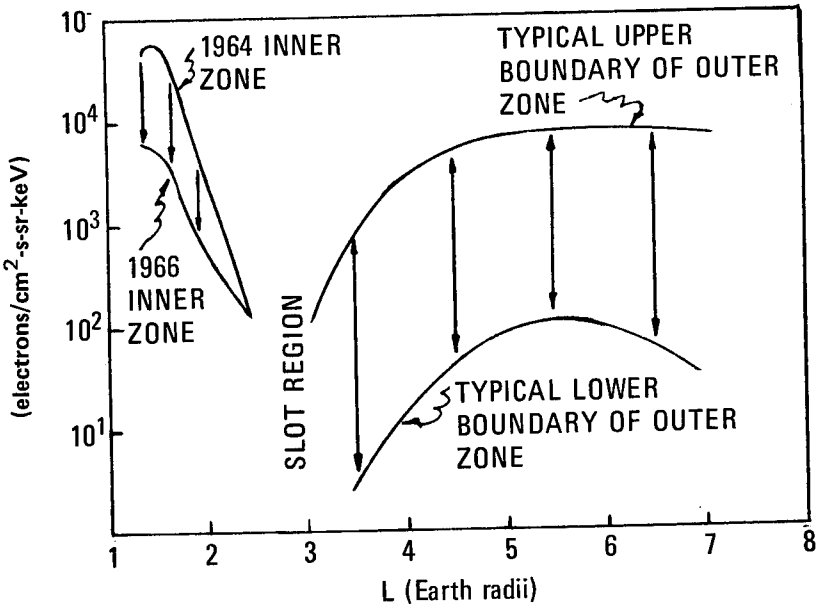

Figure 5.—Electron flux profile (260-690 keV) (ref 18) (For a given magnetic field line, the value of L is given by the distance in Earth radii from the center of the Earth to the point at which the field line intersects the geomagnetic equator.)

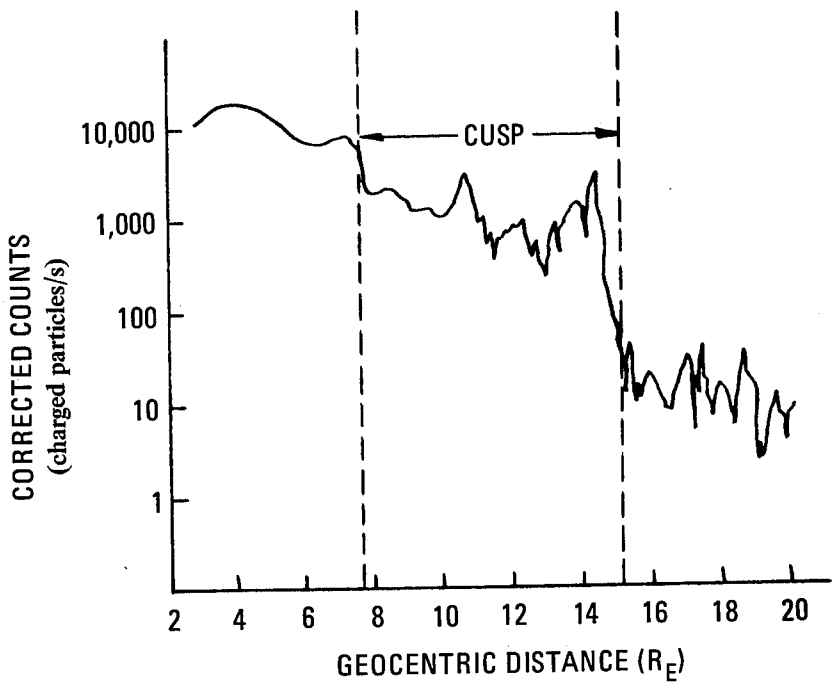

Figure 6.—Particle density in pseudotrapping (cusp) region (ref. 19).

2.1.2.3 Plasmasphere

The plasmasphere (refs. 20 and 21) lies within the region of trapped radiation (fig. 4) and contains a low energy (~ 1 eV) plasma. This cold particle population can be very important in determining the degree to which wave growth and the subsequent loss of energetic particles through pitch angle diffusion can occur. The fluxes are extremely variable in time, but their magnitude sometimes exceeds those of the stable fluxes of high energy particles.

The outer plasmasphere consists of about 99% H^+ ions and about 1% He^+ ions with only a trace of O^+ present. Data from OGO 5 spacecraft indicated an upflow of ions from the ionosphere (ref. 21). The plasmasphere terminates abruptly between L = 3 and L = 5 at the plasmapause. Location of the plasmapause varies with magnetic storm events; it moves outward during the recovery phase.

2.1.2.4 Polar Cusp

The polar cusp region is identified in figure 4. Here, the solar wind plasma can penetrate to low altitudes (ref. 22) and plasma sheet protons gain access to the magnetospheric field lines (ref. 14). The proton and electron differential energy spectrums within several Earth radii are identical to those observed within the magnetosheath, e.g., figure 7. The location of and physical processes that occur in the polar cusps depend on the north-south component of the interplanetary magnetic field (ref. 23). However, during periods of relative magnetic quiescence, the intersection of the polar cusp and the auroral zone is located at a latitude of about 79° (ref. 14).

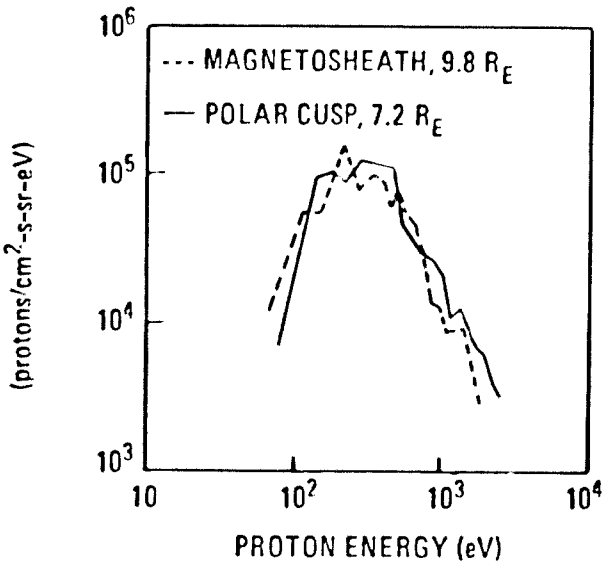

Figure 7.—Proton differential energy spectrums in polar cusp and magnetosheath (ref. 14).

2.1.2.5 Polar Cap

The polar cap regions receive fluxes of charged particles from the interplanetary fields and by leakage from the polar cusp. Solar electrons and protons have access to closed field lines at latitudes that can vary with geomagnetic conditions (ref. 24). Typical high-latitude solar proton and electron flux profiles are shown in figure 8 which also indicates diurnal variation of solar proton flux at cutoff (abrupt decrease in flux near 65°). The proton fluxes near cutoff on the night side are only slightly higher than the average fluxes, whereas on the day side the fluxes at the cutoff are significantly higher than the average fluxes. Solar electron spatial distributions are generally uniform.

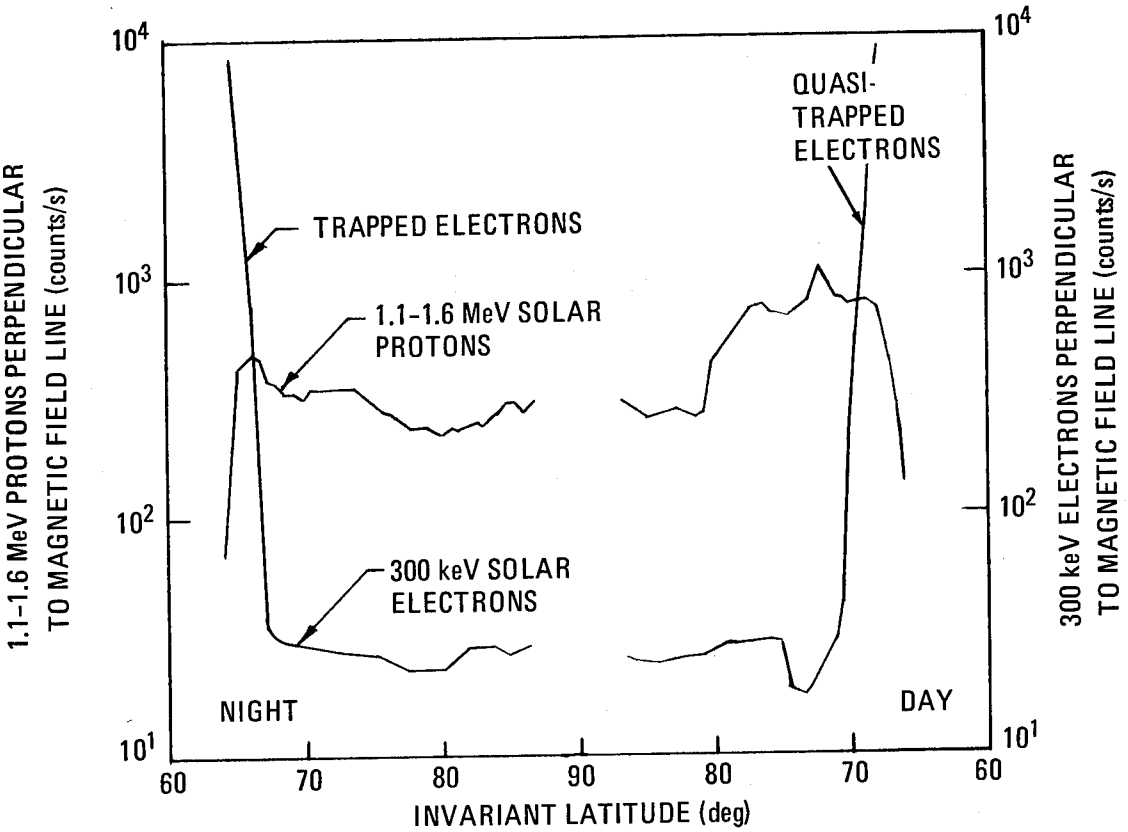

Figure 8.—Polar cap profiles of solar proton and electron fluxes at 4,000 km (ref. 24).

Solar proton flux measurements over the polar caps have been observed to exhibit asymmetry between the north and south polar regions (ref. 24). There is evidence that the asymmetry may be related to anisotropies in the interplanetary particle flux. Solar electron fluxes, on the other hand, have been observed to have equal intensities over both polar caps (ref. 25).

2.1.2.6 Auroral Zone

The auroral zone is the low altitude portion of the auroral region which lies between about 60 and 80° latitude. The auroral region contains the polar cusps, ring current, earthward termination of the plasma sheet, outer edge of the plasmapause, and the outer radiation belt.

Auroras and polar substorms in the high latitude regions give evidence of precipitation of electrons and protons from the auroral regions. Auroras are caused by the precipitation of particles and by convection induced by the solar wind (ref. 26). Present evidence shows that within factors of approximately 2 to 3, sufficient energy fluxes of electrons with appropriate energies are available in the near-Earth plasma sheet for producing auroras by magnetospheric convection without the need for other acceleration mechanisms (refs. 27, 28 and 29). Precipitation of ring current protons in a turbulent diffusion process just inside the plasmapause has been considered as a primary source of particles in the auroral zone during magnetic storms (ref. 30). However, magnetospheric convection is felt to be the most efficient proton source.

2.1.2.7 Magnetotail

Charged particle fluxes measured in the magnetotail generally lie within a few Earth radii of the neutral sheet (fig. 3). This region of the magnetotail constitutes a plasma sheet which is present almost continuously and extends from the night-side boundary of the radiation belt outward to distances beyond the orbit of the moon (ref. 15). The electron spectrum in the plasma sheet is quasi-thermal with a high energy tail (ref. 17). The average electron energy is 0.6 keV but varies from 0.1 to 10 keV. Omnidirectional fluxes > 100 eV extend to 10^9 cm^{-2} $-s^{-1}$ and the particle density ranges from 0.1 to 3 cm^{-3} with an average value of 0.5. The energy density of the protons in the plasma sheet exceeds that of electrons by a factor of about 10. The average proton energy is 5 keV and ranges from 1 to 20 keV. The energy density is greatest near the neutral sheet.

Measurement of charged particle populations with energies above the normal range results in the appearance of apparent islands of flux such as shown in figure 9. These islands, however, are dependent on the distance from neutral sheet and not on the radial distance (ref. 31) and represent an increase in the energy of the lower energy particles that are always present (refs. 15 and 31). Vela satellite results showed that a marked decrease of the particle energy density is a regular feature at about 17 R_E in the plasma sheet during the development phase of a magnetic substorm (ref. 21).

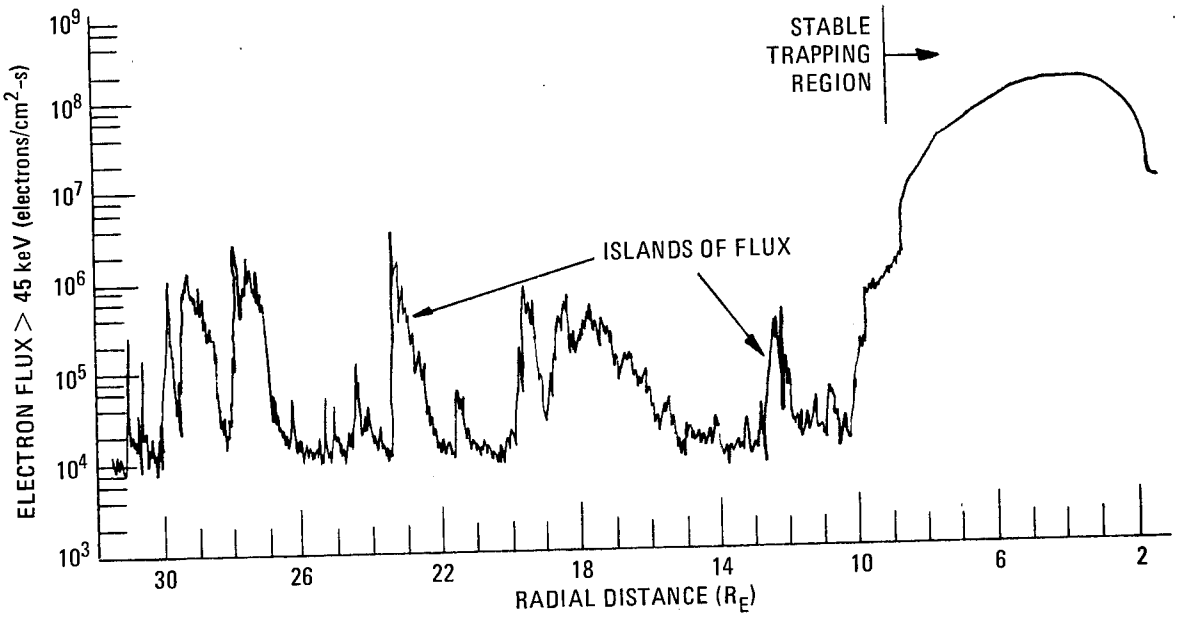

Figure 9.—Electron flux in the magnetotail (ref. 16).

2.2 Investigation Of Trapped Radiation Belts

2.2.1 Discovery

Before artificial satellites were placed in orbit, charged particle data obtained from Earth- and balloon-launched rockets indicated populations expected from cosmic radiation although laboratory experiments had indicated that the populations could be enhanced by charged particles trapped in the Earth's magnetic field. Geiger counter data from the first US satellites, Explorer 1 and 3, showed counting rates that exceeded the normal cosmic-ray count by a factor of 1,000 or more at altitudes between 500 and 2,000 km. The experiment team leader, Dr. James Van Allen, interpreted this result as evidence of a large flux of charged particles trapped in the Earth's magnetic field (ref. 5). Analysis of the Explorer 1 data (ref. 32) showed that the counting rate was a function of magnetic field intensity and thus indicated that the particles were charged and controlled by the magnetic field. In addition, the charged particle flux appeared to vary roughly in inverse proportion to atmospheric density. Thus, the combination of atmospheric density at the lower edge and the magnetic field strength at the outer edge constrained the charged particles into a radiation belt. Subsequent analysis of data recorded by the USSR Sputnik 2 and 3 satellites confirmed the existence of the radiation belt.

Geiger counters were also flown on Explorer 4. Data from this satellite were analyzed in conjunction with data obtained later from Pioneer 3 which made measurements to a distance of 107,400 km from the Earth. The results of the data analysis (ref. 33) revealed that the radiation belt actually consists of an inner and an outer zone (fig. 2). Data on the outer belt from USSR Space Rocket I and II showed very few high energy particles and also showed variation of flux and energy spectrum with time (ref. 34).

In addition to the time variations in the outer belt, it is now known that spatial distribution of the belts depends on the type and energy of the charged particles. Figure 10 from reference 8 shows typical spatial distributions for different energies of protons and electrons.

The inner radiation belt extends roughly from L = 1.2 to L = 2.5 and the outer belt from L = 3.0 to L = 8.0. (For a given magnetic field line, the value of L is given by the distance in Earth radii from the center of the Earth to the point at which the field line intersects the geomagnetic equator.) Protons and electrons dominate the charged particle effects. The radiation belt configuration and extent depend on which particles are discussed, their energy range, geographic location, and epoch. Data for the inner belt have been obtained from rocket flights and orbital spacecraft, and for the outer belt from orbital and deep-space spacecraft. These investigations have determined the characteristics of the natural proton populations; however, information concerning electron behavior in the inner belt has been highly colored by atmospheric nuclear detonations.

2.2.2 Inner Radiation Belt

The motion of the charged particles and configuration of the inner belt relate to the dipole nature of the Earth's magnetic field that causes the lines of magnetic field strength to vary with altitude as a function of longitude and latitude. As seen in figure 11, the field strength lines reach a low point at about 30°S latitude over the South Atlantic that causes a dip in the inner radiation belt. This dip of the inner belt is termed the South Atlantic or South American anomaly.

2.2.2.1 Protons

Charged particle populations measured by nuclear emulsions on Atlas rockets were identified as protons (ref. 35). Inner belt proton energy spectra from these experiments and subsequent tests are shown in figure 12. The high energy proton population is stable except for variations that are a function of the solar cycle variations in the atmosphere (refs. 36 and 37). For example, gradual changes for $L < 1.6$ were observed on Explorer 7 (ref. 38). Similarly, observations from Satellite 1963 38C (ref. 39) indicated that protons above 25 MeV were extremely stable at $L \leq 1.8$ and that protons between 8.2 and 25 MeV responded only to exceptional magnetic disturbances.

The radial variation of the proton population is shown by figure 13 (ref. 40). For $L < 1.6$, the energy spectra are similar to that of figure 12; however, for $L > 1.6$, a large flux of protons with energy $E < 30$ MeV is observed. Spatial distribution, both radially and latitudinally, of proton flux for $40 < E < 110$ MeV obtained on Explorer 15 is shown in figure 14 (ref. 41). The influence of the low energy component is not included in this energy band. The spatial distribution measured in 1963 showed two peaks, one near L = 1.5 and the other near L = 2.2. However, by 1965 the peak over L = 2.2 had begun to diffuse inward and by 1968 had disappeared (ref. 17).

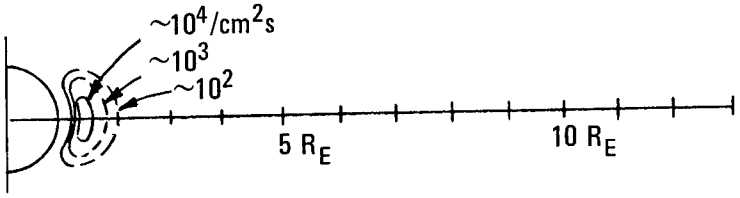

a. PROTON FLUX, E > 30 MeV

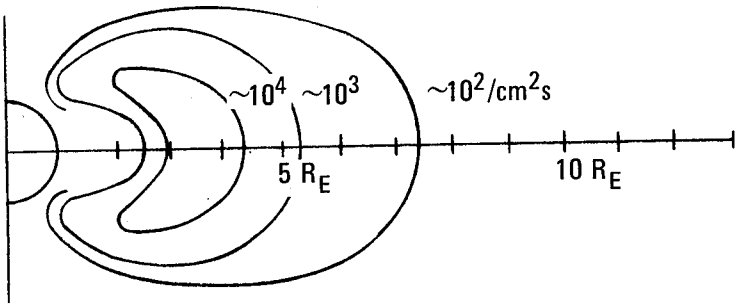

b. ELECTRON FLUX, E > 1.6 MeV

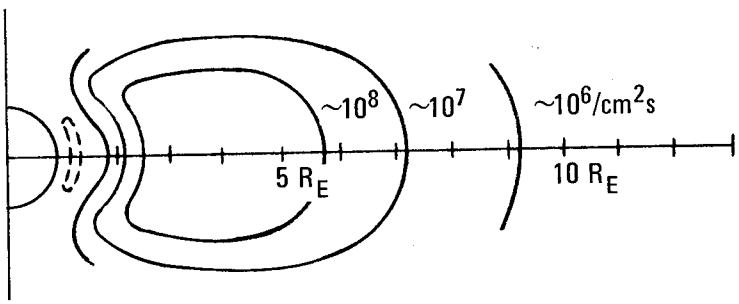

c. PROTON FLUX, 1.0 < E < 5 MeV

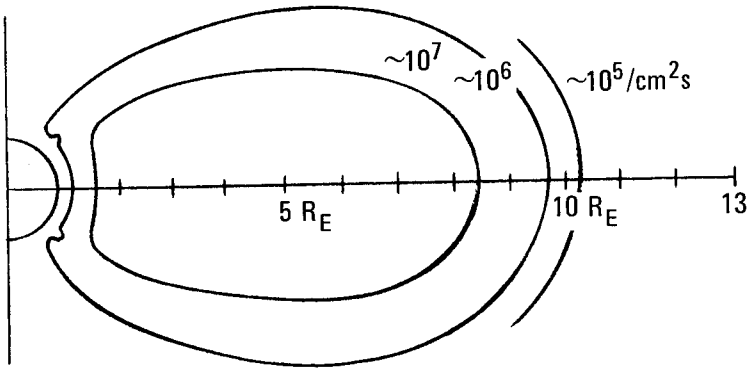

d. ELECTRON FLUX, E > 40 keV

Figure 10.—Proton and electron spatial distributions in the trapped radiation belts (ref. 8).

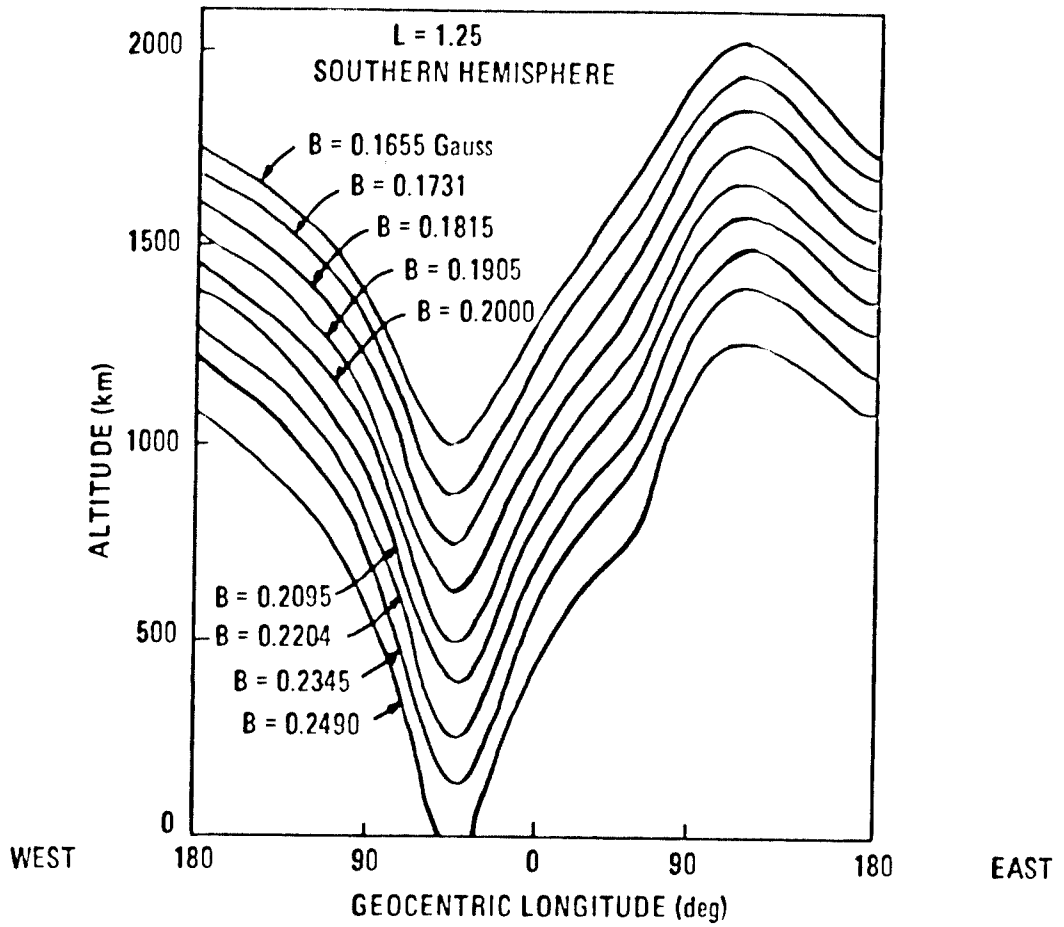

Figure 11.—Altitude variation of field strength in the South Atlantic anomaly.

2.2.2.2 Electrons

The characteristics of the natural electron population in the inner belt were masked for many years by the presence of electrons that had been introduced by nuclear detonation at high altitudes in the Starfish experiment.

(a) Artificial Radiation Belts

Table 1 gives basic information on the detonations that have caused the artificial radiation belts. The most important source of charged particles from the detonations is the β-decay of fission fragments which results in the emission of electrons.

- Argus

Of all the tests listed in table 1, only the Argus tests were specifically designed to study trapping of charged particles by the Earth's magnetic field. The tests were conducted near

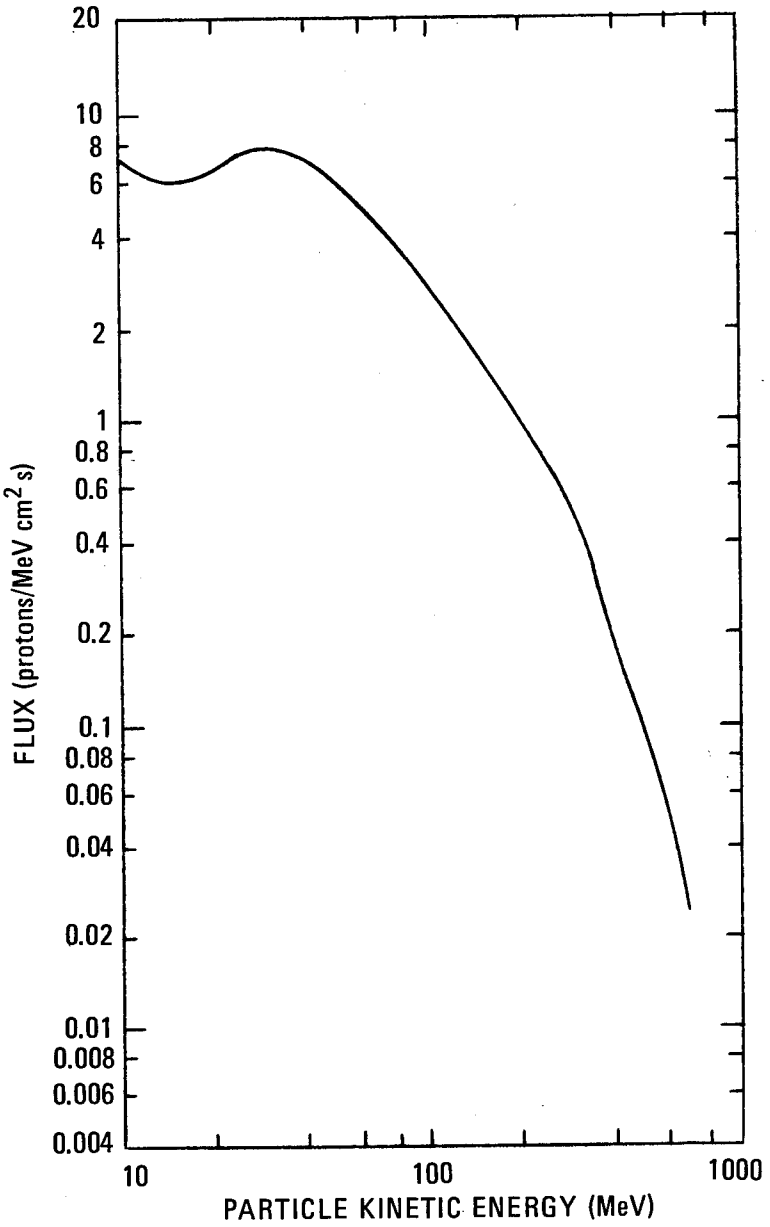

Figure 12.—Energy spectrum of high energy protons in the inner radiation belt (ref. 35).

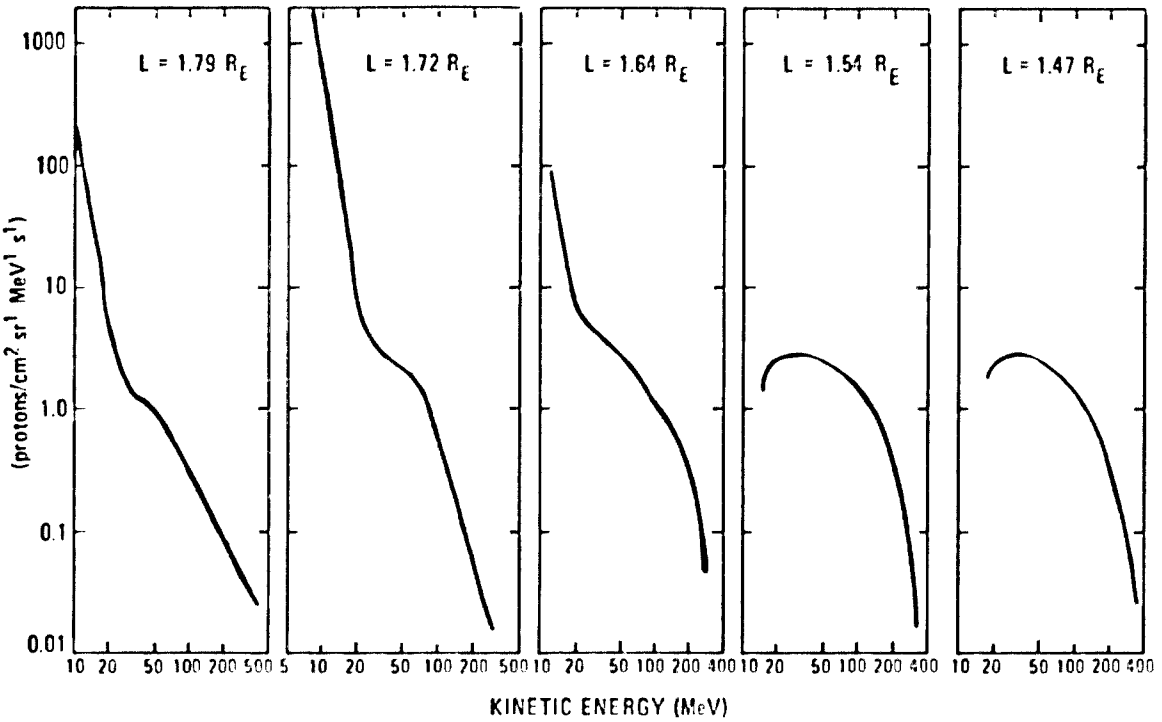

Figure 13.–Radial variation of high energy proton spectra in inner radiation belt (ref. 40).

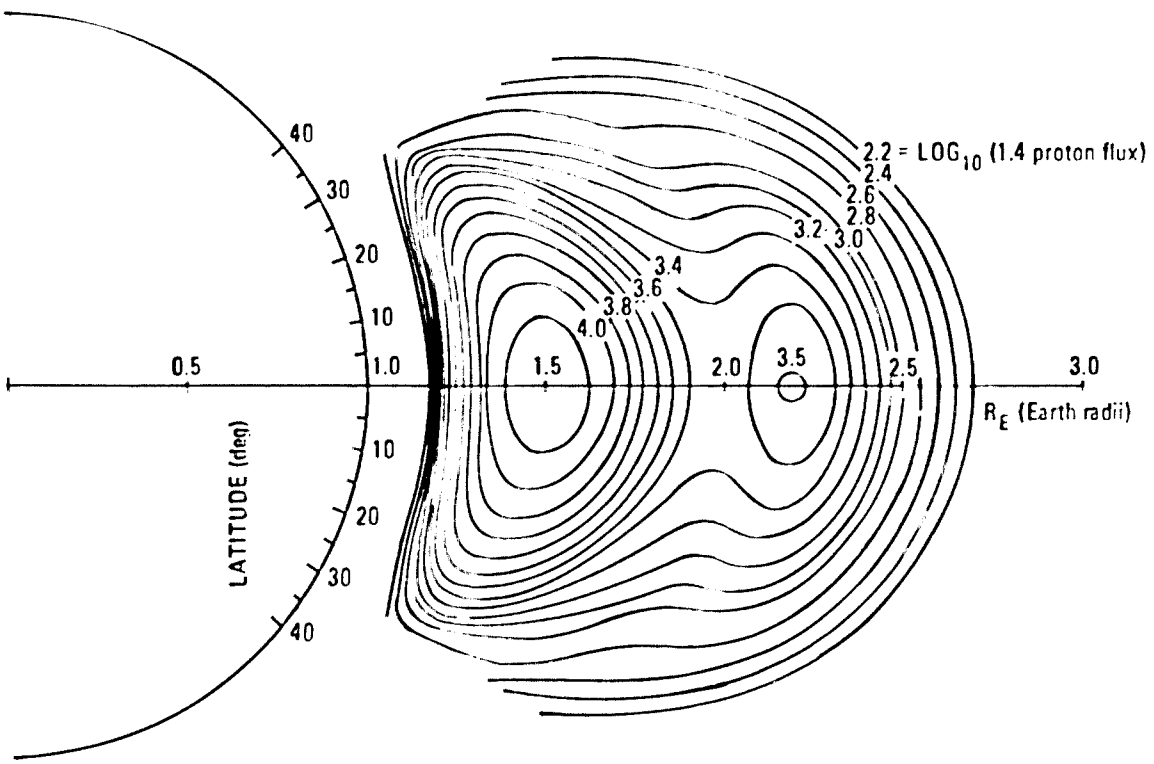

Figure 14.–Spatial distribution of high energy protons ($40 < E < 110$ MeV) (ref. 8).

the South Atlantic anomaly and demonstrated that electrons could be injected into the geomagnetic field and be trapped. The artificial radiation belt created by Argus was located at about L = 1.7 and remained stable for several weeks.

Table 1.
High Altitude Nuclear Detonations
(ref. 42).

Event	Altitude (km)	Date	Latitude	Longitude	Approximate L-Value of Detonation	Approximate Decay Time
Teak	76.8	1 Aug 1958	17°N	169°W	1.12	~few days
Orange	42.97	12 Aug 1958	17°N	169°W	1.12	~1 day
Argus 1	~200	27 Aug 1958	38°S	12°W	1.7	0-20 days
Argus 2	~250	30 Aug 1958	50°S	8°W	2.1	10-20 days
Argus 3	~500	6 Sept 1958	50°S	10°W	2.0	10-20 days
Starfish*	400	9 July 1962	16.7°N	190.5°E	1.12	~8 years
USSR 1	–	22 Oct 1962	–	–	~1.8	~30 days
USSR 2	–	28 Oct 1962	–	–	~1.8	~30 days
USSR 3	–	1 Nov 1962	–	–	1.75	~30 days

*Reference 43.

- Starfish

The Starfish test on July 9, 1962,* although not intended for the study of trapped particles, nonetheless created an artificial radiation belt of high intensity and long-term persistence. Four satellites, Injun 1, Ariel 1, TRAAC, and Cosmos V were in orbit at the time of the test and Telstar 1 was launched into orbit the following day. Initial spatial distribution in the area of the test is incomplete because none of the satellites was equipped to measure the intensity and spectrum encountered nor did they have orbits that permitted measurement of the belt's full extent.

Data obtained several hours after the test indicated the formation of an intense radiation belt centered at about L = 1.2 (ref. 42). Cosmos V showed that the electron flux at L = 2.2 increased by a factor of 100 in its first orbit after the test (ref. 44). Ariel 1 showed that the electron flux increased out to L = 7 (ref. 45).

Inner belt electron energy spectra obtained from the Starad (1962 βK) satellite are shown in figure 15 (ref. 46). These data, obtained several months after the Starfish test, indicate the radial variation of the electron population.

*NASA SP-8074 (Spacecraft Solar Cell Arrays) discusses radiation damage to spacecraft that was caused by Starfish and related design development in solar cells.

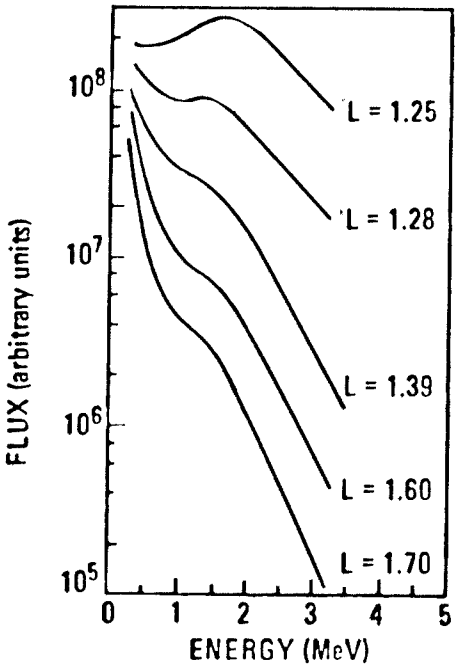

Figure 15.—Energy spectra of inner belt electrons after Starfish (ref. 46).

The spatial distribution of the Starfish electrons changed rapidly as the electrons expanded outward and drifted around the Earth and subsequently began to decay. The radial and latitude distribution of particles with energy > 0.4 MeV recorded by Telstar 1 two days after Starfish is shown in figure 16 (ref. 42). The subsequent decay of the electrons is shown in figure 17 (ref. 47) for $1.7 < L < 2.5$. After the initially-rapid decay of the electron population, the lifetime of the electrons is a function of L, energy E, and field strength B (for $L < 1.4$).*

The eastward drift of Starfish electrons from the initial Pacific Ocean location added to the large electron fluxes over the South Atalntic where the radiation belt is closest to Earth (fig. 14 and ref. 48).

(b) Natural Radiation Belts

Since the disappearance of Starfish electrons by the end of 1970 observed electron densities have been attributed to natural processes. The long term changes of electron flux between the epochs 1964 and 1966 are shown in figure 18 (ref. 18). For energies greater than 290 keV, the order of magnitude decrease below $L = 2$ is associated with the continual decay of Starfish electrons. The effects of the Starfish background disappear between

*See D. S. Beall, C. O. Bostrom, and D. J. Williams, "Structure and Decay of the Starfish Radiation Belt, October 1963 to December 1965", J. Geophys. Res., vol. 72, no. 13, July 1, 1967 and
E. G. Stassinopoulos, P. Verzariu, "General Formula for Decay Lifetimes of Starfish Electrons," J. Geophys. Res., vol. 76, no. 7, pp. 1841-1844

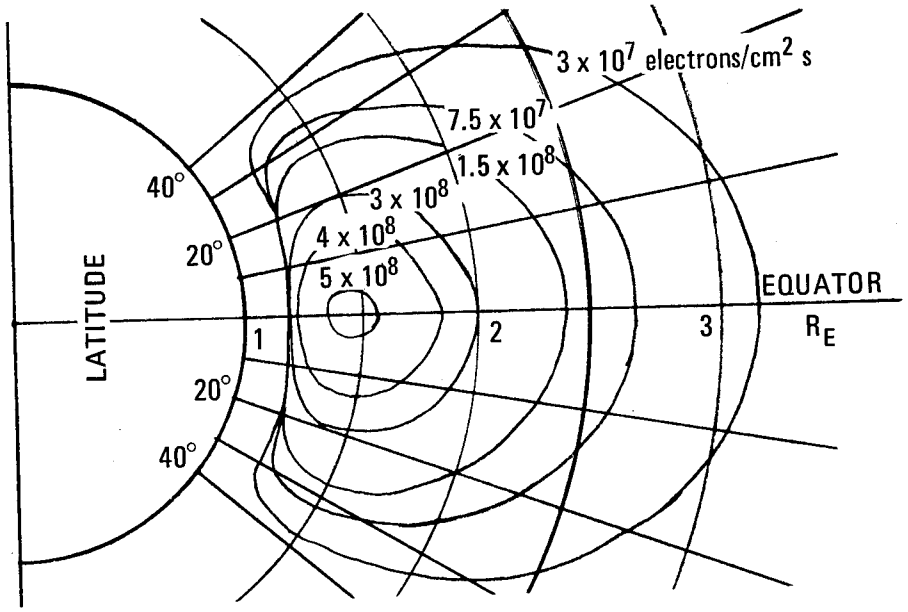

Figure 16.—Spatial distribution of electrons two days after Starfish (ref. 42).

L = 2.4 and 2.6, and a more or less constant intensity is found. The curve for 120 to 290 keV shows an intermediate behavior, whereas the very low energy band shows an essentially unchanged intensity between these epochs. After 1970, there is no indication of a natural source for electrons with energy $\geqslant$ 1.2 MeV (ref. 39).

The inner belt electron fluxes have temporal variations that are associated with the solar cycle and magnetic storms. The latter, although not great in number, cause significant changes in flux and distribution of the electrons. The electron flux associated with a strong storm of May 1967 is shown in figure 19. As the figure shows, readjustment of the flux after the initial injection may last beyond three months. In some cases, a quasi-stable level of elevated flux persists up to 60 days and then at a well defined point in time begins to decay exponentially to a final level. That level decays very slowly like the Starfish background (ref. 18).

Measurements made by satellite 1971 089A showed that naturally-trapped electrons at the lower edge ($L \leqslant 1.3$) of the inner radiation belt often show concentrations in narrow energy bands (ref. 49). These concentrations are attributed to the response of the inner belt's electron population to magnetic disturbances. Similar concentrations were also observed at the outer edge of the belt ($L \approx 1.4$ to 1.8). The energies of these peaks usually decrease very rapidly with increasing L value to the minimum values that are associated with the slot region (section 2.1.2.1).

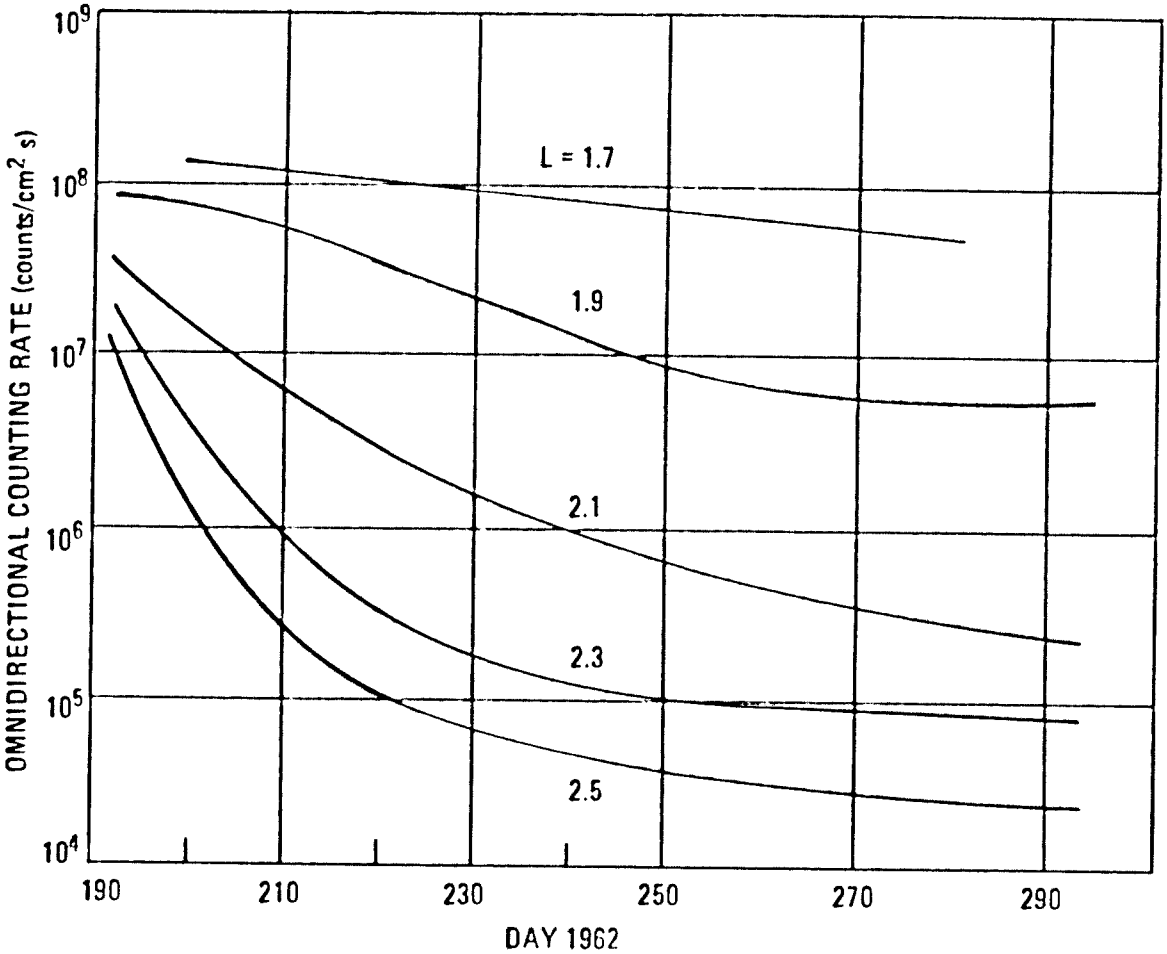

Figure 17.–Decay of inner belt electrons (E>0.4MeV) after Starfish (ref. 47).

2.2.3 Outer Radiation Belt

2.2.3.1 Protons

Measurements in the outer belt by OGO 3, Explorer 12 and 14, and Mariner 4 showed directional differential spectra of proton intensities for the energy range 200 eV $\lesssim$ E $\lesssim$ 1 MeV. The spectra for three values of L are shown in figure 20 (ref. 50). The average proton spectrum is characterized by a single maximum of intensities at 5 to 10 keV and monotonically decreasing intensities with lower and higher proton energy.

Spatial distribution of the protons is approximately that shown in figure 10. Also, the protons are strongly limited to the equatorial regions. The proton population is stable in time during geomagnetically quiet times (ref. 51) as shown by similarity of fluxes measured by Explorer 14 with those measured by Explorer 12 a year earlier. Variation in high energy proton ($40 < E < 110$ MeV) flux was observed for $L < 2.8$ during magnetic storms; however, after the storm, the flux for $L < 2.4$ returned to the pre-storm level (ref. 52).

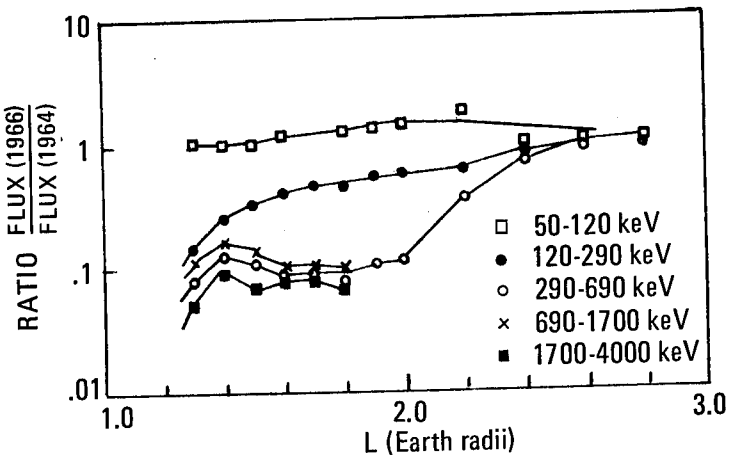

Figure 18.—Long term changes in electron flux between epochs 1964 and 1966 (ref. 18).

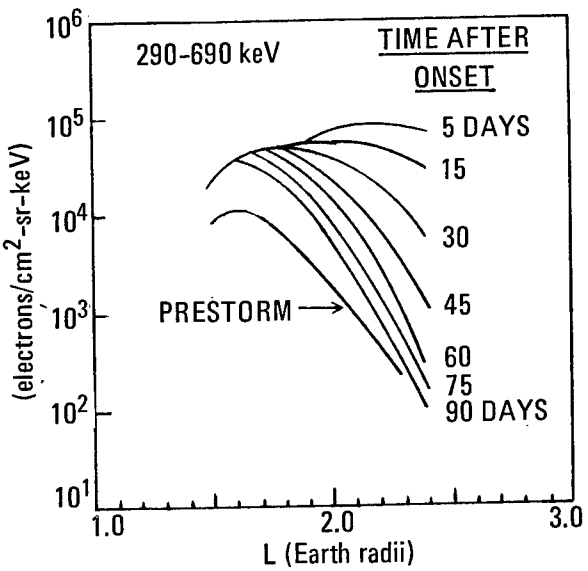

Figure 19.—Summary of effects of magnetic storm of May 1967 25, on electron flux (ref. 18).

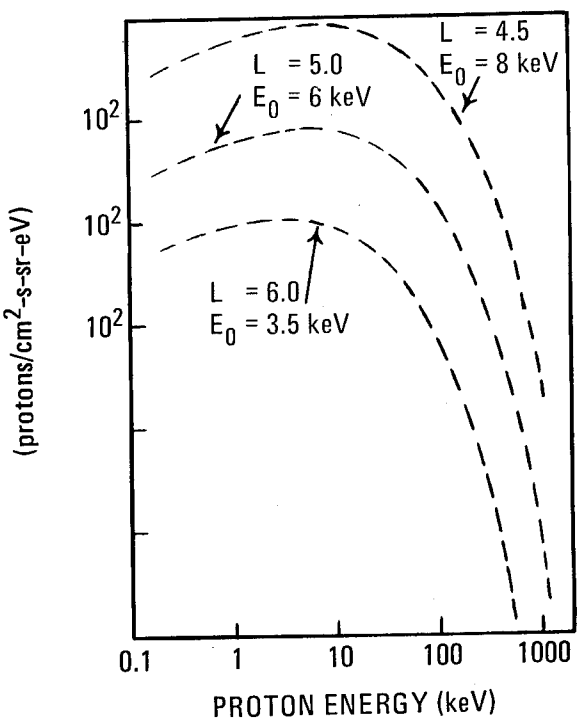

Figure 20.—Energy spectra of outer belt protons for different values of spectral parameter E_0 (ref. 50).

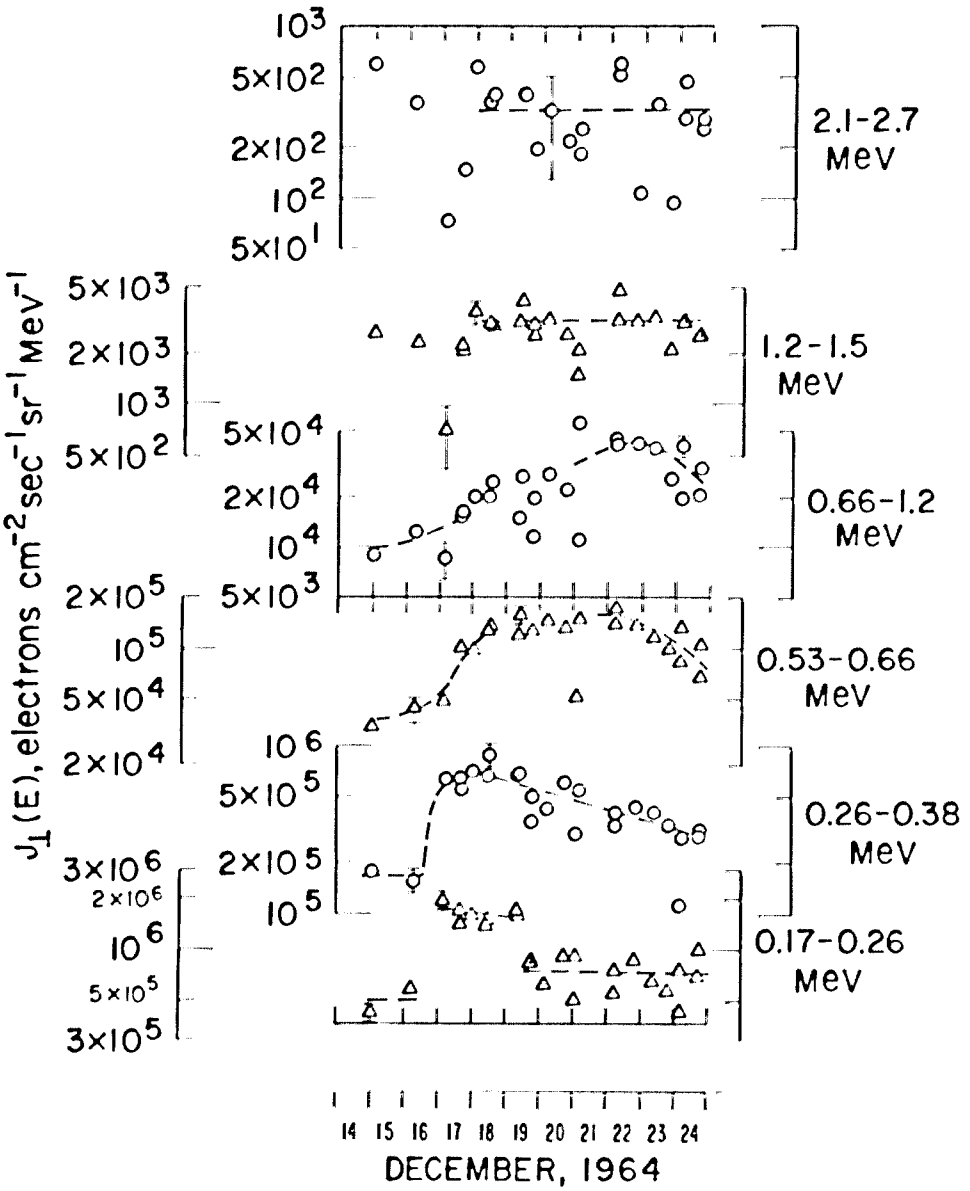

Figure 21.–Peak outer belt electron intensities at 50 to 60° geomagnetic latitude (ref. 55).

2.2.3.2 Electrons

Electrons in the outer radiation belt change grossly in intensity with time (ref. 53). For example, from October 1962 through February 1963, the following variations in electron intensity were observed by Explorer 14 (ref. 54): a factor of 100 for $E > 0.04$ MeV, a factor of 10 for $E > 0.23$ MeV, and a factor of 100 for $E > 1.6$ MeV. Figure 21 shows variations in electron intensity during 10 days in December 1964 (ref. 55).

Electron spectra for very low energy ranges, obeserved by OGO 3 in 1966, revealed significant features of the outer belt electrons as shown in figure 22 (ref. 20). The energy spectra are similar for each L value with the spectra shifting to lower energies with higher values of L. Electron fluxes of significant magnitude were recorded at the L values being considered with energy density at a maximum in the range of several hundred eV to 1 keV. A sharp increase of electron flux accompanies a geomagnetic disturbance (ref. 20).

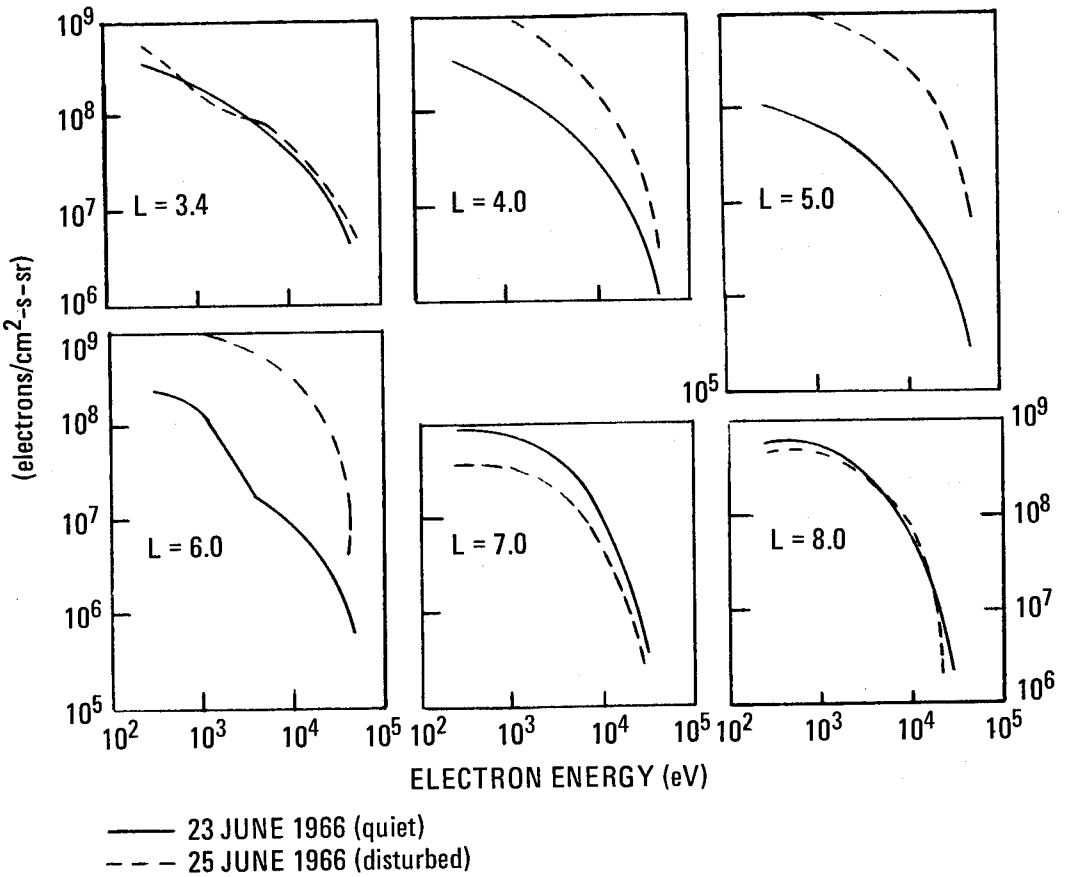

Figure 22.—Energy spectra of outer belt electrons (ref. 20).

Considerable temporal variation in electron intensity occurs in conjunction with several phenomena. Trapped electrons respond readily to magnetic disturbances; the degree of response depends on the energy band (refs. 54 and 56) and becomes more pronounced with increasing values of L, particularly for $L > 4$ (ref. 57). The flux can vary by a factor of 100 in response to the 27-day cycle that is related to Sun rotation (ref. 58). For $L > 5$, diurnal variations occur in which the trapped electron flux at local noon reaches a level that is several orders of magnitude greater than the flux at local midnight (ref. 59). Figure 23, based on Explorer 12 and 14 observations, summarizes the omnidirectional intensities of $E > 0.04$ MeV electrons.

2.2.4 Trapped Alpha Particles

Alpha particles, i.e., helium nuclei (He^{++}), are present in the interplanetary medium and are also found in the inner and outer belts. Although the flux of the trapped alpha particles is small compared to protons and electrons, they represent a measurable fraction of the trapped charged particle population.

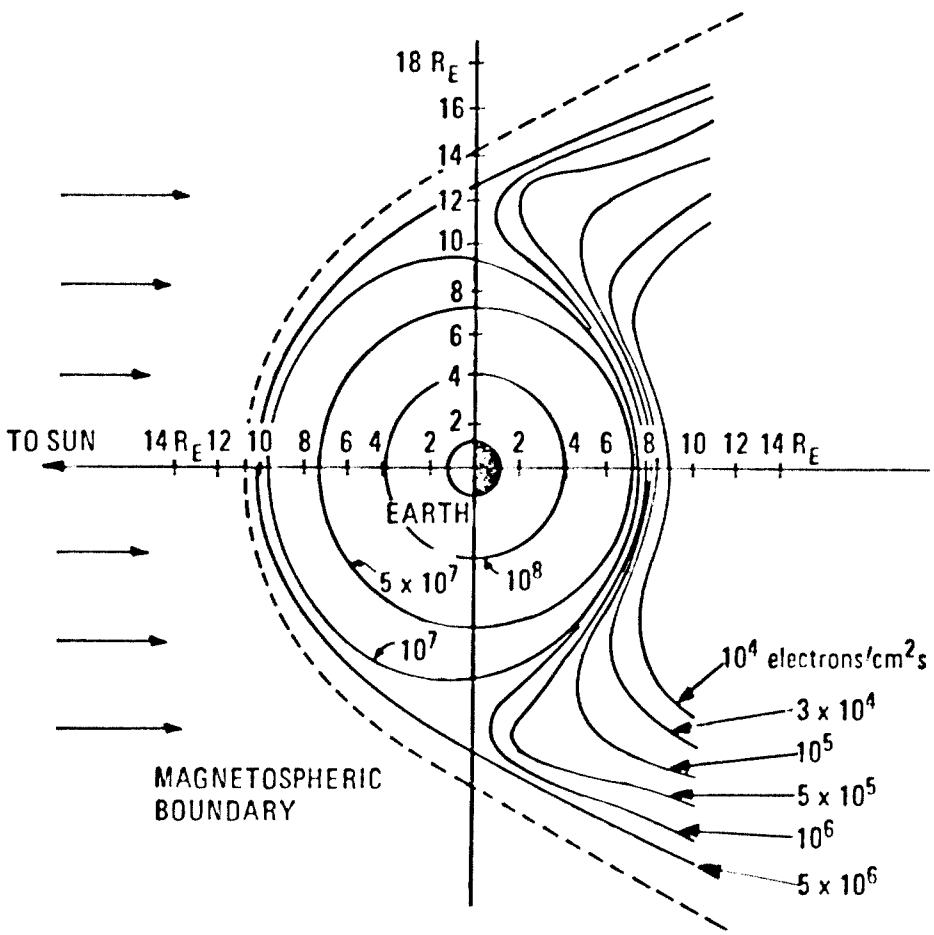

Figure 23.—Regions of rapid electron flux temporal variations by a factor of 10 or larger ($E \geq 40$ keV) (ref. 60).

The characteristic alpha-to-proton ratio (J_α/J_p) in terms of kinetic energy per nucleon was found to be approximately 2.2×10^{-4} for particle energies of 0.52 MeV/nucleon at $L \sim 3.1$ (ref. 61). For particle energies of 0.64 MeV/nucleon the maximum ratio occurs in the range $2.25 \leqslant L \leqslant 4.25$ as shown in figure 24. For the total energy of 2.56 MeV, the ratio is relatively constant for $L \geqslant 3$. For $L < 3$, the ratio decreases abruptly because the α-particle intensities decline rapidly without a corresponding decrease in protons (ref. 62). Results reported in reference 63 show that J_α/J_p increases sharply below 0.5 MeV/nucleon as the α-particle spectrum shifts to lower energies. The ratio is also highly susceptible to magnetic storms and has been noted to be as much as an order of magnitude greater than the 2.2×10^{-4} noted previously. Post-storm values gradually decay to a quiescent value in about 3 months. The ratio for $E \geqslant 0.5$ MeV/nucleon appears to be relatively constant and in the absence of geomagnetic storms, the $E \leqslant 0.5$ MeV/nucleon ratio may approach 2.2×10^{-4}.

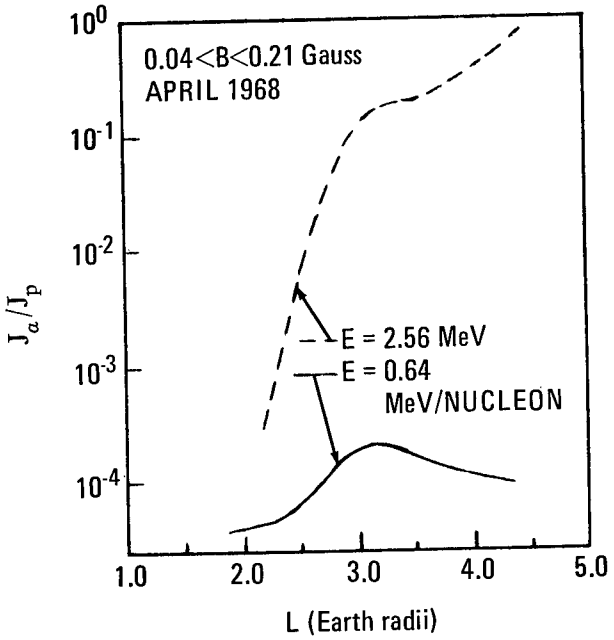

Figure 24.—Alpha-to-proton ratio (ref. 62).

2.3 Charged Particle Sources

It has been known for some time that the sources of the charged particles that enter the magnetosphere from interplanetary space are galactic cosmic radiation and solar radiation and also that charged particles are produced in the ionosphere (refs. 8 and 9). Investigations have shown that solar wind particles enter the magnetosphere through the polar cusps and that cosmic ray protons caused nuclear interactions that result in production of charged particles.

2.3.1 Galactic Cosmic Radiation

Galactic cosmic radiation consists of low intensity, extremely high-energy charged particles that originate outside the solar system (ref. 64). These particles (about 84% protons, 13% alpha particles, and the remainder heavier nuclei) bombard the solar system from all directions. Energies range from 10^2 to beyond 10^{13} MeV per particle. Galactic cosmic radiation intensity is reduced near the Earth where the paths of the particles are influenced by the Earth's magnetic field.

Charged particle production is not affected much by trapping of cosmic particles or by charged particles that are produced directly by impingement of cosmic rays on the atmosphere*, e.g., μ-mesons. The cosmic ray proton flux is too low to be significant source, and the proton energies are generally too high to be trapped permanently. Collisions of the protons with atmospheric particles are generally ineffective in producing a significant albedo (scattering) flux because the energies of the protons (often in the BeV range) are too high. The high energy collisions produce μ-mesons which decay to electrons with energies up to 50 MeV; but this source is insignificant compared to other charged particle sources.

2.3.2 Solar Radiation

Solar radiation consists of energetic particles emitted from active, disturbed regions on the Sun during solar flares and of a continuous flow of low-energy particles known as the solar wind. Reference 1 gives more detail on solar radiation.

2.3.2.1 Solar Flare Particles

The charged particles associated with solar flares consist primarily of protons; particles heavier than protons (predominantly alpha particles He^{++}) also appear to be present in each solar event. After a solar flare, particles may be detected in the Earth-Moon region within several minutes to several hours. The variation in travel times results from differing event locations on the Sun and changing configurations of the interplanetary magnetic field. The higher-energy particles reach the region of Earth first. The maximum number of particles typically arrive ten to twenty hours after the onset of the event. Particle flux may persist up to several days if the solar flare event is large.

Solar energetic particles gain access to the polar caps, the magnetotail, and the magnetosphere (ref. 25). Particle energy levels and travel time from the Sun for the different access regions are given in table 2. In the polar regions, solar protons and electrons enter at the polar cusps (refs. 14 and 23). Electrons gain access with high efficiency and show little variation of flux with latitude, whereas low-energy solar proton fluxes often have latitudinal variation (ref. 65). Solar flare electrons with $E \approx 50$ keV appear in the magnetotail with little delay after the solar flare and enter the tail at distances greater than 60 R_E (ref. 66). Protons of 1 to 10 MeV show some delay and enter within a few hundred R_E. Data obtained from ATS 1 satellite showed that solar protons with energies greater than about

*Section 2.3.3 discusses direct production of neutrons by cosmic ray collisions with the atmosphere.

Table 2.
Solar Particle Travel Times to Access Regions
(ref. 24)

Location	Particle	Energy Level	Travel Time (min)	Access Regions (R_E)
Magnetotail	Electrons	>40 keV	~10 (statistical)	5000
		~50 keV	1.7	900
	Protons	0.7-40 MeV	15-120	1000
		0.6-1.2 MeV	30-60	1400-2800
Polar Cap	Electrons	~50 keV	~1	600
	Protons	0.5-4.2 MeV	~30	1400
		1 MeV	7-40	420-2400
		~0.35 MeV	~60	2200
Magnetosphere	Protons	>12 MeV	15-110	
		85-95 MeV	5-10	
		1-15 MeV	30-240	
		20 MeV	10	

20 MeV had essentially free access to the magnetosphere down to synchronous altitude at all local times. During disturbed times, solar protons down to less than 1 MeV in energy can reach synchronous altitude without attenuation (ref. 53).

Solar protons produced during solar flares have energies up to several hundred MeV. Because of the nature of the Earth's magnetic field, these particles are excluded from the equatorial region and encounter the Earth in the polar regions. Satellite measurements over the polar caps indicate strong distinctions between north pole and south pole proton fluxes (ref. 25). Solar particle studies have indicated that both solar electrons and protons have access to closed field lines at latitudes that vary with geomagnetic conditions, and significant pseudotrapping of the solar fluxes has been measured (ref. 65). Cutoff levels of the geomagnetic field that govern entry of solar flare protons into polar cap regions are given in reference 67; protons are considered at seven energy levels between 1.2 and 39 MeV. Relative abundances of solar cosmic rays ranging from helium to iron nuclei were measured in reference 68. In addition, it appears that the helium abundance varies from flare to flare.

It has been suggested (ref. 69) that neutrons may also be produced during solar flares. The existence of solar neutrons has not been verified experimentally; however, it is suggested that low energy protons observed outside the magnetopause may result from the decay of solar neutrons (ref. 8).

2.3.2.2 Solar Wind Particles

The solar wind is composed of very low energy particles, consisting of electrons and ionized hydrogen (H^+) of about 1 keV. Alpha particles are also present with energies of about 4 keV. The ratio of alpha particles to ionized hydrogen particles is variable, apparently

increasing as solar wind velocity increases (ref. 70). Data obtained on Vela satellites (ref. 71) indicated the presence of electrons in the energy range of 150 to 500 eV. However, the average energy for electrons in the solar wind is considered to lie in the 10 to 20 eV range.

The solar wind is a constant source of energetic particles (ref. 1) that generally flow around the Earth (sec. 2.1.1). However, some solar wind particles gain access to the magnetosphere through the polar cusp regions and elsewhere (sec. 2.1.2.4). This entering flux is related to daytime auroras, ionospheric irregularities, and geomagnetic fluctuations (ref. 22).

2.3.3 Cosmic Ray Albedo Neutron Decay (Crand)

Galactic cosmic radiation has little direct effect on the charged particle population in the magnetosphere (sec. 2.3.1). However, the high energy cosmic ray protons produce neutrons as a result of collisions in the atmosphere. For example, a 5 BeV cosmic ray proton produces about 7 neutrons in the atmosphere. About 10% of these neutrons diffuse outward into space. As the neutrons scatter, they decay into protons and electrons. The process by which a scattering (albedo) flux of neutrons is produced by cosmic ray protons and subsequently decay is referred to as cosmic ray albedo neutron decay (CRAND) (refs. 72 and 73), as illustrated in figure 25. A later study provides additonal information on CRAND (ref. 74).

2.3.4 Solar Proton Albedo Neutron Decay (Spand)

Solar protons generated by solar flares and impinging on the atmosphere in the polar regions generate neutrons that scatter and subsequently decay in a process similar to CRAND (sec. 2.3.3 and refs. 72 and 75). The process is termed SPAND for solar proton albedo neutron decay.

Because solar protons are less energetic (several hundred MeV) than galactic cosmic ray protons, the resulting decay protons is of lower energy. SPAND is considered to be a contributor to proton fluxes with energies < 40 MeV for $L > 1.6$; however, additional sources are required to produce observed fluxes of the low energy protons (ref. 8).

2.3.5 Ionosphere

The densities of neutral hydrogen and thermal hydrogen ions at several Earth radii are about 10^5 greater than that of charged particles in the radiation belts. These particles form a

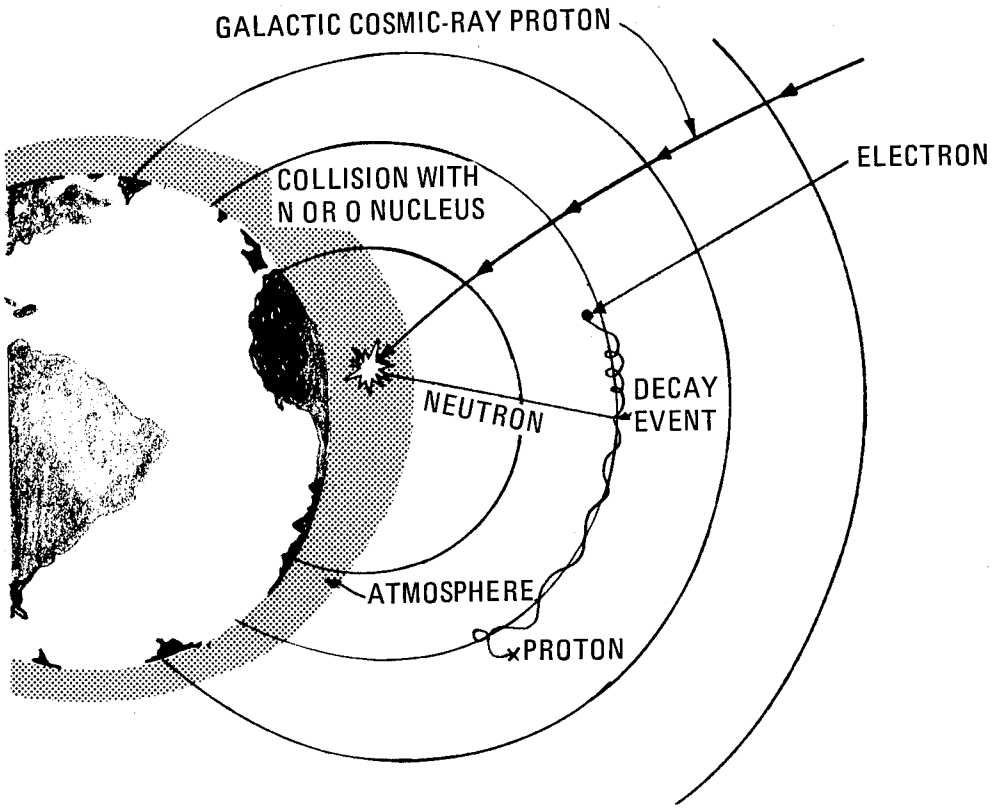

Figure 25.—Cosmic ray albedo neutron decay (CRAND) model (ref. 8).

potential source of charged particles. Magnetospheric convection (ref. 26) of particles from the lower part of the ionosphere (60 to 100 km) results in the movement of charged particles along magnetic field lines to higher regions of the magnetosphere. These charged particles, which are predominantly electrons and protons with thermal energies not exceeding several electron volts, form a region of dense plasma called the plasmasphere. The ionosphere is also considered to be a possible source of particles found in the plasma sheet (ref. 76).

2.4 Charged Particle Population Redistribution

The distribution of charged particles in the magnetosphere is the result of a balance between introduction of particles from various sources and the loss of particles either inward toward Earth or outward into space. The dynamics of the magnetosphere result in a constant redistribution of particles. Principal mechanisms include magnetospheric convection and radial diffusion. Of these, radial diffusion is of primary importance in the redistribution of trapped particles.

Three regions, the plasmasphere, the plasma sheet, and the ring current, are important in the redistribution of charged particles.

2.4.1 Radial Diffusion

Charged particles moving in a static magnetic field are constrained to remain along a particular magnetic field strength line (or shell), that is, the particle will not travel radially through the magnetic field. However, if the magnetic field fluctuates, the particles can be accelerated inward or outward radially through the field (refs. 77 and 78). The process is referred to as radial drift or radial diffusion.

Both periodic and random geomagnetic fluctuations have been observed. Regular fluctuations with periods of about one hour occur (refs. 79 and 80). If a resonant condition exists such that a particle drifts around the Earth with the period of the natural magnetic disturbance, particles at the proper phase will be accelerated and particles with other phases will be decelerated such as observed in a synchrotron (ref. 8). A more important contribution appears to be Bohm diffusion in which particles with circular motion are resonated at their gyro (or cyclotron) frequency, causing them to move a gyroradius in a gyroperiod (refs. 30 and 81). This type of diffusion appears to be important in explaining transport of particles in regions where magnetic field distortions are small such as in the plasmasphere and ring currents. Random fluctuations are more important than periodic ones in radial diffusion of charged particles. Sudden impulses and sudden changes in solar wind pressure are examples of random magnetic disturbances. During such a disturbance the geomagnetic field is rapidly compressed, especially on the sunlit side of the Earth. Particles drift with the magnetic field lines as the field is compressed; however, some particles will drift inward and others outward from their original field line. If the compressed field slowly relaxes back to its original configuration, the particles originally on a magnetic field line will be spread over a finite region in the magnetic field. If this pumping process is repeated many times, particles are diffused in the magnetic field (refs. 77 and 82). Experimental data indicates that sudden impulses acting on the magnetic field are the main driving mechanism for radial diffusion (ref. 83).

Radial diffusion can also be caused by fluctuations in the electric fields in the magnetosphere (refs. 84 and 85). It has been postulated (ref. 86) that diffusion produced by electric fields can result in diffusion coefficients as much as an order of magnitude greater than those derived for magnetic fluctuations (refs. 78 and 85). Acceleration of protons in the outer radiation belt by electrostatic diffusion has been proposed in reference 87. Measurements by OGO 5 identified electrostatic waves in the magnetotail between 5 and 10 R_i (ref. 88).

Inward radial diffusion of charged particles from the magnetosphere (caused by acceleration from random magnetic disturbances) is considered to be the primary mechanism for supplying protons, electrons, and alpha particles to the outer radiation belt (refs. 78 and 83). In particular, the low energy proton distributions can be explained on the basis of solar wind protons incident on the magnetosphere that diffuse inward (ref. 77). In addition, radial diffusion of protons from the outer radiation belt is considered as an important source of higher energy protons below $L = 2$ (ref. 89). Radial diffusion induced by periodic magnetic field fluctuations is felt to be the source of electrons in the lower radiation belt ($L = 1.15$) (ref. 90).

2.4.2 Plasmasphere

The convection of particles from the ionosphere results in formation of the plasmasphere and in the movement of plasma to the magnetosphere. The plasmasphere surrounds the Earth in a toroidal shape with a cross section resembling a dipole field (ref. 21). The boundary between the plasmasphere and the regions of plasma loss is characterized by a sharp density gradient. The boundary is called the plasmapause. The location of the plasmapause varies between $L \sim 3$ and $L = 6$ according to level of magnetic storm activity. During storms the plasmapause is compressed and during recovery phases it expands (ref. 30).

The importance of convection of particles from the plasmasphere to other regions of the magnetosphere is not fully known. In reference 28, it is demonstrated that this plasma flow can explain the precipitation of electrons from the outer radiation belt during morning hours.

Because the radiation belts lie within the plasmasphere, the plasma density can be very important in the loss of trapped particles from the belts. The plasmapause has been determined to be an especially active region for both whistler-mode wave propagation and emission (ref. 91) although these waves extend to most L values within the plasmasphere (ref. 49). The loss of particles due to whistler interaction is discussed in section 2.5.1.2.

2.4.3 Plasma Sheet

The plasma sheet is imbedded in the magnetotail as shown in figure 3. Charged particle populations in this region are discussed in section 2.1.2.7. The source of the plasma sheet particles has been attributed to three mechanisms: (1) convection upward from the plasmasphere (sec. 2.4.2); (2) convection of solar particles inward toward the Earth along the neutral sheet (sec. 2.3.2.1); and (3) solar wind particles introduced through the polar cusps (sec. 2.1.2.4).

The plasma sheet has been suggested as the source of low energy particles found elsewhere in the magnetosphere, particularly in the auroras and polar substorms. Proton intensities within the magnetotail are similar to the magnetosheath (fig. 3) intensities of protons that are directed normal to the magnetopause where it is downstream from the Earth in the solar wind (ref. 87). This suggests that these proton intensities have access to the magnetotail. Plasma sheet particles have been observed to move toward Earth along field lines reaching the auroral zones in the polar caps (ref. 27). Also, the electron islands in the magnetotail have been found to correlate with electron spikes over the polar caps seen with low orbit satellites. This suggests that auroral electrons are precipitated from the plasma sheet (ref. 92).

2.4.4 Ring Currents

Ring currents (i.e., electromagnetic currents circling the Earth, ref. 8) are generated during magnetic storms and are the result of the movement of electrons and protons in the

magnetosphere. Sources of the particles that form the ring currents are believed to be the interplanetary plasma or plasma sheet particles convected into the outer radiation belt (refs. 87 and 93) or low energy protons and electrons in the outer radiation belt disturbed by a magnetic storm (ref. 20).

Protons penetrate to lower L-shells than electrons and provide the dominant contribution to the ring current (ref. 81). Ring current protons have energies from 10 to 50 keV. The location of the ring current coincides with the location of the plasmapause (fig. 25), i.e., at about L = 3 to 6 (sec. 2.4.2). Two phases of the ring current have been noted: one is a symmetric current associated with outer edge protons that become stably trapped, and the other is an asymmetric current associated with unstable protons that drift toward the plasmapause (ref. 30). Ring current models are summarized in reference 94.

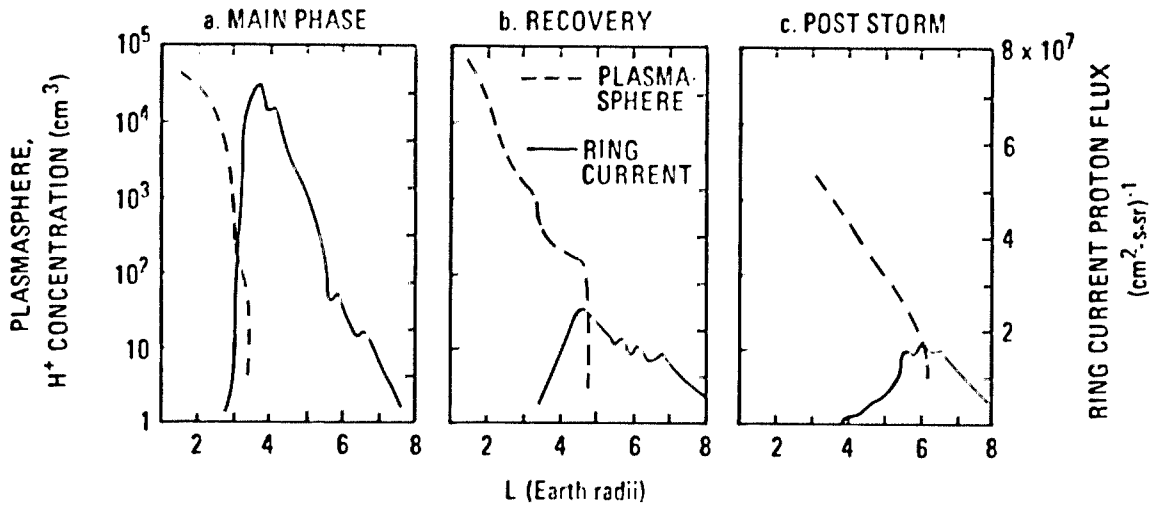

Figure 26.—Location of ring current and plasmapause—July 1966 magnetic storm (ref. 30).

The redistribution of the proton population because of ring current effects is significant. Proton precipitation mechanisms in the ring currents that are associated with proton auroras (ref. 95) may result from pitch angle diffusion caused by wave particle interactions (ref. 96) or from ion cyclotron turbulence interactions of the plasmapause (ref. 30).

2.5 Charged Particle Loss Processes

Numerous loss mechanisms have been proposed to explain observed particle distributions (refs. 8 and 9). However, as with sources, loss processes are often restricted to particular observed phenomena and in general are not well understood. The following paragraphs treat loss processes that are considered significant.

2.5.1 Particle Interactions

2.5.1.1 Coulomb Scattering

Collisions between energetic particles result in Coulomb scattering in which the particles may be slowed down or their direction of travel altered.

(a) Slow-Down

Charged particles lose energy by collisions with electrons and nuclei. At lower altitudes, the particles encounter a higher density of molecules and atoms in the atmosphere. Collisions with atmospheric particles result in rapid loss of energy and loss of the particles from the radiation belts.

In the inner belt, high energy protons between 5 and 100 MeV are lost primarily by collisions with oxygen atoms until the proton energies are reduced to about 100 keV. Electrons are not slowed down by collisions as effectively as protons because electrons scatter more easily.

(b) Scattering

Particle collisions cause scattering of the particles as well as slowing down. Coulomb scattering alters the angle of travel of the particle relative to the magnetic field lines (pitch angle). If its pitch angle changes enough, the particle can escape the radiation belt or avoid being trapped. The change in pitch angle can occur in a single collision but more likely occurs as a result of successive small energy-loss collisions.

Electrons are easily scattered because of their light mass. In the inner radiation belt below $L = 1.25$, electrons are lost primarily by scattering rather than by slowing down (ref. 97). Because lower-energy electrons are more easily scattered, they are lost more rapidly. Coulomb scattering of electrons in the atmosphere is described analytically by the Fokker-Planck equation (ref. 97).

(c) South Atlantic Anomaly

The loss of charged particles in the inner radiation belt by interactions with the atmosphere is characterized by a rapid decrease in particle lifetime as the higher density of lower altitudes is encountered (table 3). Minimum altitudes occur in the South Atlantic anomaly (sec. 2.2.2.1) where the magnetic field dips closer to Earth (fig. 14). Nearly all of the loss of protons for low L-shells occurs within the anomaly.

Electrons are also lost by Coulomb scattering in the South Atlantic anomaly (ref. 97). However, because of the effectiveness of the atmospheric scattering, the supply of electrons is replenished by scattering at slightly higher altitudes (ref. 16). In addition, the rapid scattering of electrons at low altitudes, particularly below 350 km, results in longitudinal

variation in the flux. The variation is caused by the "windshield wiper" effect in which electrons at high field strength (B) values (fig. 11) west of the anomaly are lost (wiped off) by scattering as they drift through the anomaly. However, east of the anomaly, the electron flux is replenished by scattering (ref. 97). The "windshield wiper" effect is illustrated in figure 27.

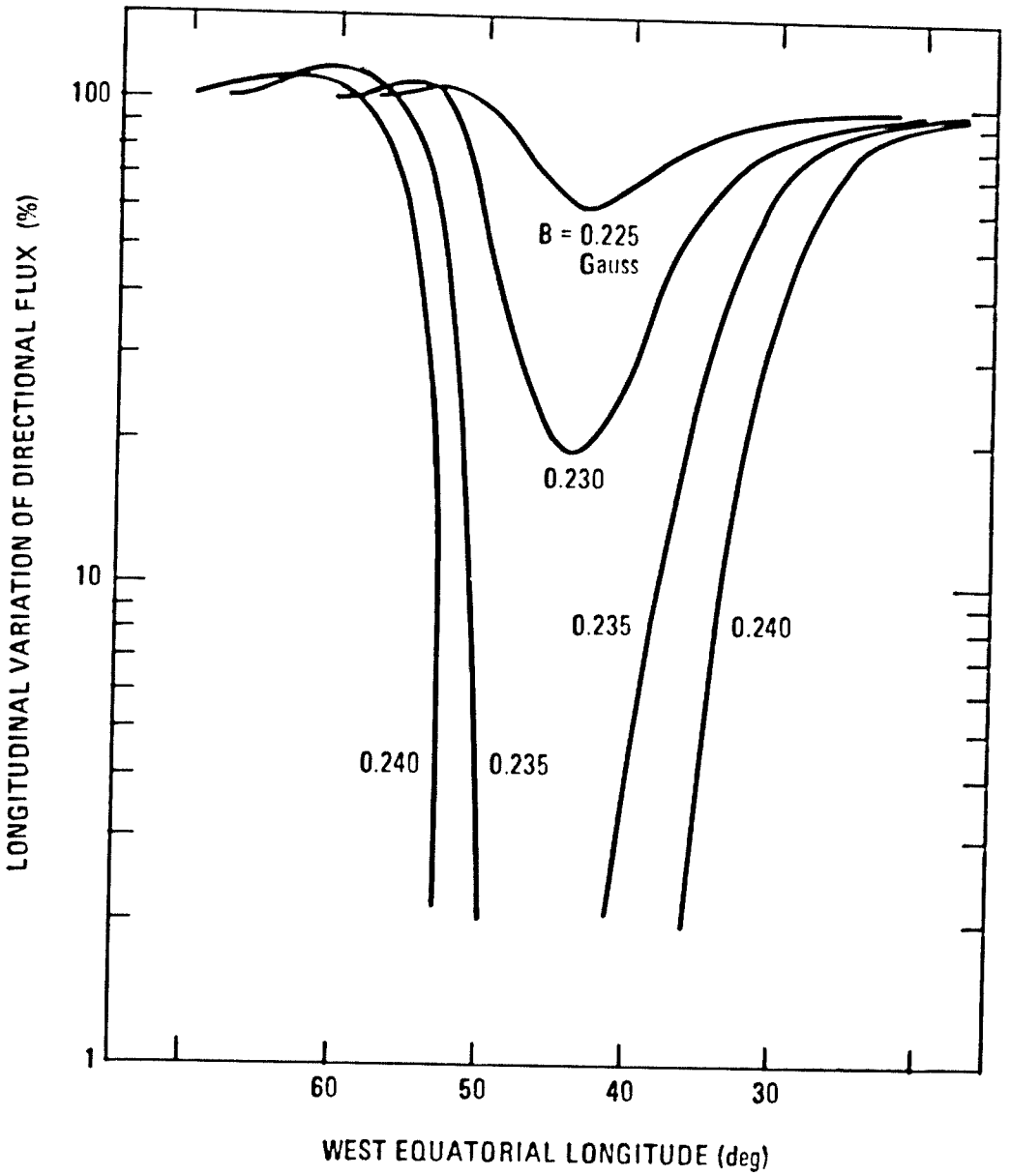

Figure 27.—Longitudinal variation of low-altitude electron fluxes (windshield wiper effect) at L = 1.25 (ref. 98).

Table 3.
Coulomb Loss Lifetimes of Trapped Particles with Pitch Angles Near 90°
(ref. 9)

Trapped Particles	L = 1.2 (days)	L = 1.6 (years)	L = 3 (years)
300 keV Electron	10	6	20
2 MeV Electron	100	60	200
10 MeV Proton	50	30	100
100 MeV Proton	1825	1000	(not trapped)

2.5.1.2 Pitch-Angle Scattering

Above L = 1.25, Coulomb scattering is no longer the predominant loss process for electrons although observation of the decay of electrons in artificially-created radiation belts indicates pitch-angle scattering is an important effect. Pitch-angle scattering can be caused by the interaction of electrons with electromagnetic waves in the magnetosphere. The most important electromagnetic waves observed in this type of scattering are those in the whistler mode (refs. 83 and 97). A whistler is a circularly-polarized wave that is generated by lightning. Scattering occurs when the wave propagates along a magnetic field line and interacts at a resonant frequency with an electron moving along the same line.

Whistler mode scattering has been proposed as the cause of electron precipitation from the outer radiation belt (refs. 28 and 29) and from the outer regions of the inner radiation belt (ref. 49). Whistler mode scattering best describes electron pitch angle diffusion away from the magnetic equator (ref. 97). It appears possible to account for the observed pitch angle diffusion of trapped electrons by a combination of whistler mode and bounce scattering. Bounce scattering is a resonant condition that is induced by perturbation forces with components parallel to the Earth's magnetic field lines.

2.5.2 Nuclear Interactions

The dominant loss process for protons with high energies (300 to 500 MeV) in the inner radiation belt, is nuclear interaction. An inelastic nuclear collision reduces the energy of a proton by a large enough factor that the particle can be considered lost. Below 300 MeV, nuclear interactions become insignificant.

2.5.3 Charge Exchange

Protons with energies less than 100 keV in the inner radiation belt are lost principally by charge exchange. In this process, the reaction of high velocity protons with ambient

hydrogen and oxygen atoms generates high velocity neutral atoms by addition of electrons to the fast protons. The fast neutrals are generally lost from the radiation belt before reionization can occur. Loss from charge exchange is negligible for energies above 1 MeV. It is felt that charge exchange is also important in the loss of protons with energy < 50 keV during the recovery period of a magnetic storm (ref. 30).

2.5.4 Magnetic Field Effects

One of the magnetic field effects that has been considered to explain the loss of protons in the outer radiation belt is scattering induced by magnetic waves (ref. 99). Two interactions have been noted. The first is the interaction of hydromagnetic waves in the trapped radiation belts with charged particles and consequent Fermi acceleration of the particles (ref. 100).

The second and more important is interaction of electromagnetic waves that are propagated along magnetic field lines with charged particles that are moving along the same field lines. If conditions are such that the particle cyclotron (gyro) frequency and the wave frequency are equal, that is, in resonance, the particle is accelerated (ref. 99). (The effect is similar to whistler scattering which is described in section 2.5.1.2.) This form of magnetic scattering is valid only for high energy protons and becomes more effective at high altitudes. It may also be the explanation for the absence of high energy protons in the outer radiation belt. An example is the resonant interaction between ring current protons and ion cyclotron waves inside the plasmapause that was hypothesized in reference 30. Subsequently, this interaction has been identified as the cause of diffusion of protons with $E < 50$ keV from the ring currents.

The Earth's magnetic field cannot trap protons and heavy particles if their energy is too great: the level beyond which trapping does not occur is the critical energy value. Accordingly, protons and heavy particles with energy above the critical values will not be trapped initially or will be lost if they are accelerated to an energy above the critical value.

2.5.5 Particle Precipitation

Charged particles in the radiation belts, the plasma sheet, and the ring currents are lost by precipitation (ref. 101). Considerable more evidence of precipitation of electrons than protons has been gathered because the proton flux is about 43 times smaller than that of electrons for the same particle density and energy. The precipitation of particles into ionospheric regions results in auroras. Proton auroras (ref. 102), however, are usually not visible and are much more diffuse than electron auroras.

Particle precipitation is particularly prevalent at latitudes between 60 and 80° where auroras occur. As demonstrated in figure 28, outer belt fluxes plunge into the atmosphere at latitudes between 50 and 70°. In the southern hemisphere, the outer belt fluxes blend with the flux contours affected by the South Atlantic anomaly between 30 and 50° (ref. 16).

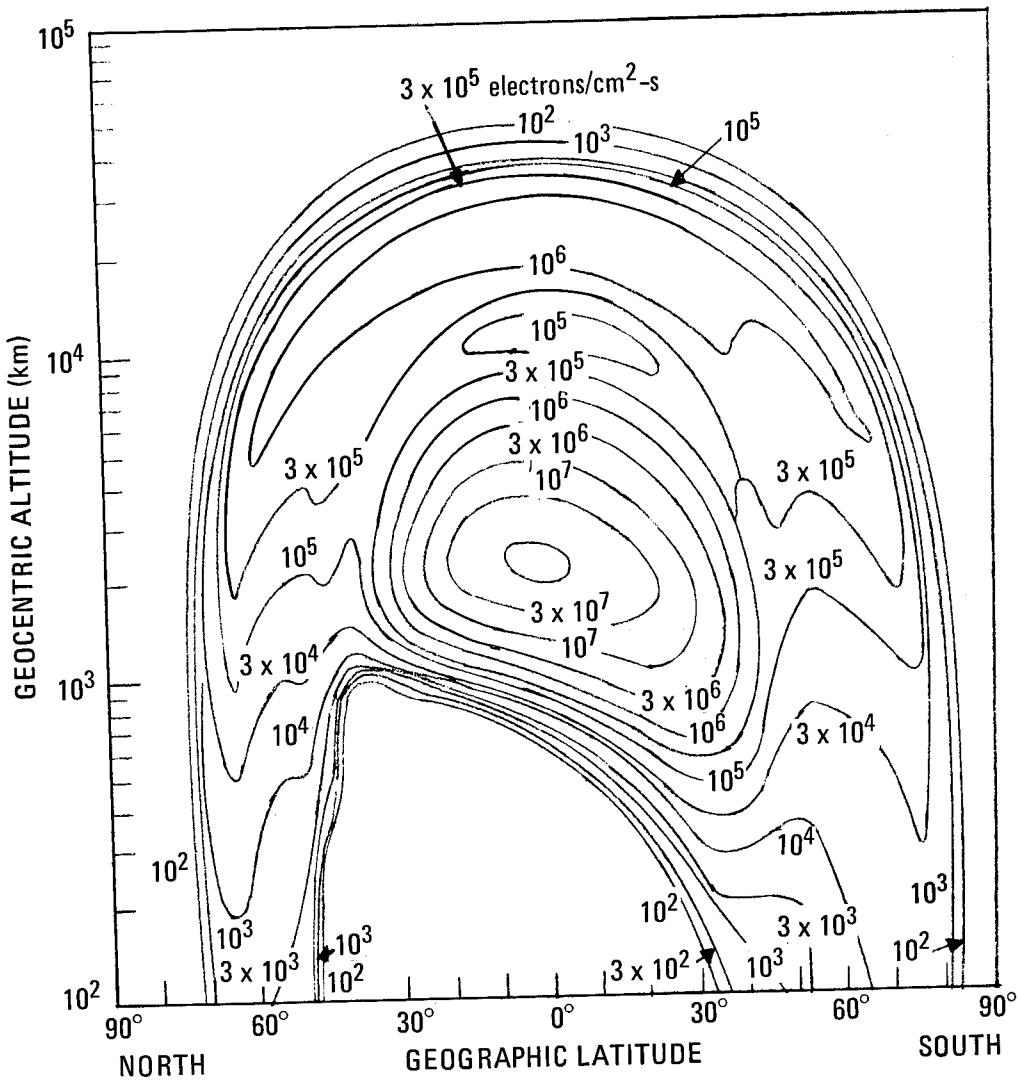

Figure 28.—Altitude variation of electron flux (E≥0.5 MeV) with latitude in August 1964, longitudinally averaged (ref. 103).

Lower energy particles are more susceptible to precipitation than higher energy ones. In particular, electrons with energies greater than 1 MeV can remain trapped and unaffected on field lines while fresh electrons with energies greater than 40 keV are being precipitated (ref. 104).

Electrons with characteristic energies of tens of keV are observed to precipitate at latitudes between 60 and 70° near local midnight. At higher latitudes (between 70 and 80°) near local midnight, precipitating electrons have energies of approximately 0.5 keV. Proton precipitation regions spatially overlap the zone of electron precipitation. For example, the peak of precipitation of $E > 4$ keV protons near local midnight is found between latitudes of 65 to 75° (ref. 101).

Loss mechanisms that cause particle precipitation include magnetic storm effects on plasma sheet electrons (ref. 29), whistler mode scattering of electrons in the outer belt and the outer region of the inner belt, atmospheric scattering of low altitude electrons and protons, and interaction of ion cyclotron waves and ring current protons. These effects have been noted in this section (2.5) and are reviewed in reference 101.

2.6 Effects Of Radiation On Spacecraft Systems

The effects of charged particles on spacecraft materials, components and crew have been demonstrated by numerous inflight experiments as well by degraded performance of spacecraft systems (ref. 105). In calculating the effects of charged particles on spacecraft, it is essential to determine the energy spectra and the time-integrated particle flux of the particles (sec. 2.7). These charged particle properties must then be related to the particular mission by consideration of such factors as the orbital apogee and perigee, inclination, and time in space. After the environment to be encountered by the spacecraft has been determined, the effects of the charged particles are assessed for spacecraft characteristics, i.e., materials used in the spacecraft structure, operating systems, and experiments; types of components; shielding effect of the spacecraft structure and shielding incorporated in the design for radiation protection; and the location of susceptible components.

Earth-orbiting spacecraft may spend considerable time in the trapped particle regions. External components and experiments are directly susceptible to charged particles. Internally, the spacecraft may be subject to secondary radiation phenomena such as bremsstrahlung radiation (X-rays and gamma rays which are emitted when energetic charged particles interact with spacecraft materials and are decelerated).

The structure often acts as the primary radiation shield for more sensitive components of the spacecraft system and for man (ref. 106). The optimum procedure is to use materials that will provide both the desired structural properties and the required radiation shield (ref. 2). Experience with manned spacecraft has shown that the spacecraft provides adequate shielding for the crew, but additional shielding may be required for critical components. For example, on Skylab the crew operating environment was within radiation criteria, but additional shielding was required for photographic film (ref. 107). Other susceptible items on spacecraft include photographic film, semiconductor devices, thermal control coatings, solar reflector surfaces, optical materials and devices, adhesives, and sealants. In general, photographic film is the most sensitive and adhesives and sealants least susceptible to damage. Semiconductors, which include solar cells, diodes, bipolar transistors, field effect transistors and metal oxide semiconductor transistors are particularly susceptible to charged particle damage. Of these, solar cells and biploar transistors are the most sensitive to charged particle interaction (ref. 108).

Thermal control coatings, solar reflector surfaces, and optical material devices can withstand radiation effects better than semiconductors; but their external location with minimal shielding may result in a higher exposure to the radiation environment than well-shielded components. Thermal control coatings, solar reflector surfaces, and optical materials for

lenses, solar cell cover slides, and optical coatings may suffer degradation of optical properties, particularly changes in thermal conductivity, and optical emissivity, absorptance and reflectance. In lenses, the optical transmission and the color of the lens may be affected. In addition, coatings for thermal control, solar reflection and optical purposes are susceptible to blistering from charged particle radiation. More detail on the effects of charged particles on materials are provided by references 2 and 109 through 111.

2.7 Charged Particle Environment Models

Accurate, reliable analytical models of the Earth's charged particle environment are difficult to formulate because of the large number of variables involved. The present state of the art of analytical models (as discussed in secs. 2.3 and 2.5) is inadequate for providing reliable information for use in spacecraft design. However, beginning with Explorer 12, extensive measurements of the trapped radiation belts have been made by numerous spacecraft.

These data have been processed and presented in useful engineering form in a series of NASA documents (refs. 6, 7, 103, and 112 through 118). The trapped radiation charged particle environment was divided into various segments of space, energy, and time that allowed considerable simplification of data representation. The various spacecraft data for electron and proton populations were analyzed to obtain flux distribution and energy spectra.

The measured data are usually in the form of particle fluxes measured within a specified energy range. The plot of the integral flux as a function of particle energy then constitutes the energy spectra for the measured particles. The omnidirectional integral flux, $J(>E,B,L)$ is defined as the total flux of particles (electrons or protons) integrated over all directions at some position in space specified by the appropriate values of B and L. The omnidirectional differential flux j is, therefore, defined as

$$j(E,B,L) = -\frac{dJ}{dE}$$

so that $j \Delta E$ gives the total flux of particles in the energy interval between E and $E + \Delta E$.

It is convenient for the analysis of the data to write J as a product of two functions, one of which is taken as essentially independent of E, that is, a function of magnetic space only. Thus,

$$J(>E,B,L) = F(B,L)\, N(E,B,L)$$

The function F can be taken to be the integral flux for some specific energy, E_1. Then $F(B,L)$ gives the variation of $J(>E_1)$ with B,L, and information on the particle spectrum (that is, the dependence of $J(>E)$ on energy) is given primarily by N.

In practice, the spectrum can often be satisfactorily approximated by an exponential. Then

$$J(>E,B,L) = F(B,L) \exp\left\{\frac{E_1 - E}{E_0(B,L)}\right\}$$

where $E_0(B,L)$ describes the change in spectrum with B and L. Alternatively, the spectrum may be taken to follow a power law. Then

$$J(>E,B,L) = F(B,L)\left(\frac{E}{E_1}\right)^{-P(B,L)}$$

Table 4 summarizes the models that have been developed on the basis of spacecraft measurements. The models present time-averaged or median values of particle flux except for Model AE3 and Model AE4 which also include statistical models. Time-averaged models were developed in areas where the flux is relatively stable (sec. 2.2) and median values were used where insufficient data was available for producing reasonable time-averaged models.

As more recent data became available, several of the models have been replaced by updated models. Thus Model AE2 (August 1964) replaced Model AE1 (June 1964); Model AE4 (February 1968) and Model AE5 (December 1967) subsequently replaced Models AE2 and AE3; Model AP6 (February 1965) replaced Models AP2 and AP4 (June 1964); and Model AP7 (July 1966) replaced Model AP3 (June 1964). (Because Model AP1 was not effectively changed by later data, it was not modified.) A model for high energy protons in the outer zone has not been developed because of the low densities encountered (sec. 2.2.3.1). A new proton model covering all energy ranges is being developed by the NASA National Space Science Data Center.

Models AE4 and AE5 define the electron environment, and Models AP1, AP5, AP6 and AP7 provide models of the proton environment.

Table 4.
Trapped Radiation Belt Models

Model Designation	Type of Particle	Energy Range MeV	L Range	Source (Ref.)	Date Published
AE1	Electron	>0.5	1.2 to 3.0	112	1966
AE2	Electron	>0.04	1.2 to 6.0	105	1966
AE3	Electron	>0.04	6.6	113	1967
AE4*	Electron	>0.04	3.0 to 11.0	6,114,119	1972, 1974
AE5*	Electron	>0.04	1.2 to 3.0	7,115,119	1972, 1974
AP1*	Proton	30 to 50	1.2 to 2.8	112	1966
AP2	Proton	15 to 30	1.2 to 3.0	112	1966
AP3	Proton	>50	1.2 to 2.8	112	1966
AP4	Proton	4 to 15	1.2 to 3.9	112	1966
AP5*	Proton	<4	1.2 to 6.6	116	1967
AP6*	Proton	4 to 30	1.2 to 4.0	117	1969
AP7*	Proton	>50	1.15 to 3.0	118	1970

*Recommended for current use in section 3.

3. CRITERIA

Models of the Earth's trapped radiation belts presented herein should be used in studies and design of space vehicles, their equipment, and experiments. Computer programs needed to compute useful quantities from the recommended models are discussed in reference 115 and are available from the National Space Science Data Center, NASA Goddard Space Flight Center. For other regions of the magnetosphere in which particles are not trapped, the design criteria monograph* being issued on interplanetary charged particles provides conservative design parameters. For the solar proton component of the flux in these regions, reference 1 recommends amounts by which the interplanetary solar proton flux should be reduced for different circular orbits to account for magnetospheric shielding. Reference 120 gives the relative importance of solar and trapped proton flux for circular orbits.

3.1 Electron Environment Models

Models AE4 (ref. 6) and AE5 (ref. 7) should be used for the electrons in the trapped radiation belts. These models were developed concurrently and were made to be compatible at the interface of L = 2.6. The electron models given herein represent conditions during periods of maximum solar activity and thus constitute conservative estimates for other periods.

*NASA SP-8118, March 1975.

For periods of minimum solar activity, Model AE5 (projected for 1975) in reference 119 may be consulted for the inner belt. To provide an outer belt model for minimum solar activity, the AE4 model for outer belt electrons (ref. 6) has been adjusted in reference 119 to make it compatible with the description of inner belt electrons given by Model AE5 (projected for 1975).

3.1.1 Inner Belt, 4.0 MeV > E > 0.04 MeV (Model AE5)

Model AE5 should be applied for electrons with energies in the range of 40 keV to 4.0 MeV between L = 1.2 and 3.0 R_i. The model is presented for an epoch of October 1967 (corresponding approximately to solar maximum). Temporal variations such as magnetic storm effects, solar cycle effects, and decay of residual Starfish electrons may result in significant flux changes. However, with the exception of magnetic storm effects, these variations cause the flux to decrease from that given by model AE5 and, thus, the model provides a conservative estimate of the electrons in this energy range.

The total electron flux in the inner zone at any given time is composed of four components: (1) a quiet day, i.e., no magnetic storm effects, at solar minimum, (2) a quiet day component that is dependent on solar cycle, (3) magnetic storm flux, and (4) residual flux from the 1962 Starfish nuclear explosion. For most L values at energies below 700 keV, the inner zone flux for a quiet day (based on the first two components) can be described analytically as follows.

The unidirectional flux for various values of L and time T (referred to October 1967 and an equatorial pitch angle of 90°) is

$$j = a_r f_1 (L,T) E \exp [-E/X_r f_2 (L,T)]$$

where the pitch angle(a)dependences of the parameters are given by the expressions

$$a(a_0,L,T) = a_r f_1 = a_r \left[\frac{\sin^m(a_0-a_c)}{\sin^m(\phi-a_c)}\right] \text{ for } \phi > a_0 \geq a_c$$

$$= a_r \qquad \text{for } 90° \geq a_0 \geq \phi,$$

$$X(a_0,L,T) = X_r f_2 = X_r [\sin^n a_0/\sin^n \phi] \text{ for } \phi > a_0 \geq a_c$$

$$= X_r \qquad \text{for } 90° \geq a_0 \geq \phi;$$

m and n are L-dependent pitch angle parameters and ϕ is an L-dependent limit for the pitch angle variation. The five model parameters are given in table 5 for 0.05 intervals in L for $L \leq 2$ and at 0.1 intervals at higher L values.

Table 5
Quiet Day Parameters (Model AE5) (ref. 7)
With Reference Pitch Angle of 90° for
Epoch October 1967

L (R_E)	a_r (cm^{-2} s^{-1} sr^{-1} KeV^{-2})	X_r (KeV)	m*	n*	ϕ (deg)	Magnetic Field Strength at Cutoff (Gauss)
1.30	1.71E03	83.7	2.80	0.670	67.1	0.232
1.35	2.39E03	84.3	2.20	0.660	61.4	0.234
1.40	3.08E03	85.1	1.70	0.650	57.5	0.238
1.45	3.81E03	85.7	1.20	0.640	59.0	0.241
1.50	4.56E03	86.5	0.93	0.630	65.0	0.245
1.55	5.21E03	87.5	0.92	0.620	66.0	0.249
1.60	5.74E03	88.4	0.91	0.610	67.0	0.253
1.65	6.08E03	88.8	0.90	0.600	66.5	0.257
1.70	6.42E03	89.1	0.89	0.590	66.0	0.262
1.75	6.81E03	89.5	0.88	0.580	68.0	0.265
1.80	7.16E03	89.8	0.87	0.570	70.0	0.268
1.85	7.57E03	89.0	0.86	0.545	76.0	0.271
1.90	7.93E03	87.8	0.85	0.520	86.0	0.274
1.95	7.80E03	86.5	0.83	0.500	90.0	0.277
2.00	7.50E03	84.7	0.80	0.480	90.0	0.280
2.10	7.15E03	81.0	0.79	0.470	90.0	0.286
2.20	7.00E03	77.0	0.78	0.460	90.0	0.292
2.30	6.50E03	74.5	0.77	0.450	90.0	0.298
2.40	6.00E03	72.0	0.76	0.440	90.0	0.304

*L-dependent pitch angle parameters, non-dimensional

The electron flux for energy levels above 700 keV depends on the effects of magnetic storms. Unfortunately, magnetic storms are not readily modeled and the frequency of effective magnetic storms in the inner zone is too low for a statistical approach. Therefore, for model AE5, a crude averaging process was used on the basis of measured data (ref. 7). The average flux from June 1966 to December 1967 was divided by a quiet day flux for an epoch of October 1967 to provide the ratio R_s in figure 29.

Figure 29 shows that the peak storm effect is observed in the energy range $100 > E > 850$ keV for $2.8 \geqslant L \geqslant 1.8$. These results verify that the analytical model for $E < 700$ keV provides a good estimate of the environment for $L \leqslant 1.9$ and that the quiet day model of electrons with $E > 700$ keV provides good flux estimates for $L \leqslant 1.8$.

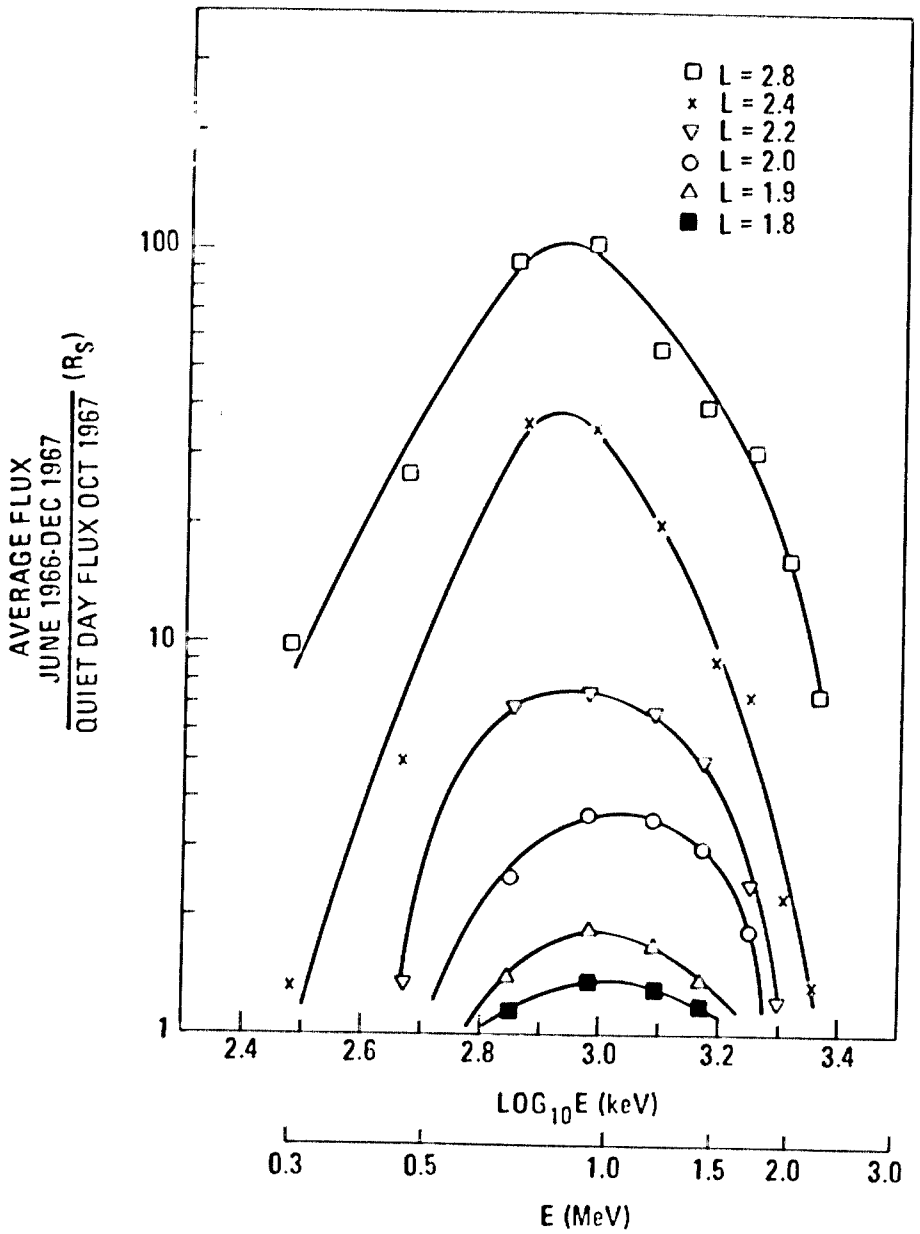

Figure 29.—Magnetic storm flux ratio R_s (ref. 7).

Figure 30 shows the omnidirectional flux map for the AE5 model environment that has been derived by numerical integration from the analytical and time-averaged unidirectional flux models (ref. 119). Threshold energies of 40 keV, 500 keV, and 1 MeV typify the radial profiles in the inner zone. An alternate form of the flux map in R_i and λ coordinates is shown in figure 31 where R_i is geocentric distance and λ is magnetic latitude. Nomographs of the model are available in references 7 and 115.

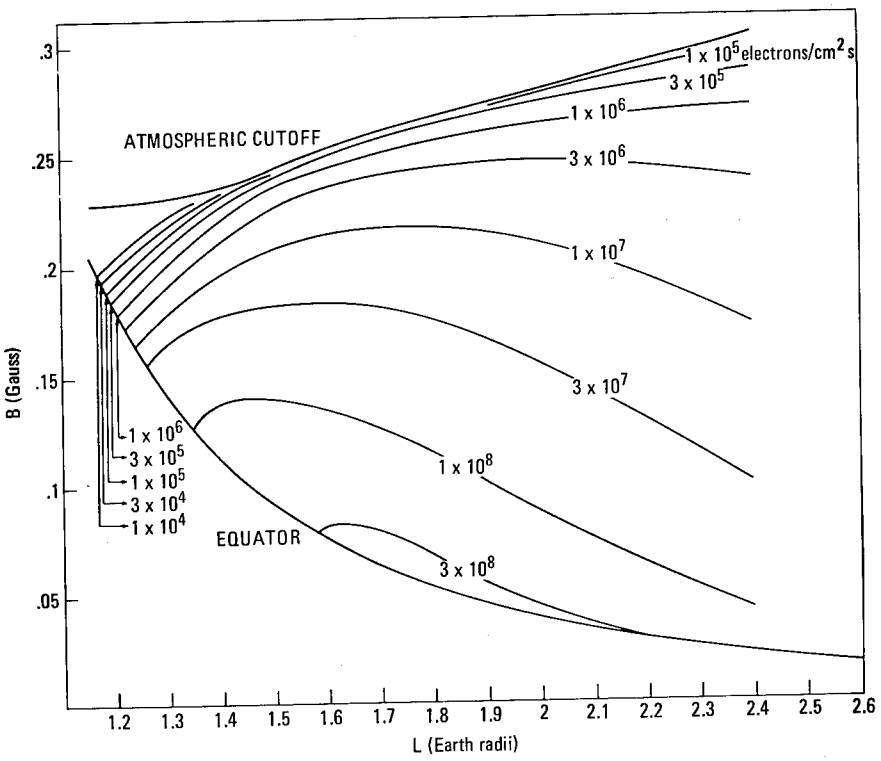

a. E > 40 keV, Epoch October 1967

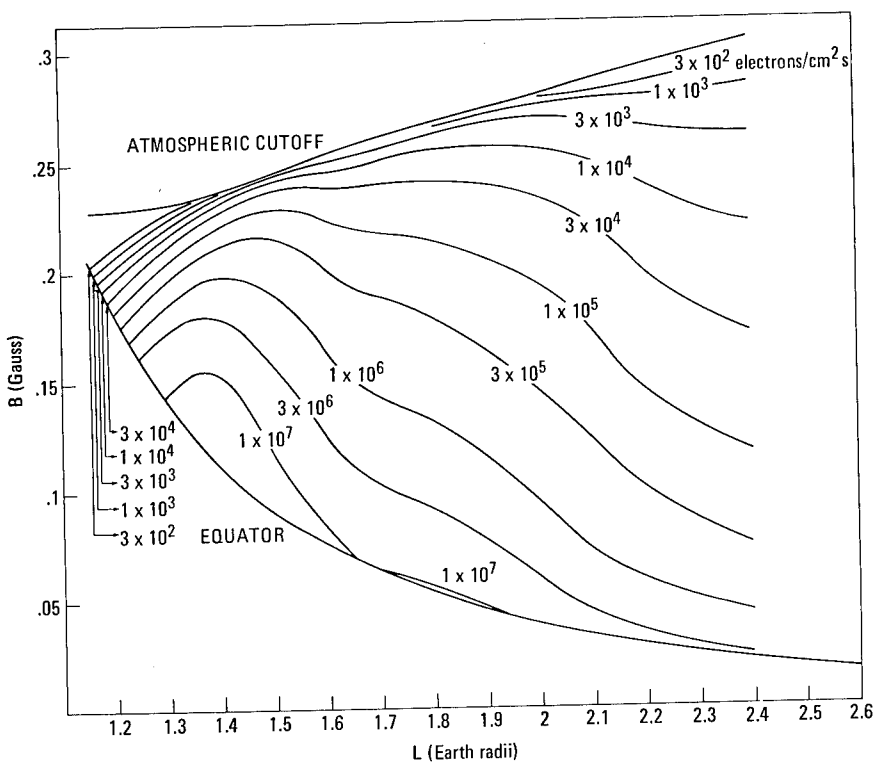

b. E > 500 keV, Epoch October 1967

Figure 30.–Model AE5 (ref. 7) ominidirectional electron flux as function of B and L. (cont.).

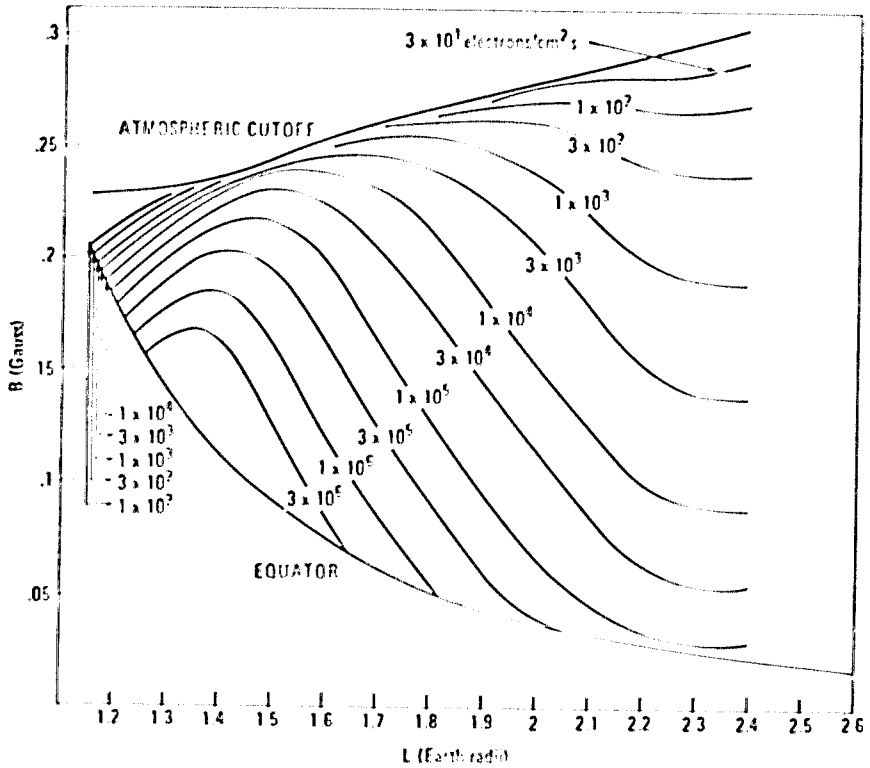

c. E > 1 MeV, Epoch October 1967

Figure 30.—Model AE5 omnidirectional electron flux as function of B and L (ref. 7).

Model AE5 includes temporal behavior attributable to solar cycle effect and decay of Starfish electrons. Variations in the flux caused by solar cycle effects can be estimated by values of the solar cycle parameter R_1 defined as the ratio of the flux at the epoch of October 1967 to that at time T measured in months from solar minimum (assumed to be September 1964), that is

$$R_1\ (E,L,T) = \frac{J\ (E,L,T = \text{October } 1967)}{J(E,L,T)}$$

Plots of R_1 (L,T) are given in figure 32 for energy thresholds of 40, 100, 250, and 500 keV. Above E = 500 keV, the solar cycle effect is small in comparison to the effects of magnetic storms.

Model AE5 contains a small Starfish residual flux in the energy range 500 keV $\leq$ E $\leq$ 3 MeV and the L range $1.2 < L < 1.5\ R_e$. In the foregoing L and E region of Model AE5 that is influenced by Starfish electrons, it is estimated that a maximum reduction factor of 10 should be used to account for the decay of this component.

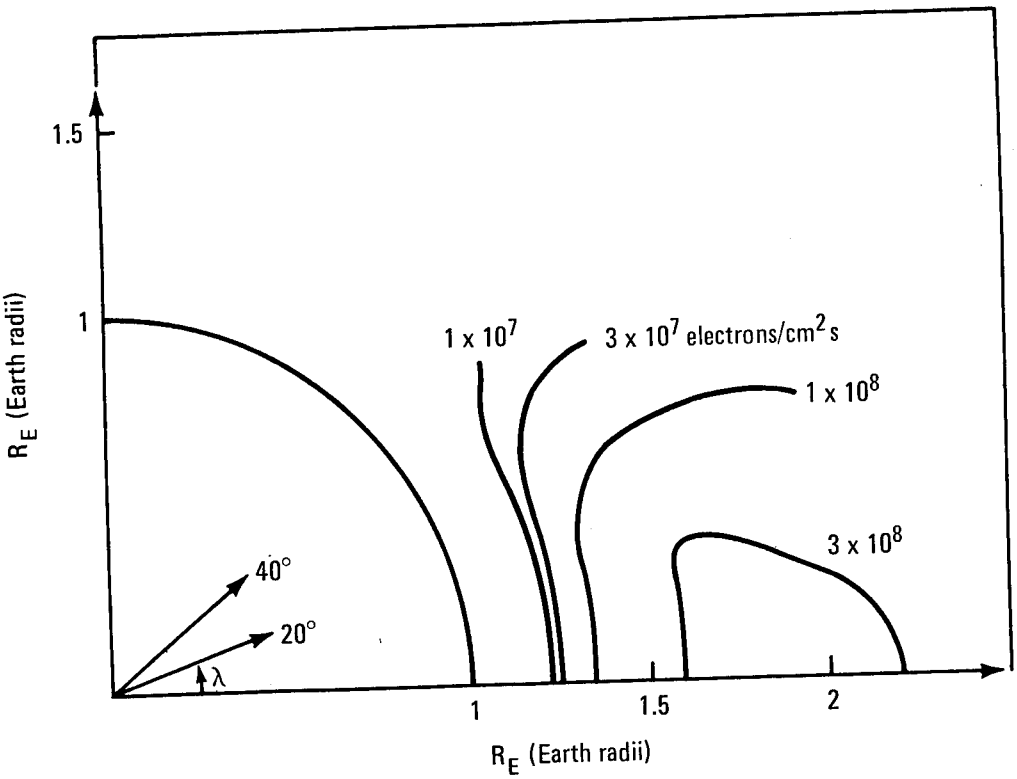

a. E > 40 keV

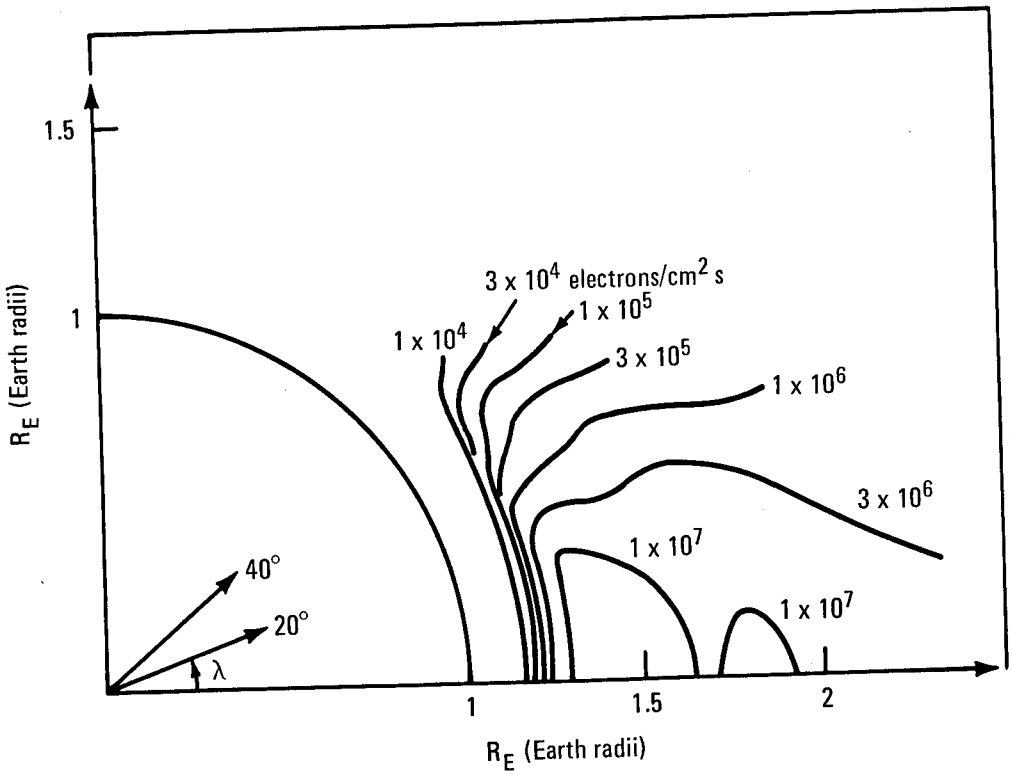

b. E > 500 keV

Figure 31.—Model AE5 (ref. 7) omnidirectional electron flux as function of R_E and latitude λ (cont.).

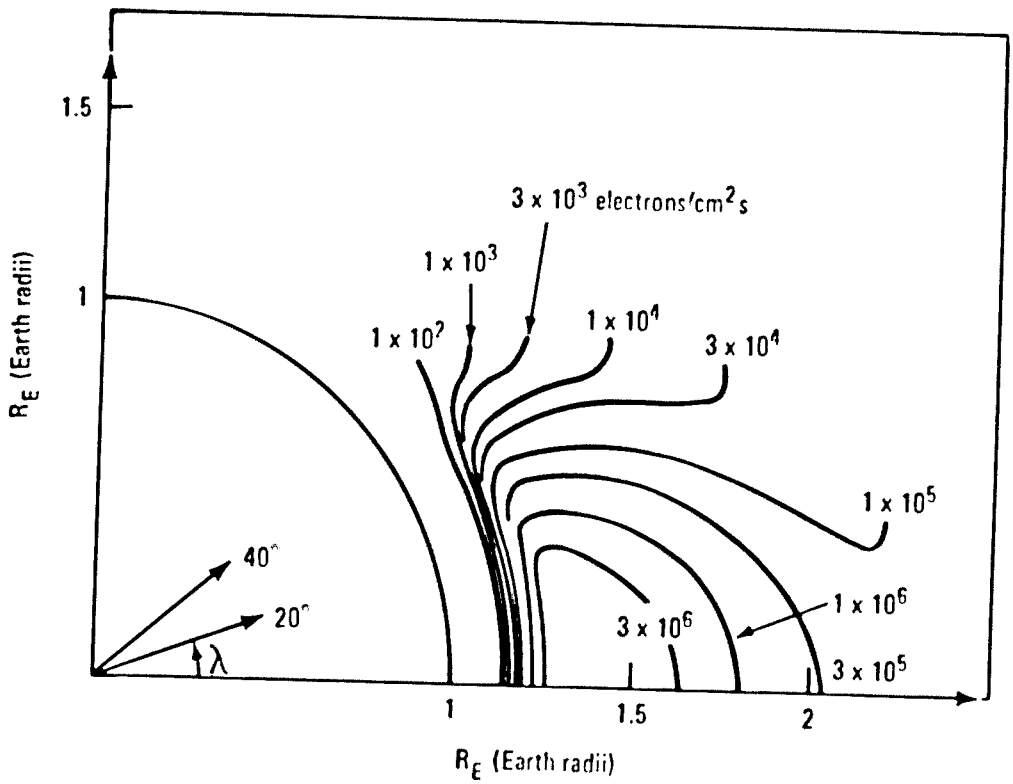

c. $E > 1$ MeV

Figure 31.—Model AE5 omnidirectional electron flux as function of R_E and latitude λ (ref. 7).

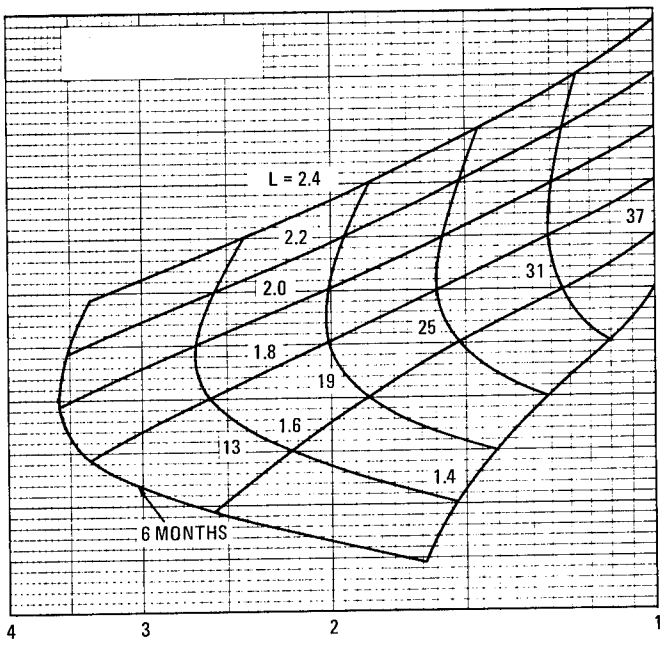

$$\frac{\text{INTEGRAL FLUX, OCT. 1967}}{\text{INTEGRAL FLUX, TIME T}} (R_T)$$

a. E > 40 keV, at 6 month and 0.2 L intervals

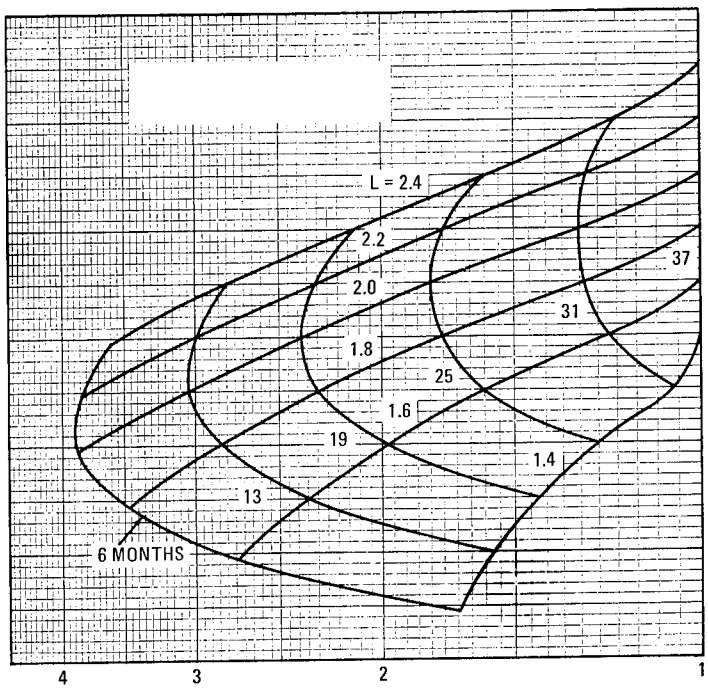

$$\frac{\text{INTEGRAL FLUX, OCT. 1967}}{\text{INTEGRAL FLUX, TIME T}} (R_T)$$

b. E > 100 keV, at 6 month and 0.2 L intervals

Figure 32.—Integral flux solar cycle ratios R_T from reference 7. (cont.).

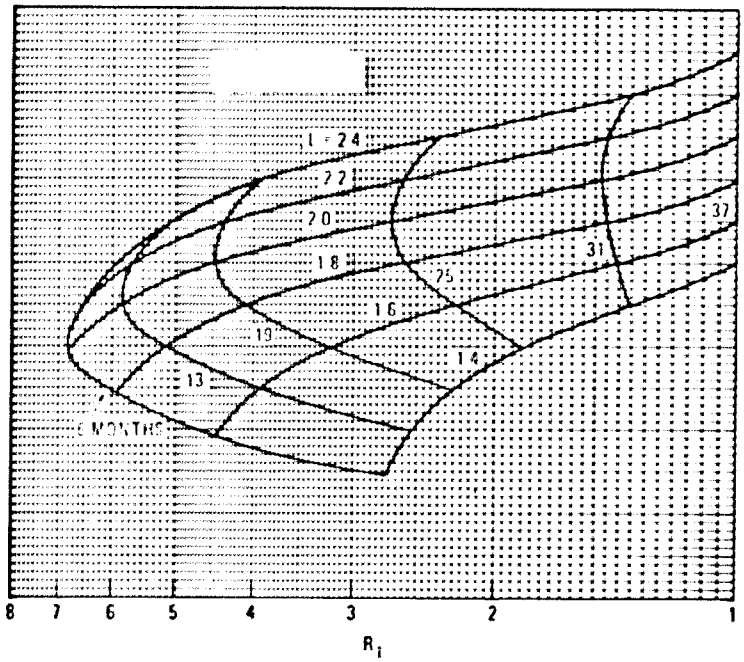

c. E > 250 keV, at 6 month and 0.2 L intervals

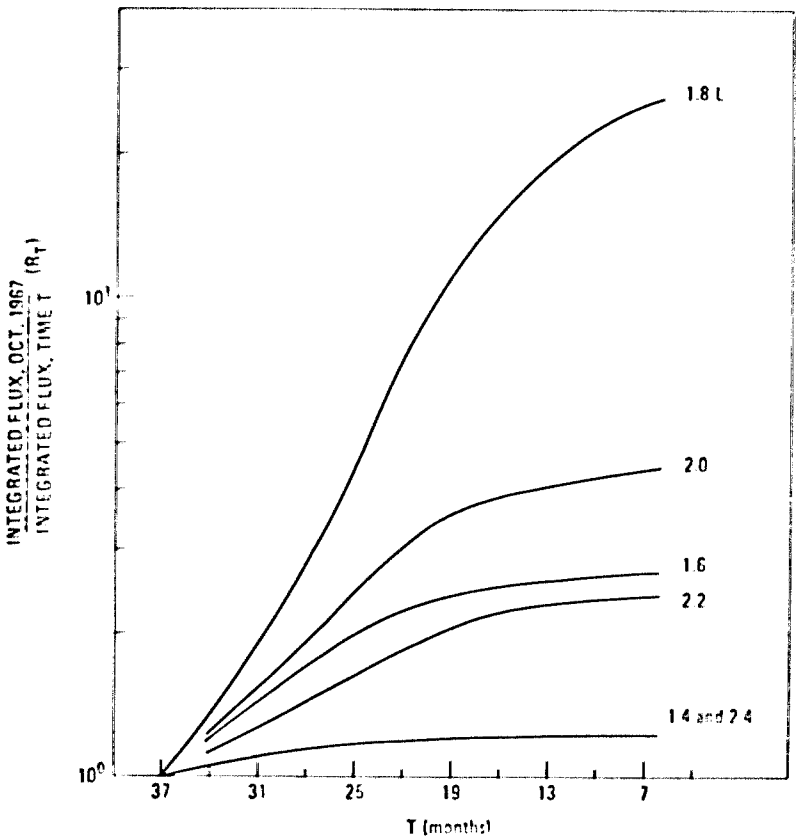

d. E > 500 keV

Figure 32.–Integral flux solar cycle ratios R_T (ref. 7).

To enable the user to assess the reliability of the model AE5, a system of confidence codes is included. In general, efforts have been made to provide pessimistic flux estimates where low confidence codes are given which state that it is more probable that the flux is lower than the quoted value rather than higher. Two sets of codes are given—one for the omnidirectional flux at an epoch of October 1967 (table 6) and one for the integral flux solar cycle parameters (table 7).

Table 6.
Omnidirectional Flux Confidence Limits (ref. 7).

Confidence Code*	B Range**	L Range	E Range	Comment
1	$>B_o$	1.2-1.4	>3 MeV	Extrapolation on both B dependence and spectrum, no data
2	$\sim B_o$	1.2-1.4	>3 MeV	Extrapolation on spectrum, no data
4	$\geqslant B_o$	1.2-1.7	>250 keV	Possible presence of Starfish electrons
5	$\geqslant B_o$	1.9-1.4	4-2 MeV	Magnetic storm effects, single data set, B extrapolation
6	$>B_o$	1.7-1.9	>500 keV	Single data set, B extrapolation
6	$\geqslant B_o$	<1.25	all energies	L extrapolation
6	$\sim B_o$	>1.5	all energies	Poor data
7	$\geqslant B_o$	1.3	all energies	Poor OGO data
8	$>>B_o$	>2	all energies	Poor pitch angle coverage
10	$\geqslant B_o$	1.4-1.9	<250 keV	Agreement between three data sets

*Larger number denotes increasing reliability.
**B_o magnetic field strength on equatorial plane.

Table 7.
Integral Flux Solar Cycle Parameter Confidence Limits (ref. 7).

Confidence Code*	L Range	E (keV)	T**	Comment
3	<1.8	250, 500	>22	Significant Starfish flux 22 months after solar minimum of Sept. 1964
4	>1.9	all	all	Poor OGO data at high L values
4	all	40	all	Small R_T values
5	<1.4	250, 500	all	Hardening of spectrum
5	>1.8	500	all	Storm contributions to R_T become significant
7	1.6-2.0	250, 500	all	Two data sets available, i.e., OGO and 1963-38C

*Larger number denotes increasing reliability
**Time in solar cycle that began September 1964.

3.1.2 Outer Belt, 5 MeV > E > 0.05 MeV (Model AE4)

Model AE4 should be applied for electrons with energies in the range of 50 keV to 5.0 MeV between L = 3.0 and 11.0 R_E. This model which is based on data obtained between 1959 and 1968 includes pseudotrapped regions that have substantial fluxes of short-lived particles. Discernible changes in the average flux over the time period studied were attributed to solar cycle effects. To account for these changes, model AE4 is given for two epochs. The first epoch, 1964, represents conditions at solar minimum; the second, 1967, represents conditions near solar maximum.

Time-averaged values of the electron flux were prepared to average out the effects of magnetic storms. The standard B-L coordinate system was used; however, this system loses its physical meaning in many parts of the spatial region considered because of distortion in the Earth's magnetic field. For convenience, B/B_o (where B_o is the equatorial magnetic field strength) was used as the magnetic variable instead of B.

The time-averaged omnidirectional flux for energy greater than E is given by

$$J\,[>E, B, L, \phi, T] = N_T\,[>E, L]\;\phi_T\,[>E, L, \phi]\;G\,[B, L]$$

where N is spectral function

- G is the model dependence on B
- ϕ is the local time variation
- T is the epoch

Integral energy spectra for constant L values are shown in figure 33. Similar figures for differential energy spectra are given in reference 6. Tabulated values of both the integral and differential spectral functions N are given in table 1 of reference 6.

Model AE4 local time variation is represented analytically by

$$\phi_T\,[E, L, \phi] = K_T\,[E, L]\,10^{C_T[E,L]\cos\frac{\pi}{2}(\phi - 11)}$$

where $K_T\,[E, L]$ is a factor normalizing the average of the function to 1. ϕ_T represents the variation with local time of flux levels from average flux levels. The coefficients K_T and C_T are presented in figures 34 and 35. Tabulated values are given in table 2 of reference 6.

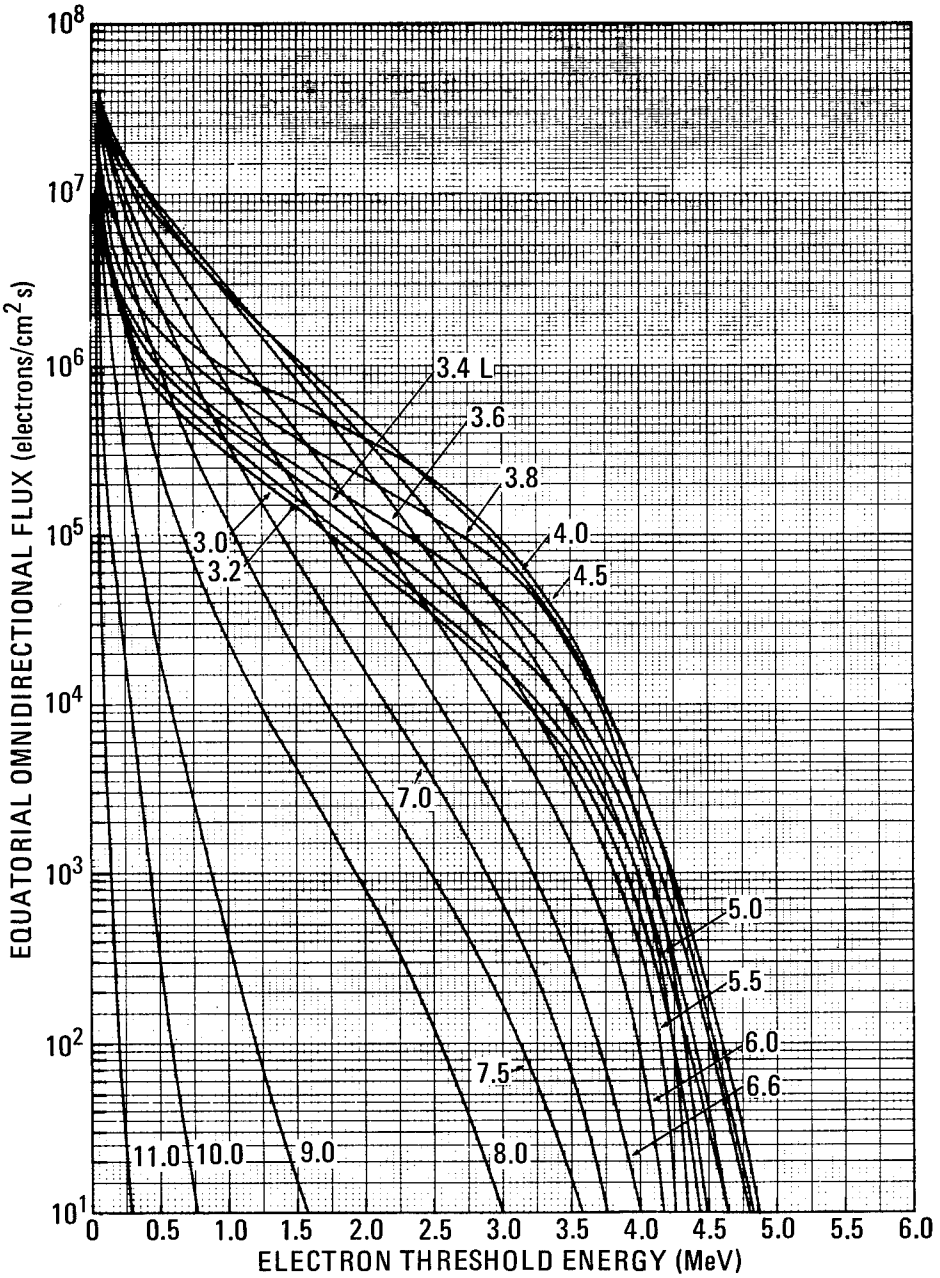

a. Epoch 1964

Figure 33.—Model AE4 (ref. 6) integral electron spectra as function of L. (cont.).

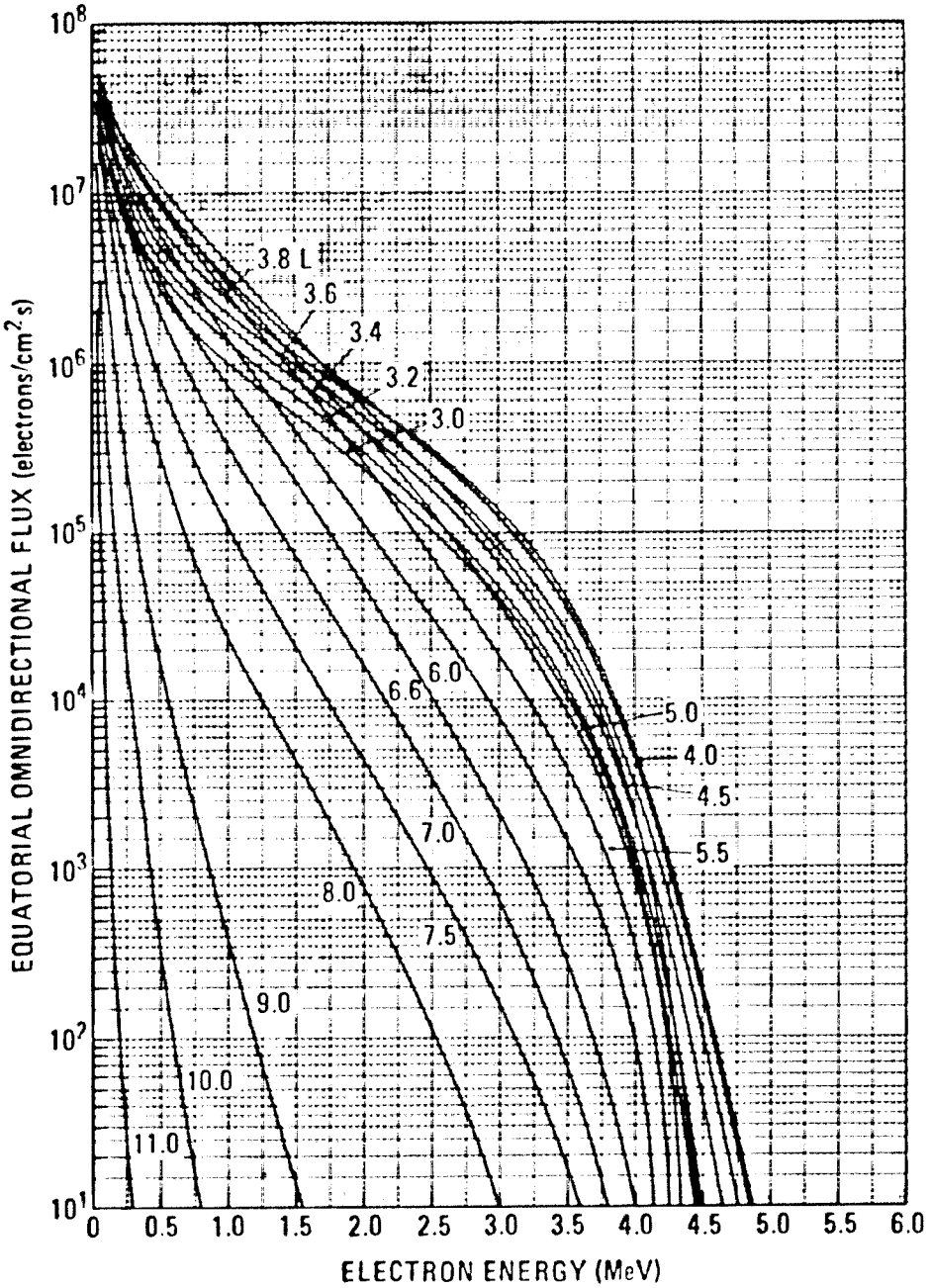

b. Epoch 1967

Figure 33.–Model AE4 integral electron spectra as function of L (ref. 6).

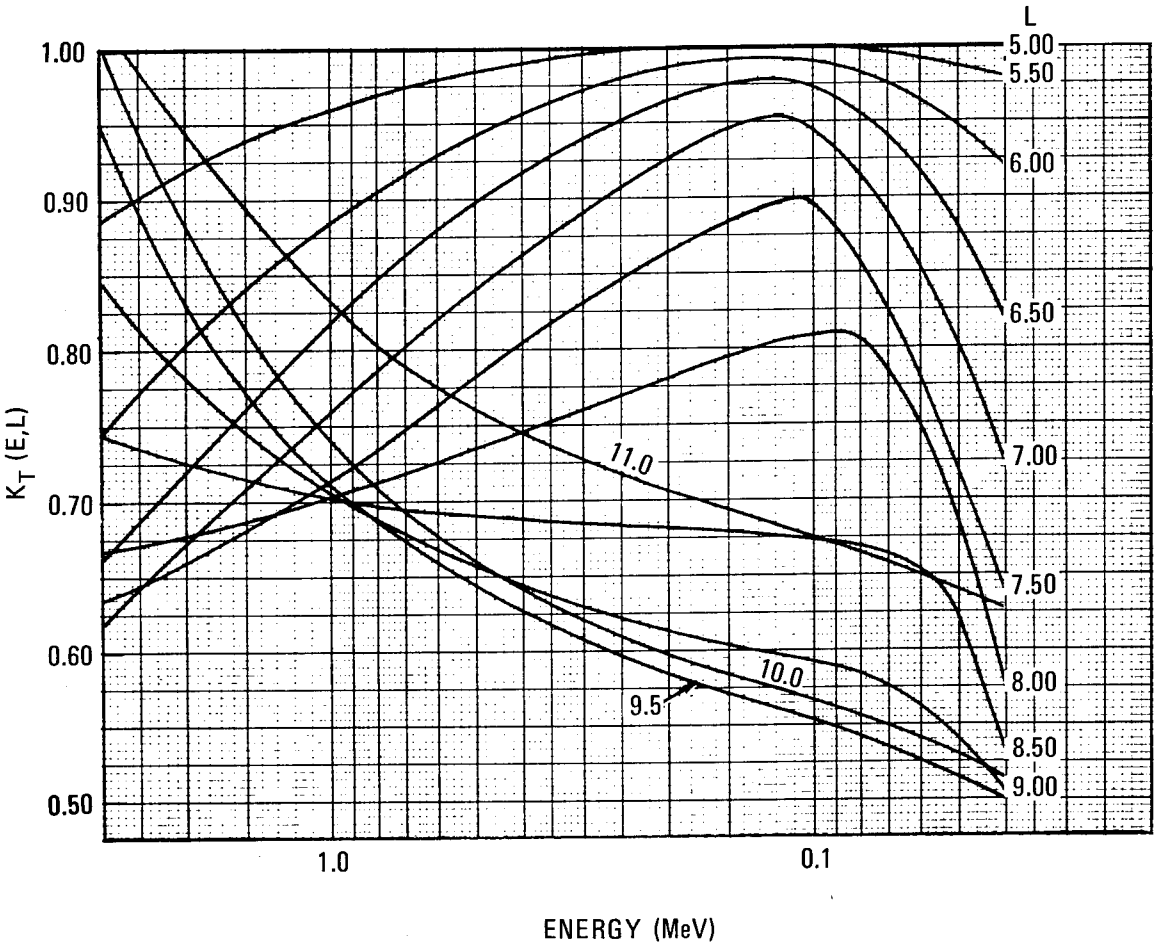

a. Epoch 1964

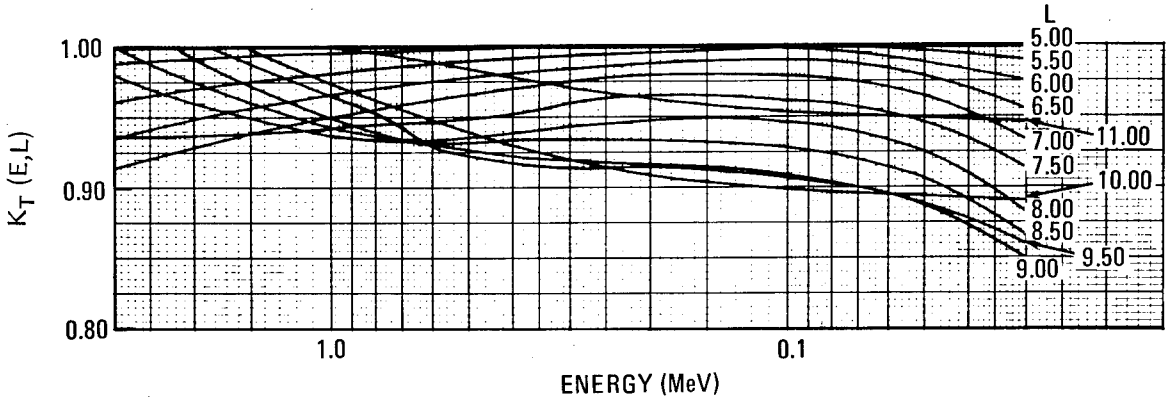

b. Epoch 1967

Figure 34.—Model AE4 local time model normalization factor K_T as function of energy E and L (ref. 6).

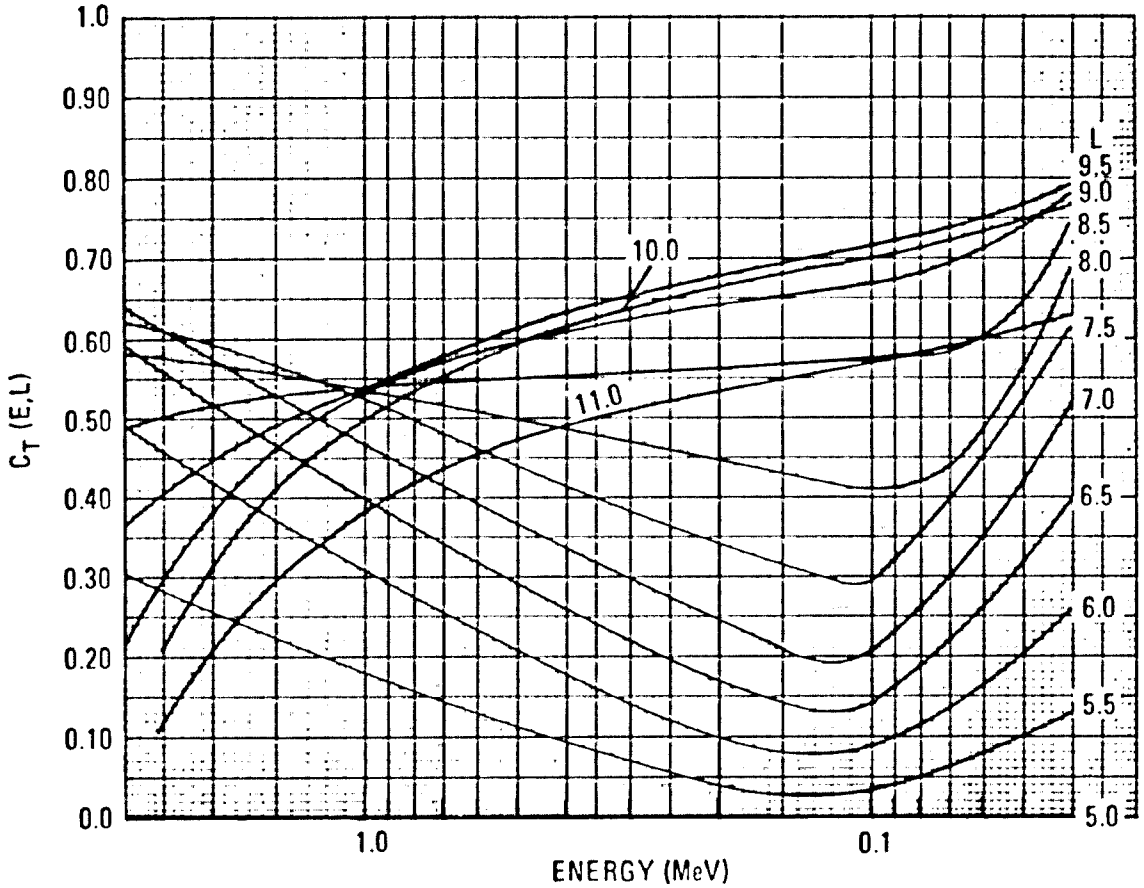

a. Epoch 1964

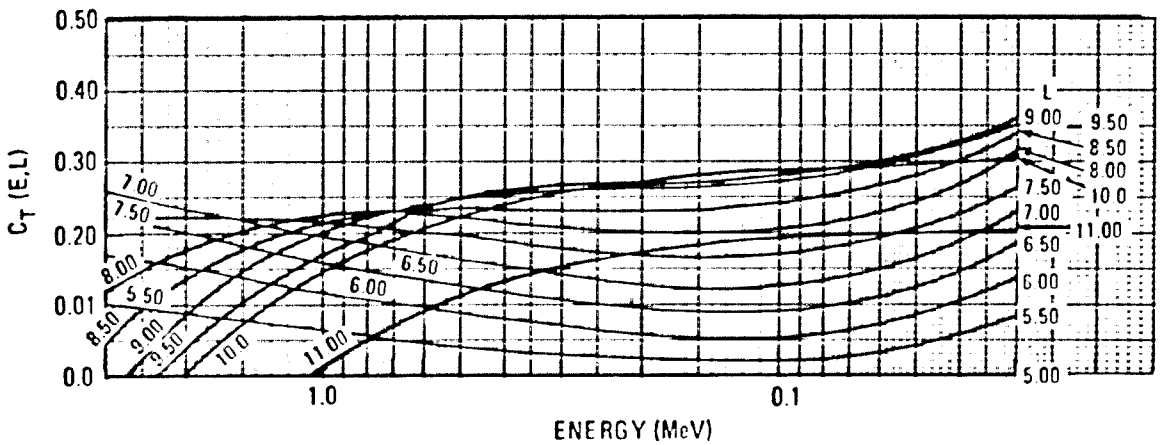

b. Epoch 1967

Figure 35.–Model AE4 local time model amplitude coefficient C_T as function of energy E and L (ref. 6).

The model dependence on B was assumed to be a power law function with no energy or time dependence. Then

$$G[B,L] = \begin{cases} [B/B_o(L)]^{-m(L)} \left[\dfrac{B_c(L) - B}{B_c(L) - B_o(L)}\right]^{m(L)+0.5} & \text{for } B < B_c \\ 0 & \text{for } B \geq B_c \end{cases}$$

where $B_c(L)$ is the magnetic cutoff assumed for the model. Parameters used in evaluating G(B,L) are given in table 8.

Table 8.
Parameters for Evaluation of B and L Variation (Model AE4) (ref. 6).

L (R_E)	m*	Equatorial Magnetic Field Strength, B_o** (Gauss)	Assumed Magnetic Cutoff, B_c (Gauss)
3.00	1.12	.01154	0.580
3.10	0.87	.01046	0.582
3.20	0.71	.009511	0.585
3.40	0.66	.007929	0.588
3.60	0.63	.006680	0.593
4.00	0.60	.004870	0.596
4.50	0.60	.003420	0.599
5.00	0.60	.002493	0.600
5.50	0.60	.001873	0.601
6.00	0.60	.001443	0.601
6.50	0.60	.001134	0.602
7.00	0.60	.000909	0.602
7.50	0.60	.000739	0.603
8.00	0.60	.000609	0.603
8.50	0.60	.000507	0.6035
9.00	0.57	.000428	0.6035
9.50	0.52	.000363	0.604
10.00	0.44	.000312	0.604
10.50	0.35	.000269	0.604
11.00	0.24	.000234	0.604

*L-dependent power law exponent for determining dependence of model on B

**$B_o = \dfrac{.311654}{L^3}$

The local time-averaged omnidirectional flux map for model AE4 is presented in B and L coordinates for Epoch 1964 in figure 36 and for Epoch 1967 in figure 37. The map is also shown in R_i and latitude λ coordinates for Epoch 1964 in figure 38 and for Epoch 1967 in figure 39.

Because time variations are significant, the time-averaged values of the energy spectrum are valid only for periods of several weeks or longer. For shorter periods, it is necessary to develop a model which reflects the time variations caused by solar events and by changes in the interplanetary medium. These are best treated with a statistical model. On this basis, the probability of occurrence of a certain flux was investigated. It was found that the logarithm of the flux can be adequately represented by a Gaussian distribution. In accordance with reference 113, the probability that the flux will exceed a threshold J_1 was developed from the Gaussian fit as

$$P(J > J_1) = \frac{1}{\sqrt{2\pi}\,\sigma} \int_{\log_{10} J_1}^{\infty} \exp\left[-\left(\frac{x-\mu}{2}\right)^2\right] dx$$

where

$$x = \log_{10}(J[> E,B,L,\phi,t])$$

(t is time at instantaneous value of J)

$$\mu = \log_{10}(J[> E,B,L,\phi,T]) - 1.15\sigma^2\,[E,L]$$

The standard deviation σ for model AE4 is given in figure 40. It is valid for both epochs. Tabulations of flux levels that will be exceeded with given probabilities for the two epochs are presented in tables 6 and 7 of reference 6.

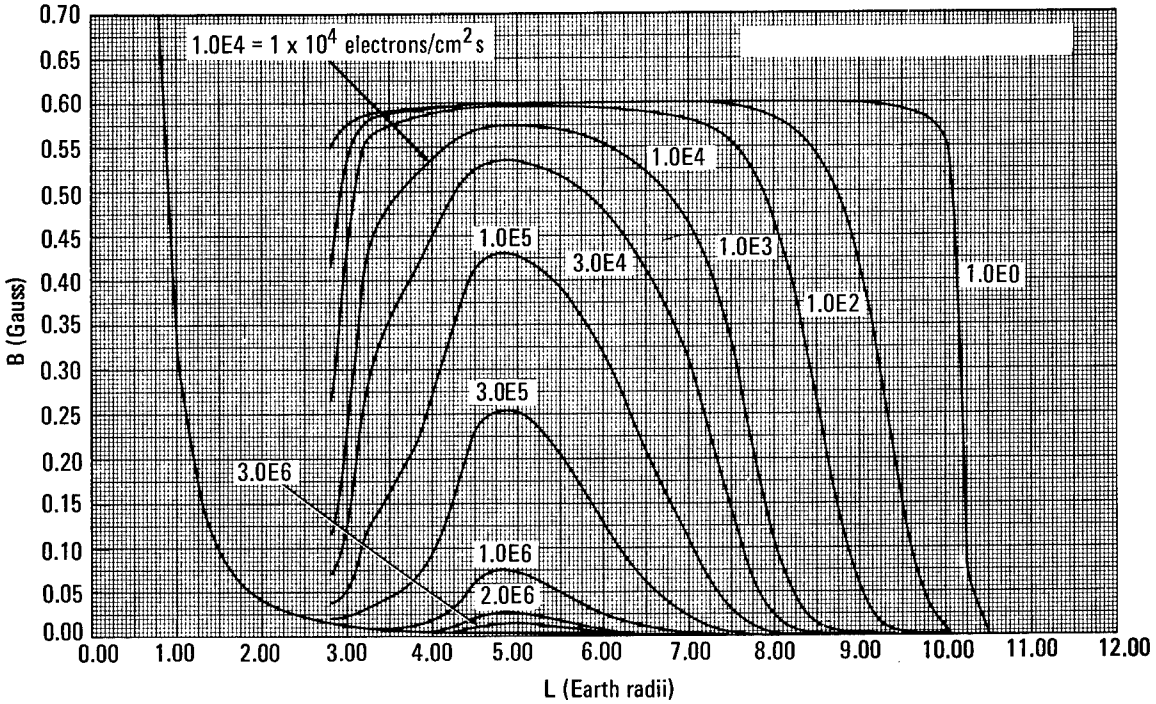

a. E > 0.5 MeV

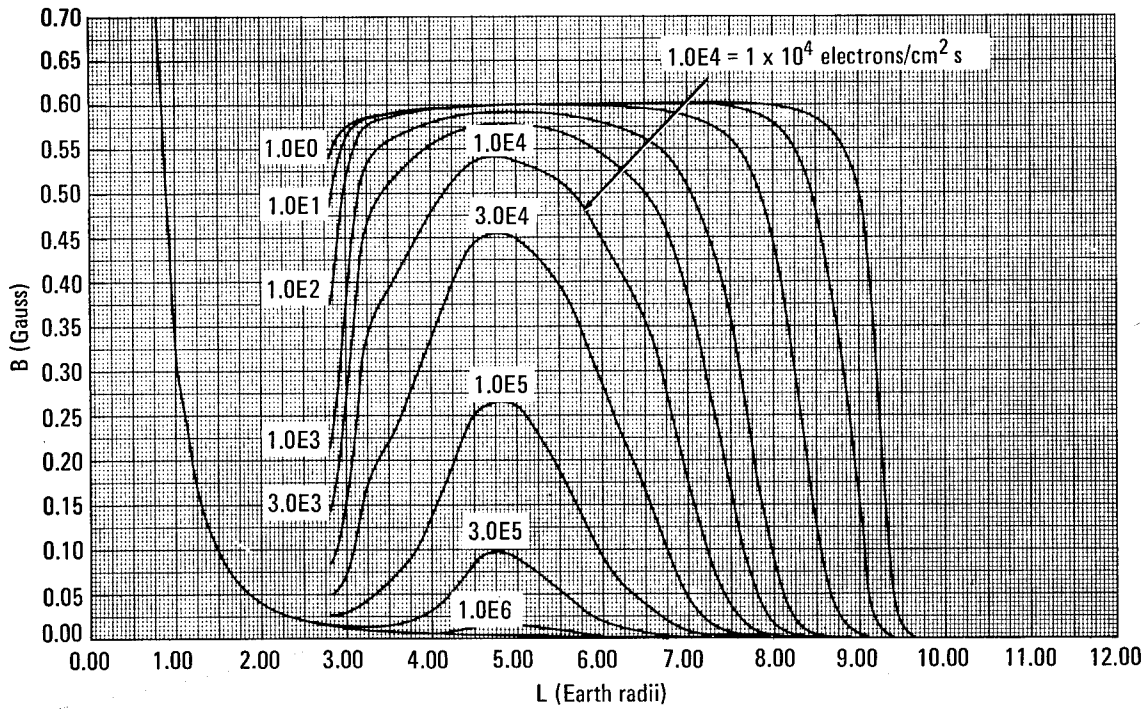

b. E > 1.0 MeV

Figure 36.—Model AE4 (ref. 6) omnidirectional electron flux for Epoch 1964 as function of B and L. (cont.).

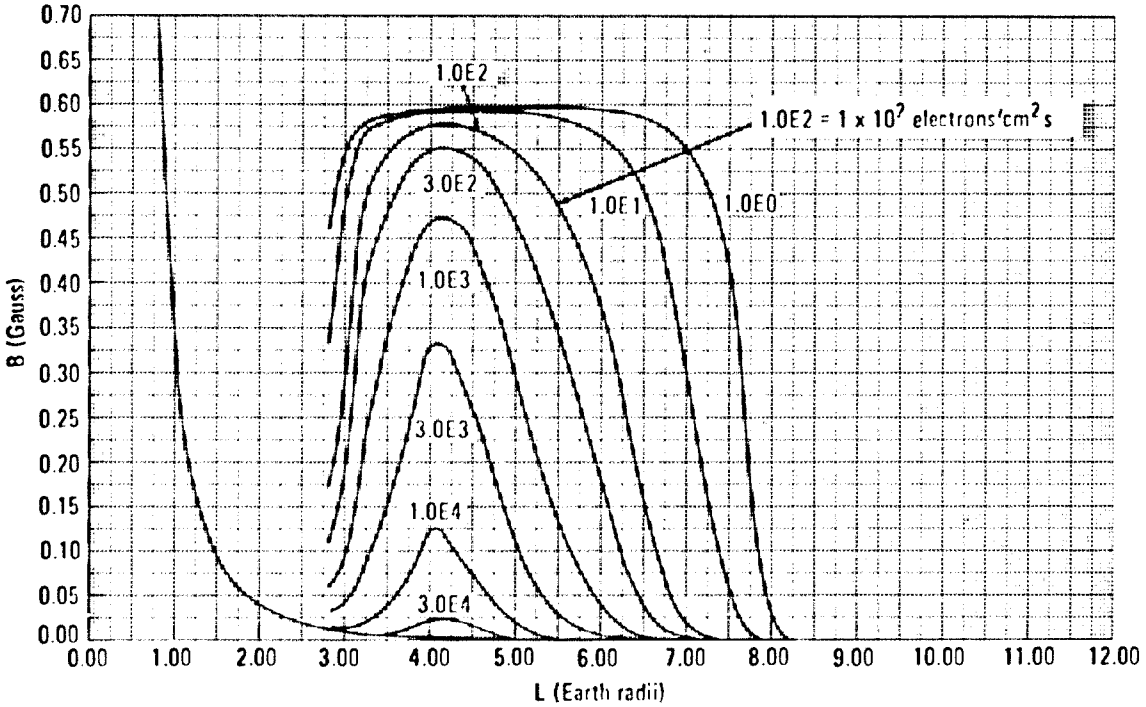

c. E > 3.0 MeV

Figure 36.–Model AE4 omnidirectional electron flux for Epoch 1964 as function of B and L (ref. 6).

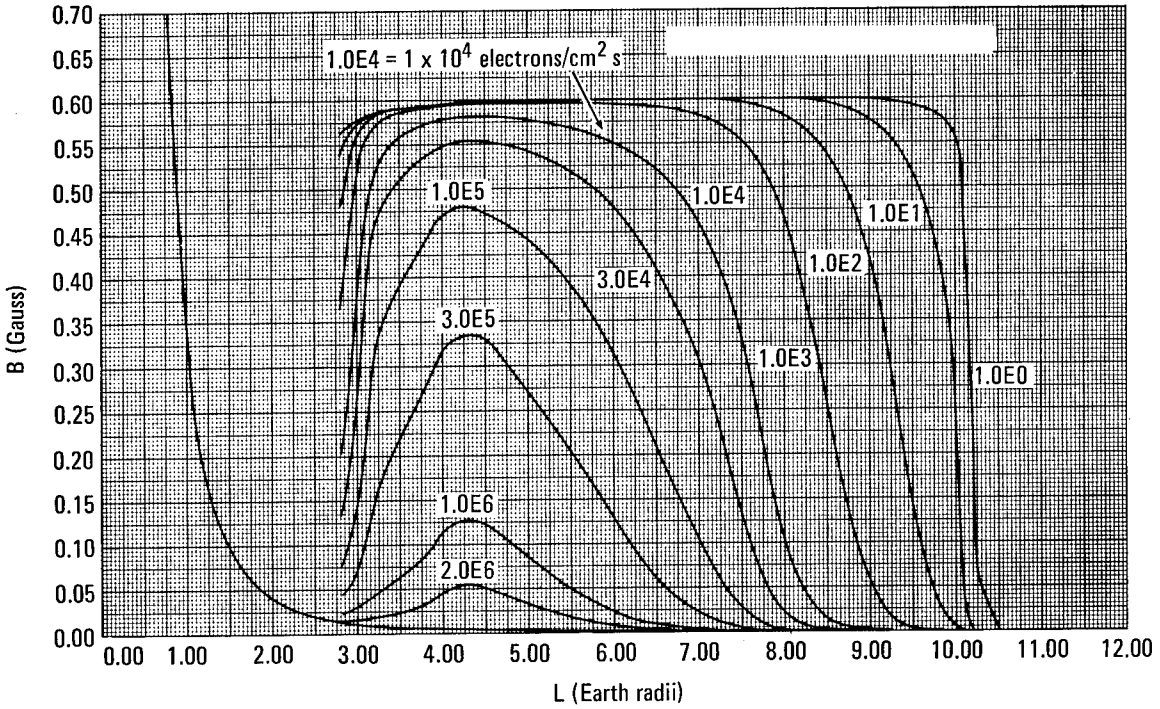

a. E > 0.5 MeV

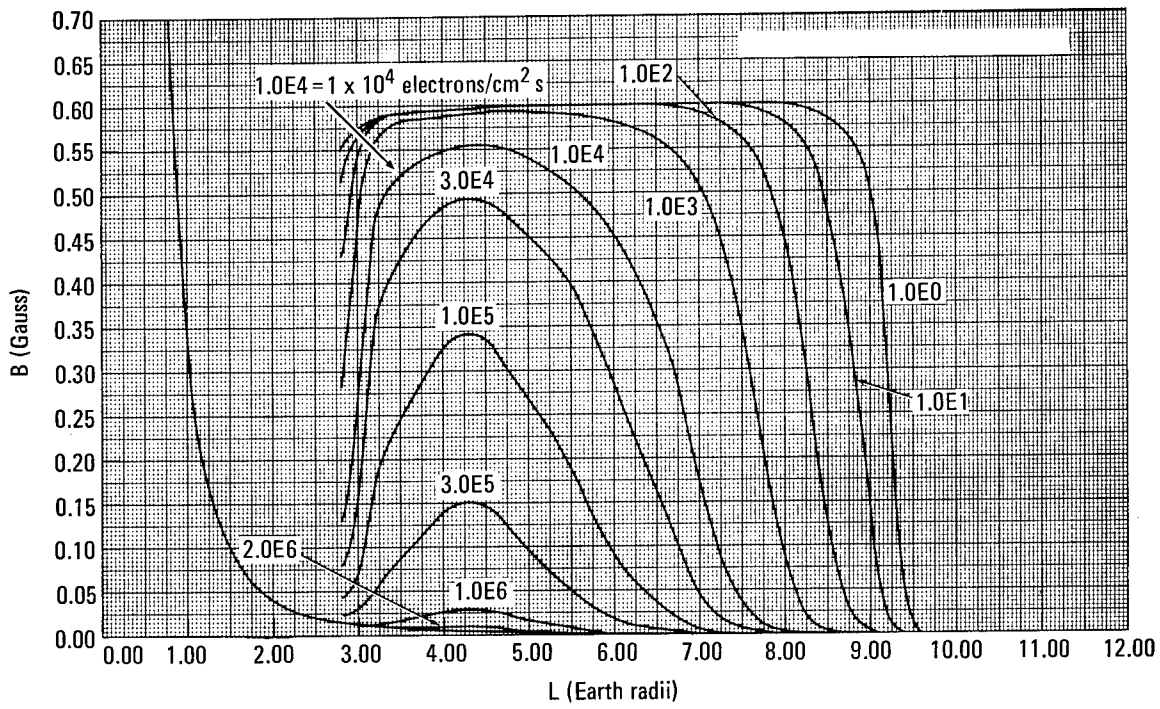

b. E > 1.0 MeV

Figure 37.—Model AE4 (ref. 6) omnidirectional electron flux for Epoch 1967 as function of B and L. (cont.).

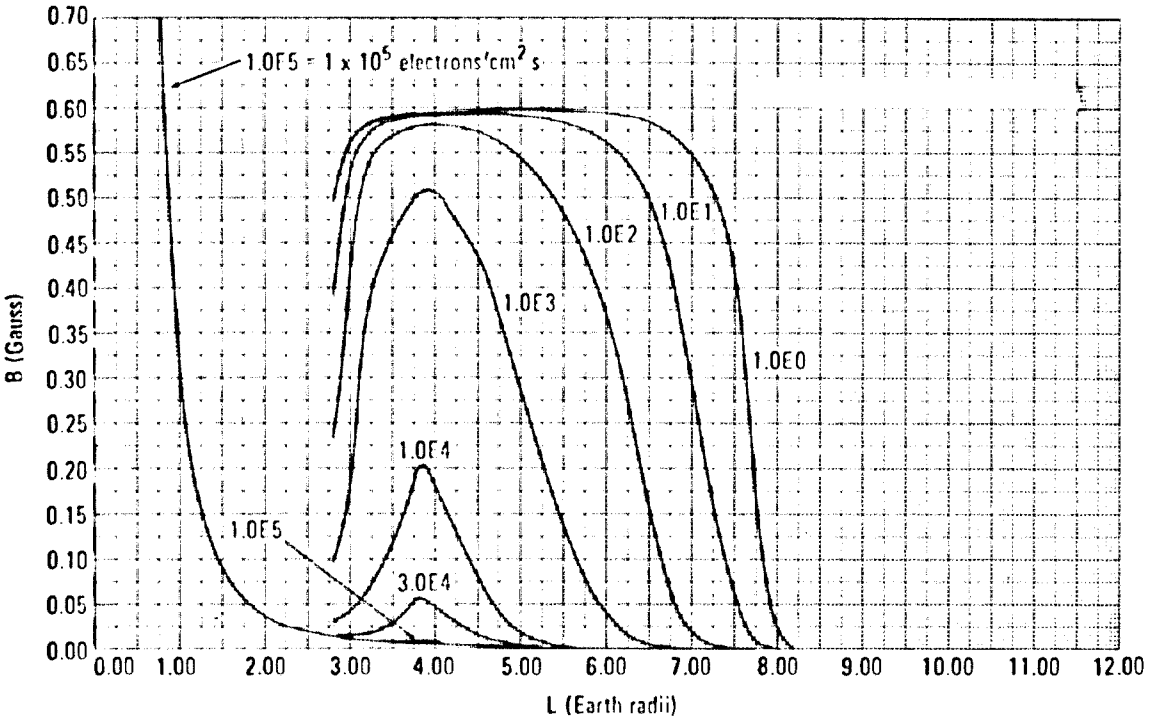

c. E > 3.0 MeV

Figure 37.–Model AE4 omnidirectional electron flux for Epoch 1967 as function of B and L (ref. 6).

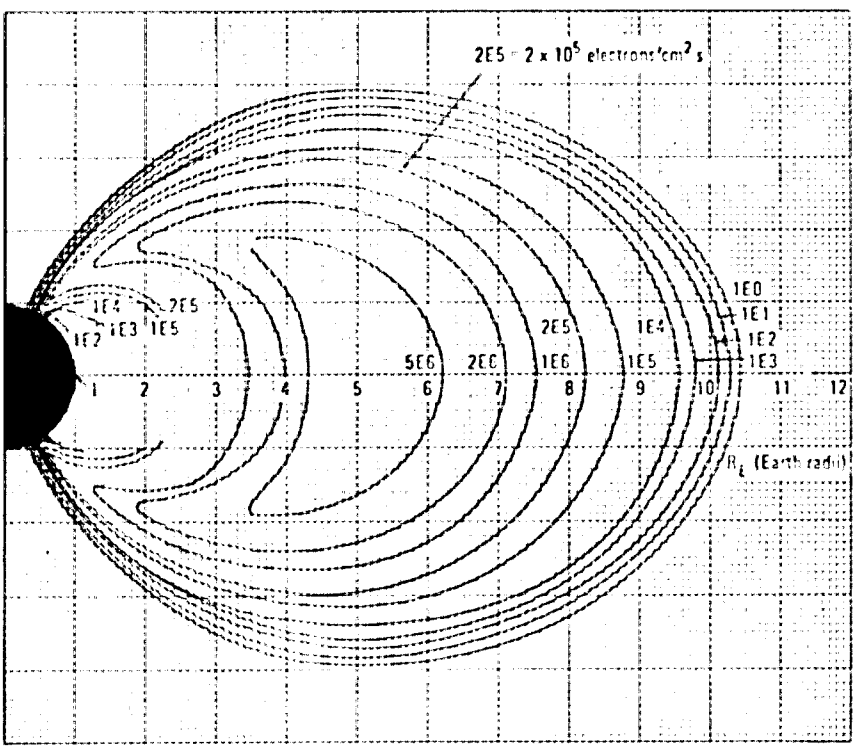

a. E > 0.5 MeV

Figure 38.–Model AE4 (ref. 6) omnidirectional electron flux for Epoch 1964 as function of R_E and latitude. (cont.).

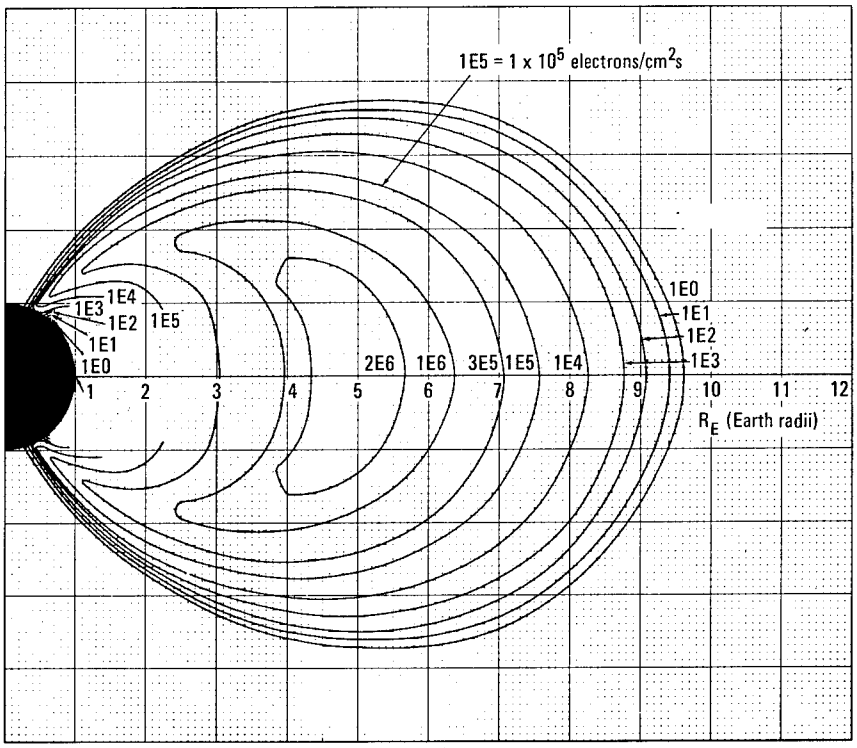

b. E > 1.0 MeV

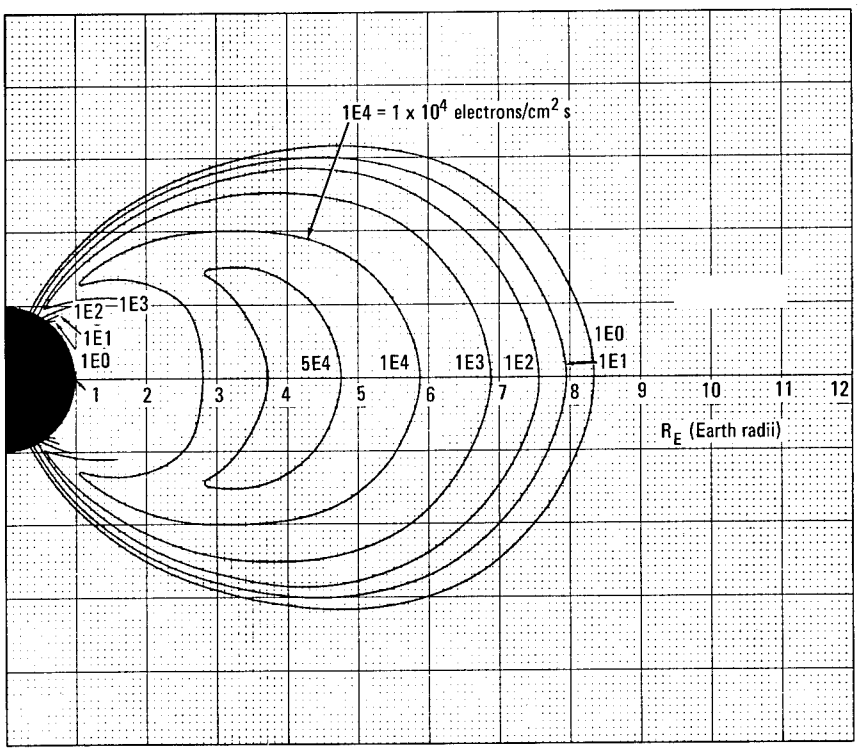

c. E > 3.0 MeV

Figure 38.—Model AE4 omnidirectional electron flux for Epoch 1964 as function of R_E and latitude (ref. 6).

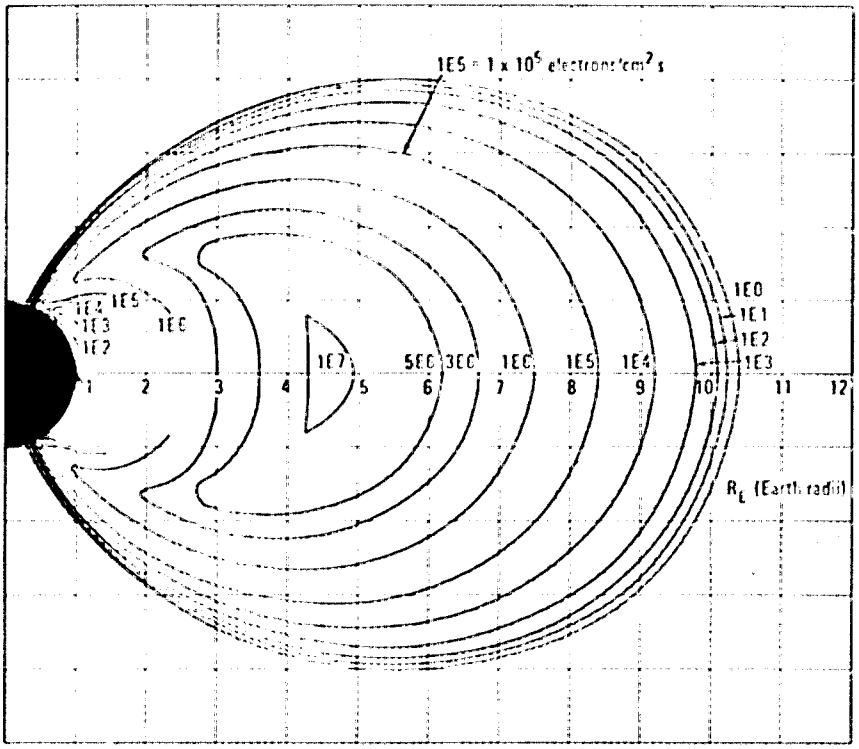

a. $E > 0.5$ MeV

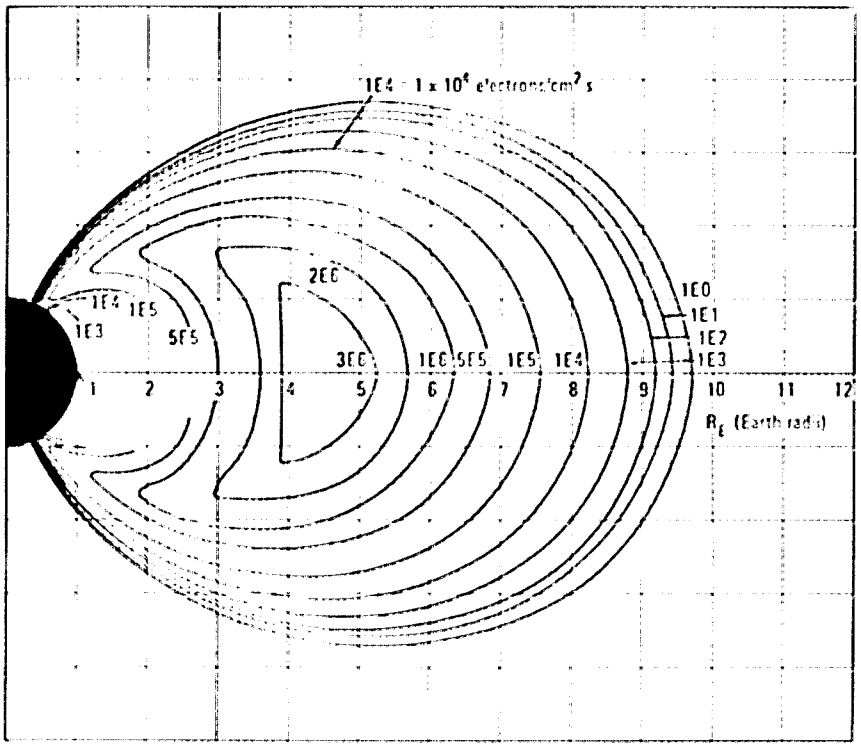

b. $E > 1.0$ MeV

Figure 39.–Model AE4 (ref. 6) omnidirectional electron flux for Epoch 1967 as function of R_E and latitude. (cont.).

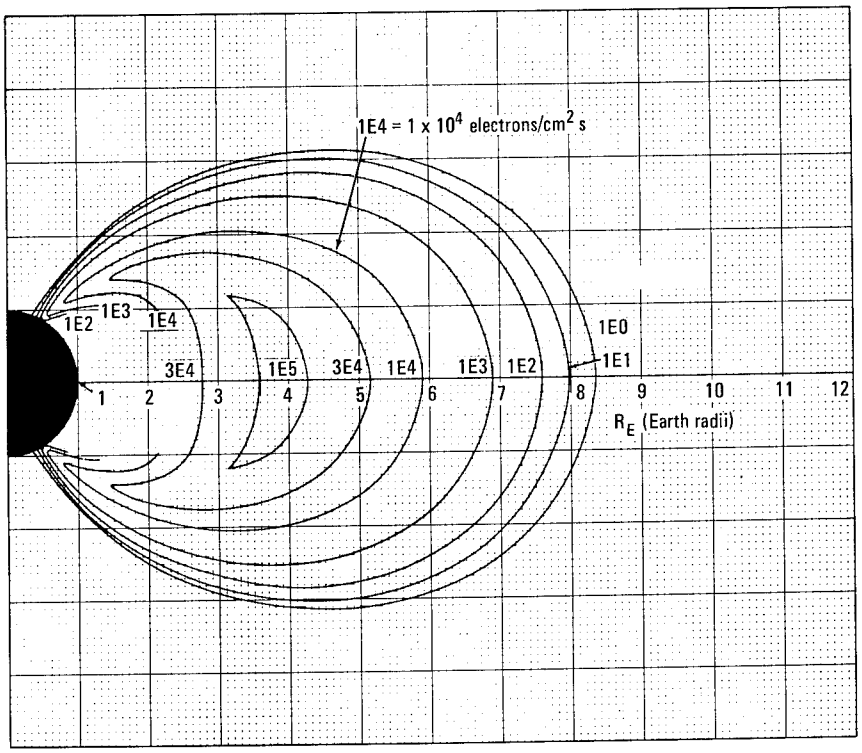

c. $E > 3.0$ MeV

Figure 39.—Model AE4 omnidirectional electron flux for Epoch 1967 as function of R_E and latitude (ref. 6).

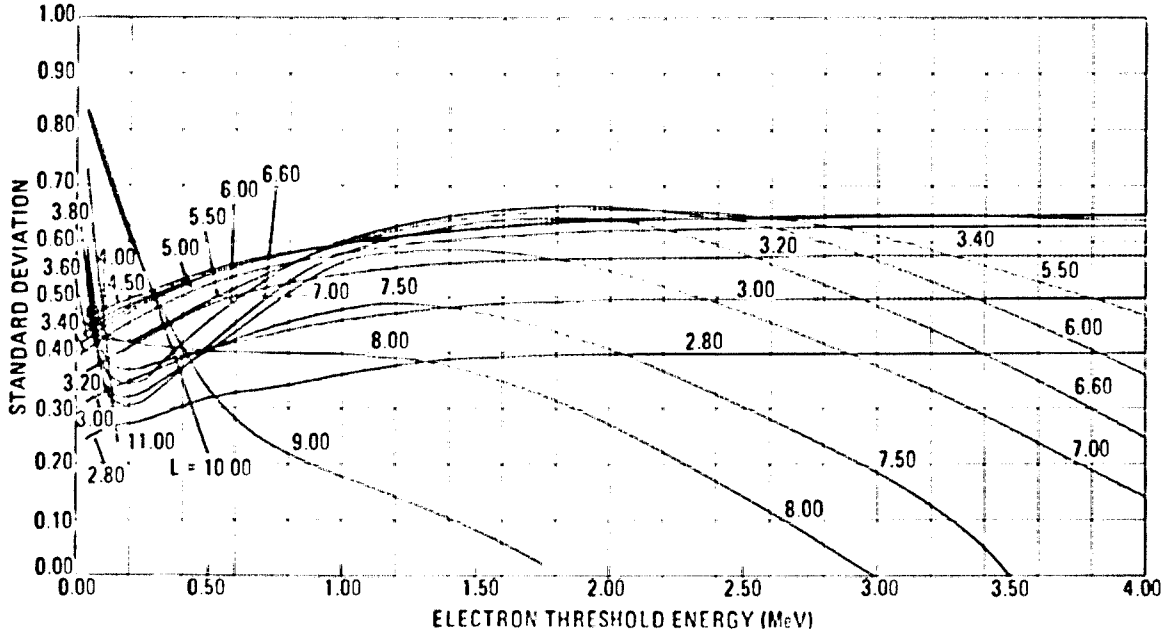

a. Energy variation for constant L

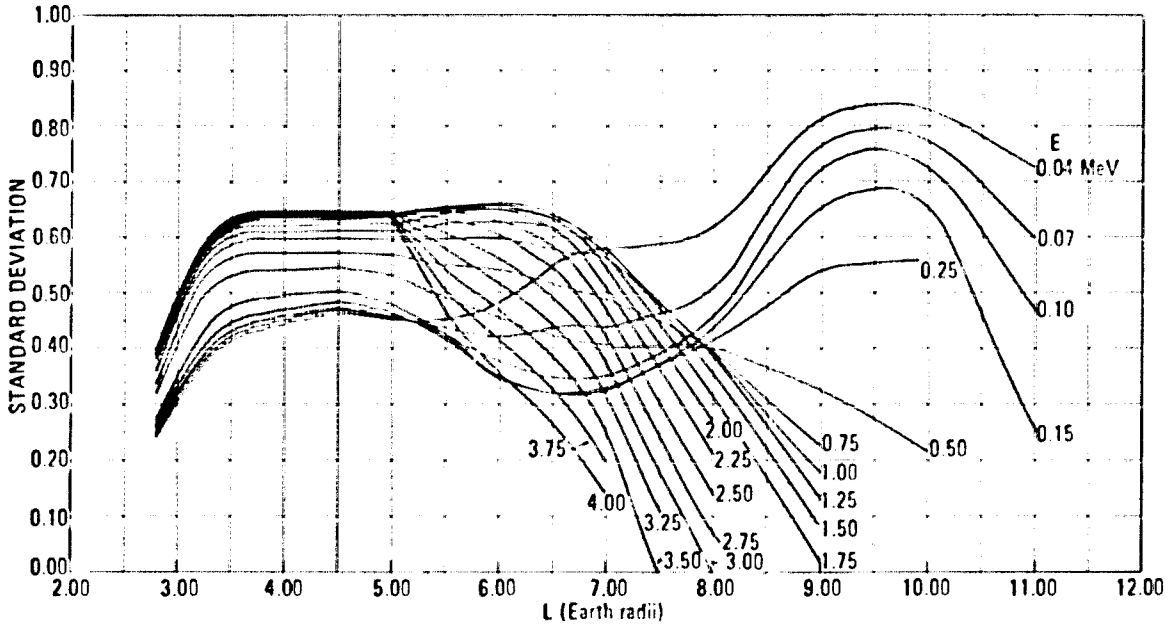

b. L variation for constant energy

Figure 40.—AE4 standard deviation (ref. 6).

3.2 Proton Environment Models

Models AP1 (ref. 112), AP5 (ref. 116), AP6 (ref. 117), and AP7 (ref. 118) are the models of the proton environment in the trapped radiation belt that should be used in the determination of the radiation environment.

3.2.1 Inner Belt, E> 50 MeV (Model AP7)

Model AP7 should be used for protons with energies above 50 MeV between L = 1.15 and 3.0. An exponential representation of the energy spectrum was found to be satisfactory. The spectral function E_0 is shown in figure 41. The omnidirectional flux for E > 50 MeV are shown in figures 42, 43, and 44. Tabulated values of the distribution function are available in table 2 of reference 118.

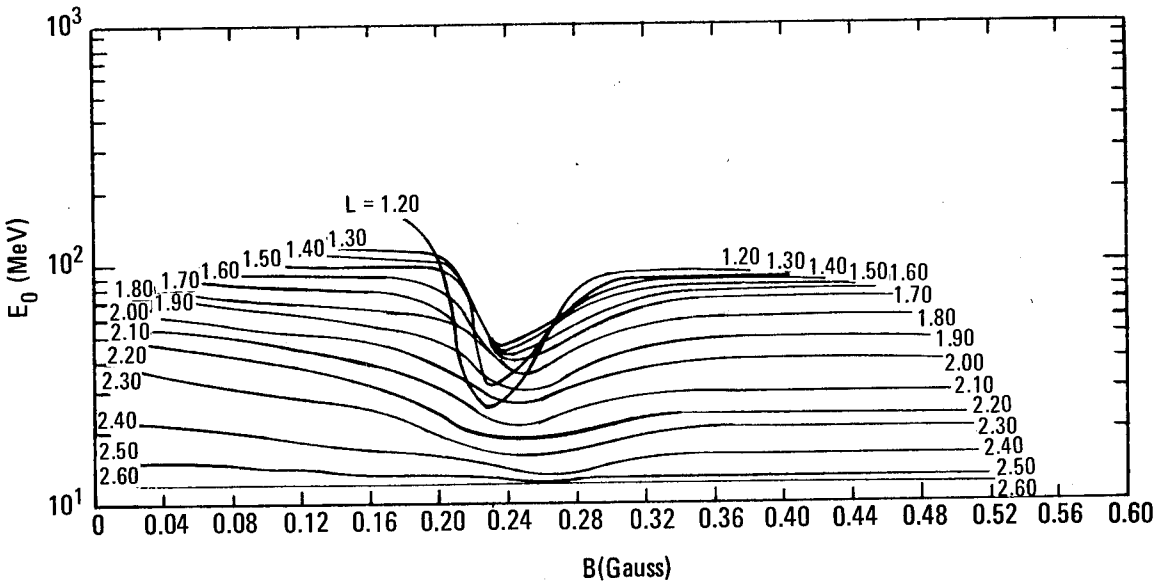

Figure 41.—Spectral parameter E_0 for Model AP7 (ref. 118).

Because the proton flux was found to be very stable, no regular time dependence is included in Model AP7. The model was found to represent the data within a factor of two and should be applied within those limits.

3.2.2 Inner Belt, 30 MeV < E < 50 MeV (Model AP1)

Model AP1 (based on data available up to June 1964) should be applied to inner belt protons in the energy range between 30 and 50 MeV. The energy spectrum of the data was found to vary exponentially. The exponential energy parameter E_0 is shown as a function of field strength in figure 45. The reference energy was chosen as 34 MeV for the omnidirectional flux which is shown in figures 46, 47, and 48. The inner zone proton flux is relatively stable so time variations can be ignored.

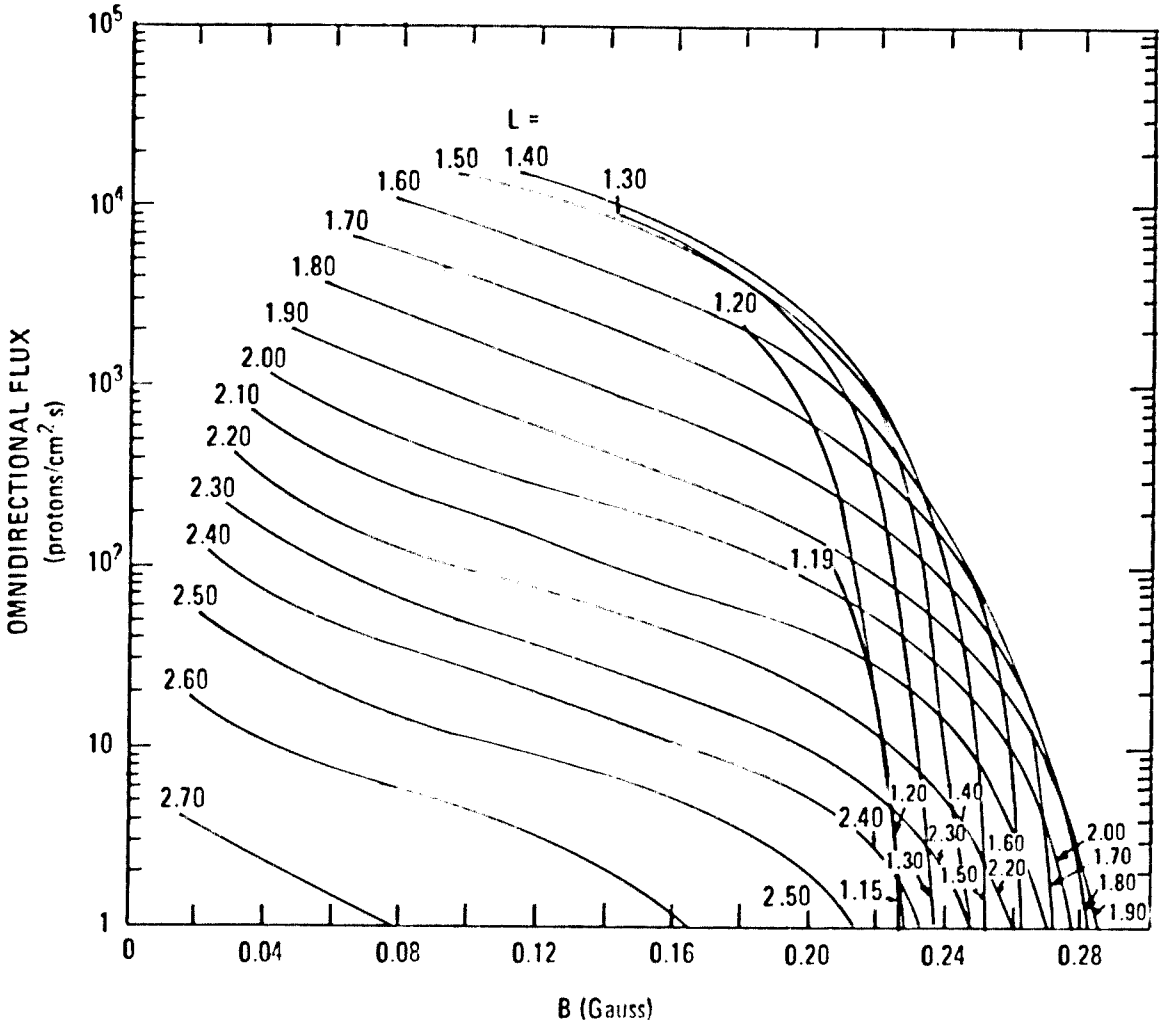

Figure 42.–Omnidirectional flux for Model AP7 (E > 50 MeV) (ref. 118).

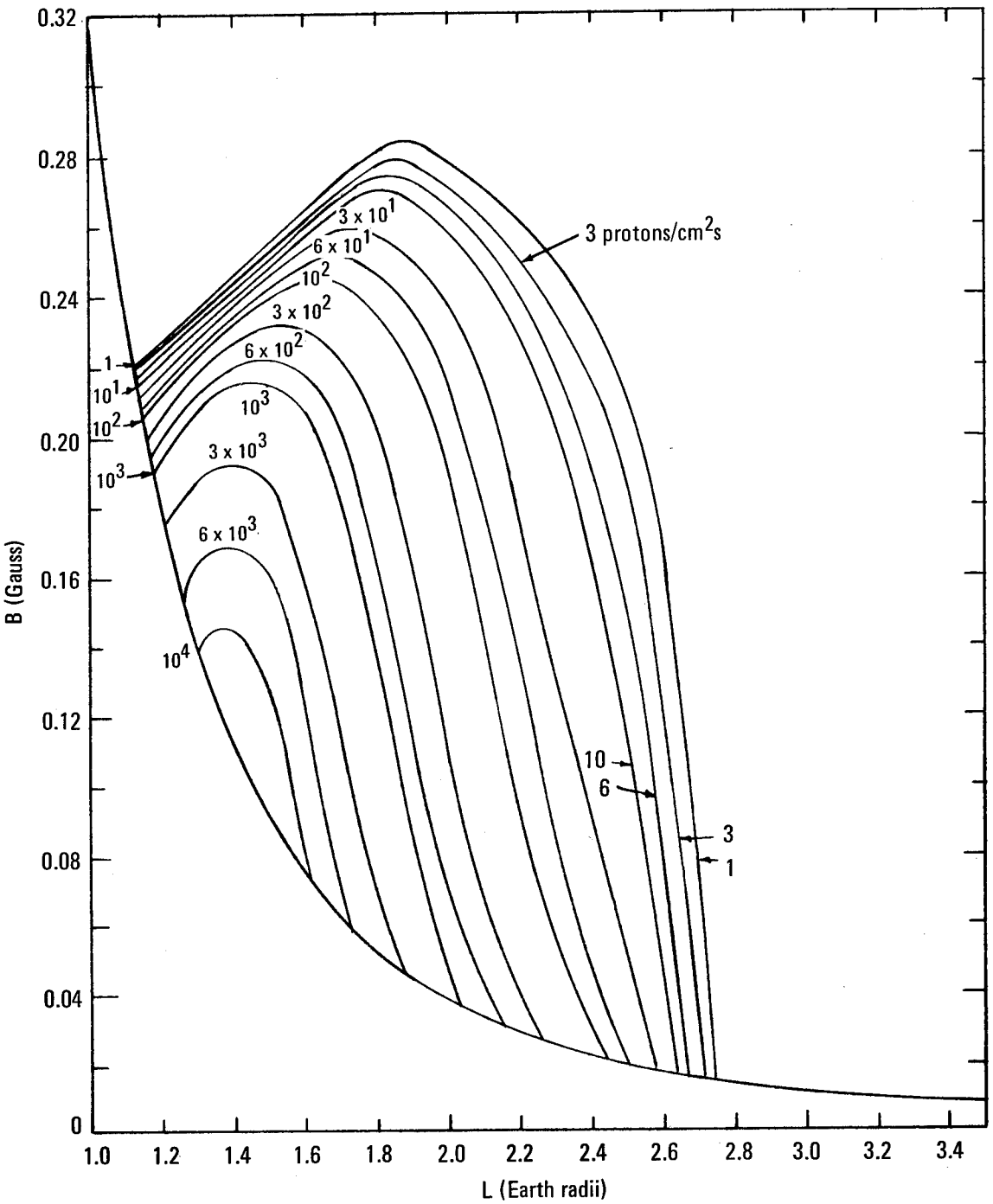

Figure 43.—Model AP7 omnidirectional proton flux as function of B and L ($E > 50$ MeV) (ref. 118).

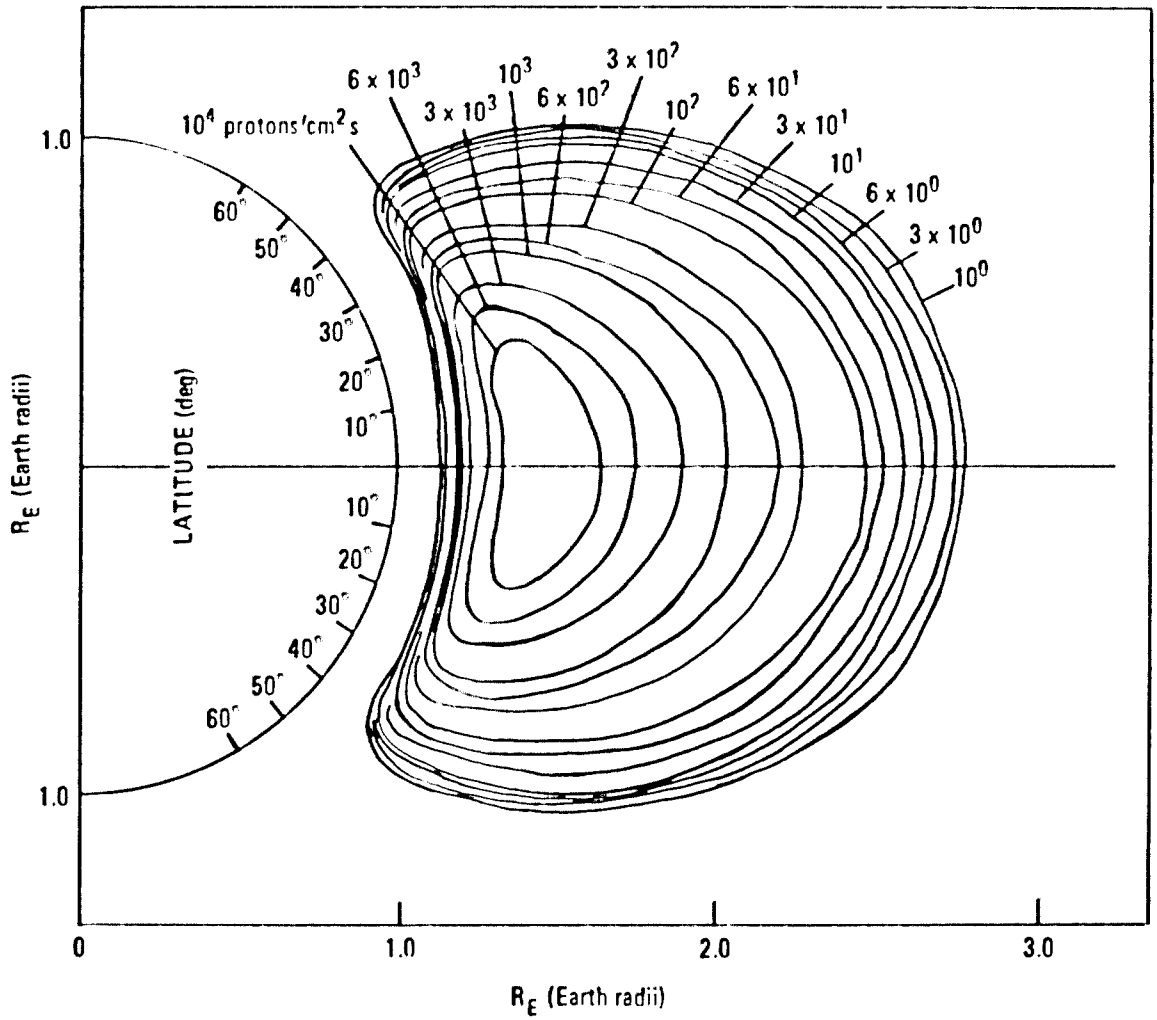

Figure 44.—Model AP7 omnidirectional proton flux as function of R_E and latitude (> 50 MeV) (ref. 118).

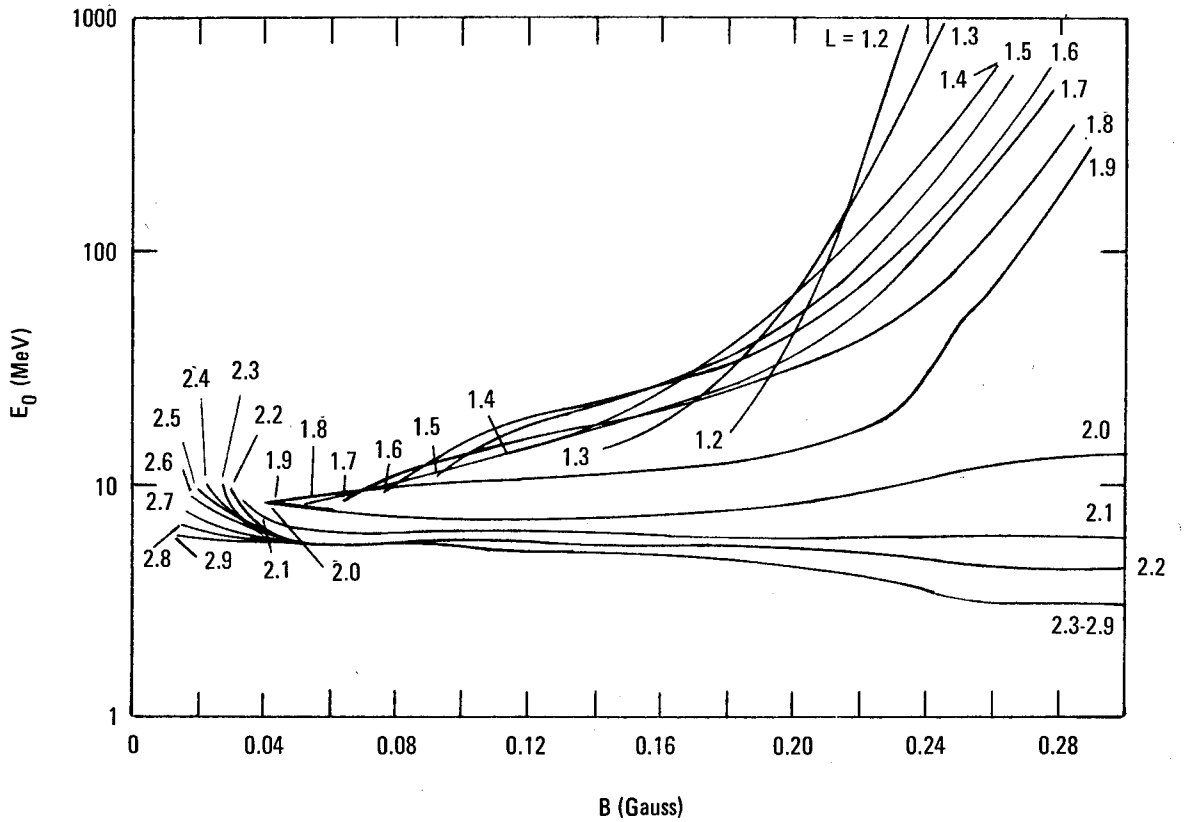

Figure 45.—Spectral parameter E_0 for Model AP1 (ref. 112).

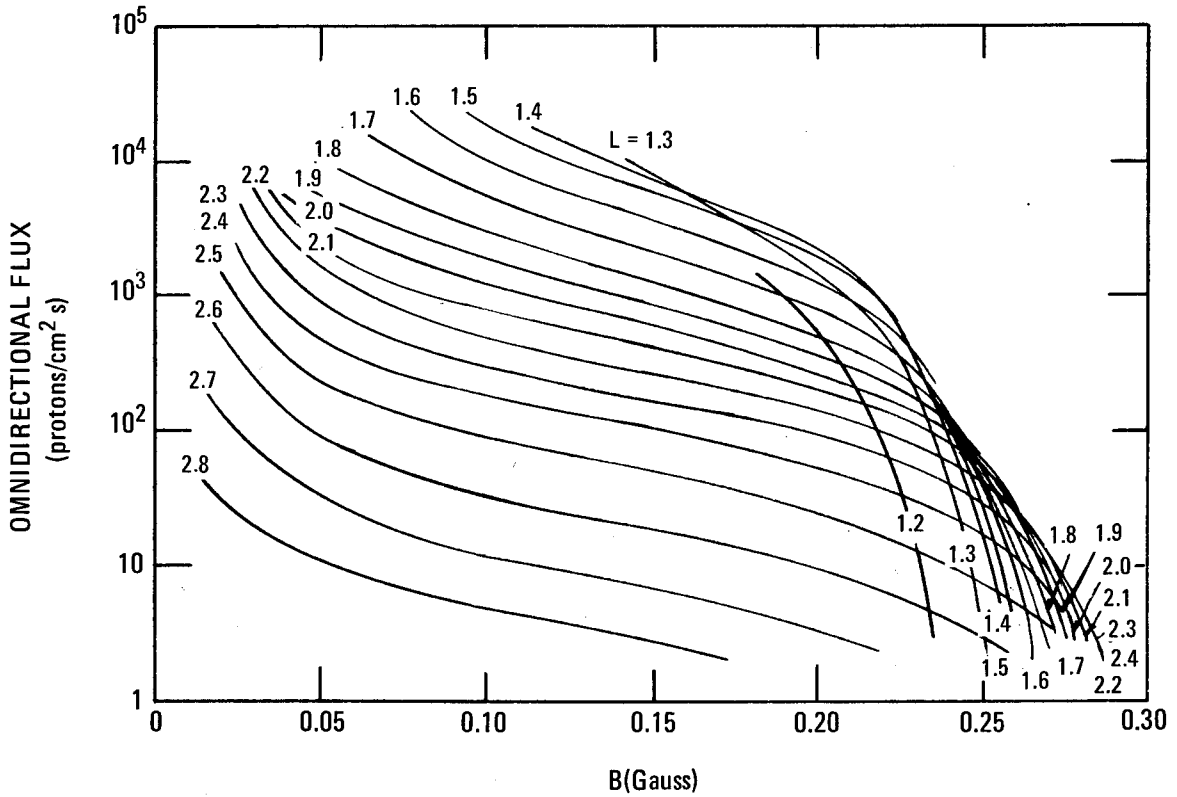

Figure 46.—Omnidirectional flux for Model AP1 (E > 34 MeV) (ref. 112).

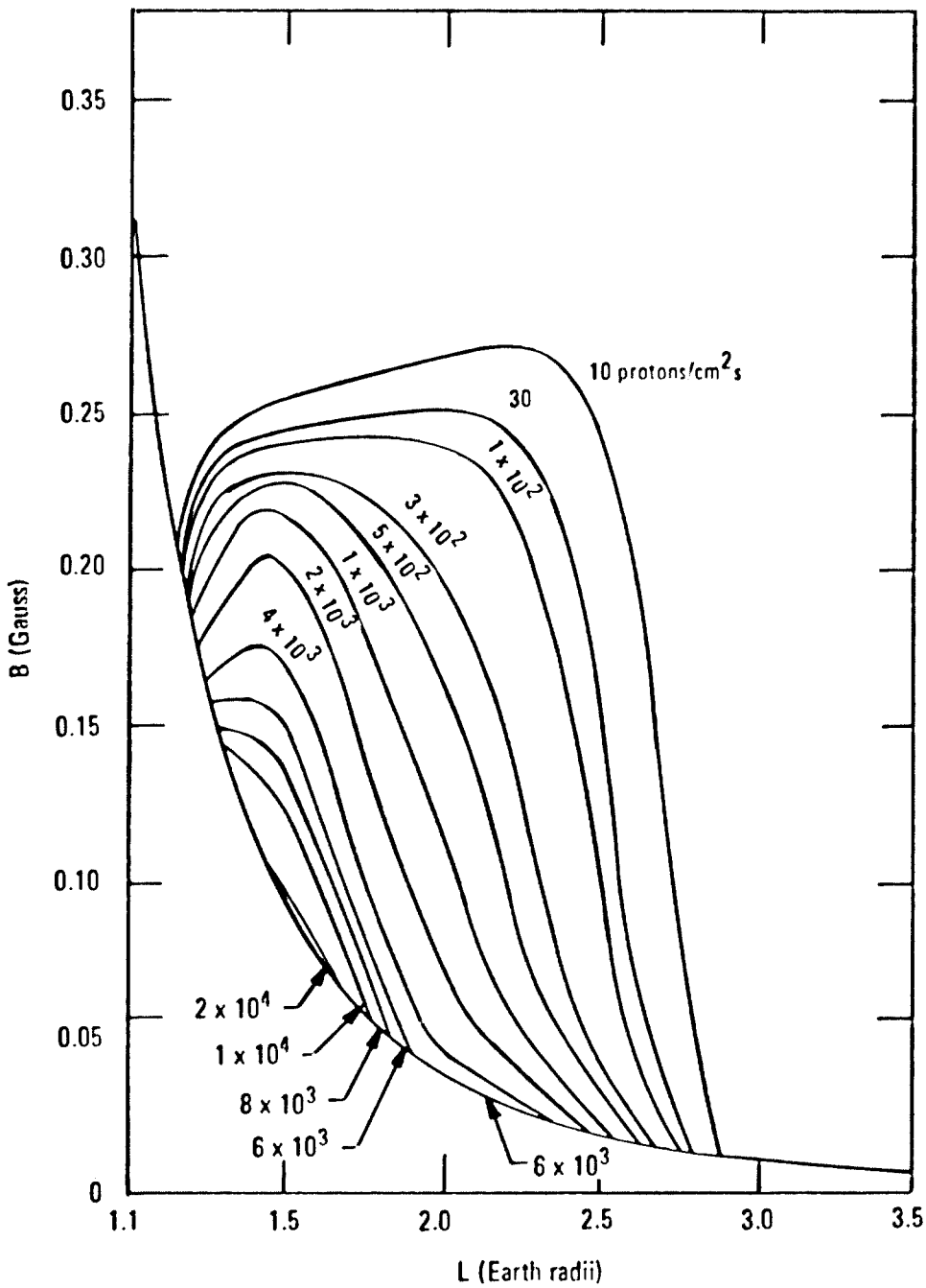

Figure 47.–Model AP1 omnidirectional proton flux (E > 34 MeV) as function of B and L (ref. 112).

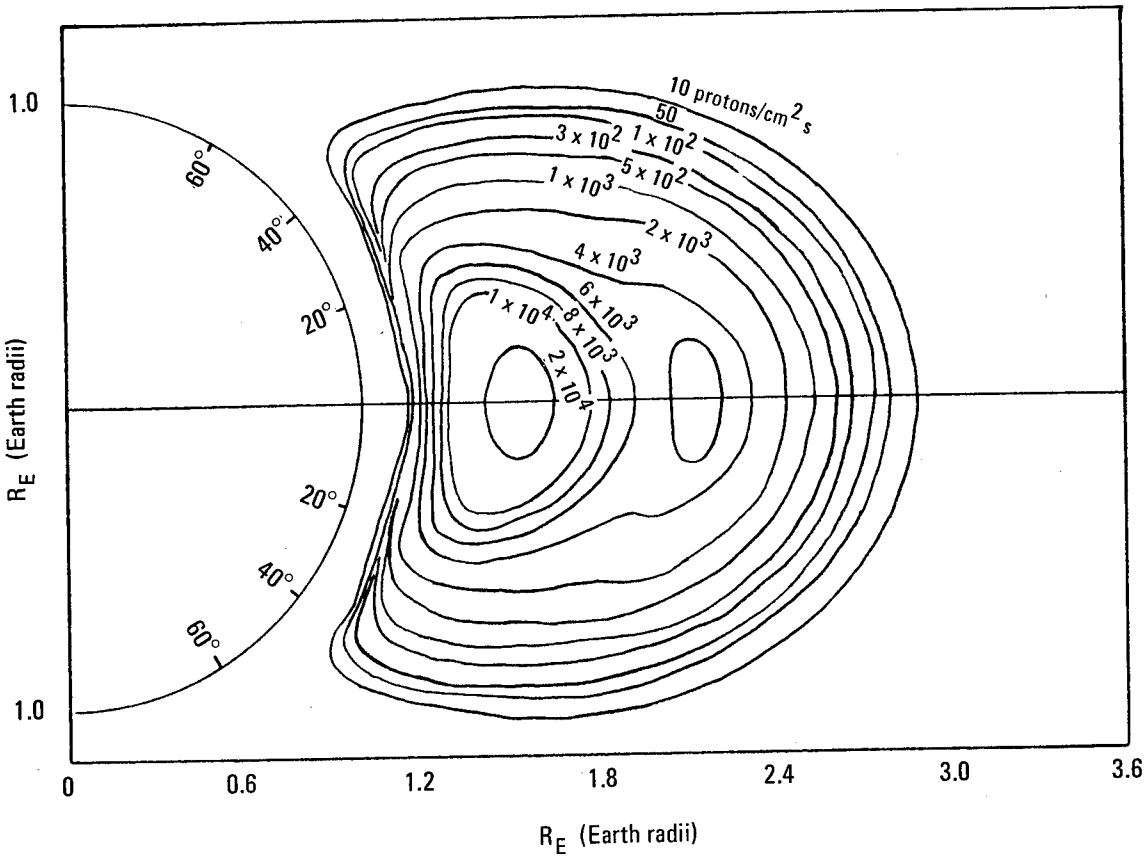

Figure 48.—Model AP1 omnidirectional proton flux (E > 34 MeV) as function of R_E and latitude (ref. 112).

3.2.3 Inner Belt, 4 MeV < E < 30 MeV (Model AP6)

Model AP6 should be used for inner belt protons in the energy range between 4 MeV and 30 MeV.

It was shown that the energy spectrum of the data was best fit by a power law. (An exponential fit was used for Models AP2 and AP4.) The power law parameter P is shown as a function of L in figure 49.

Figures 50, 51, and 52 show the omnidirectional flux for E > 4 MeV and E < 30 MeV. The distribution function is tabulated in table 2 of reference 117.

Time fluctuations were not incorporated because the proton fluxes are relatively stable. The effect of the solar cycle is too uncertain to warrant inclusion. Model AP6 is an average of available data. It is expected that actual fluxes should not differ from these values by more than a factor of two.

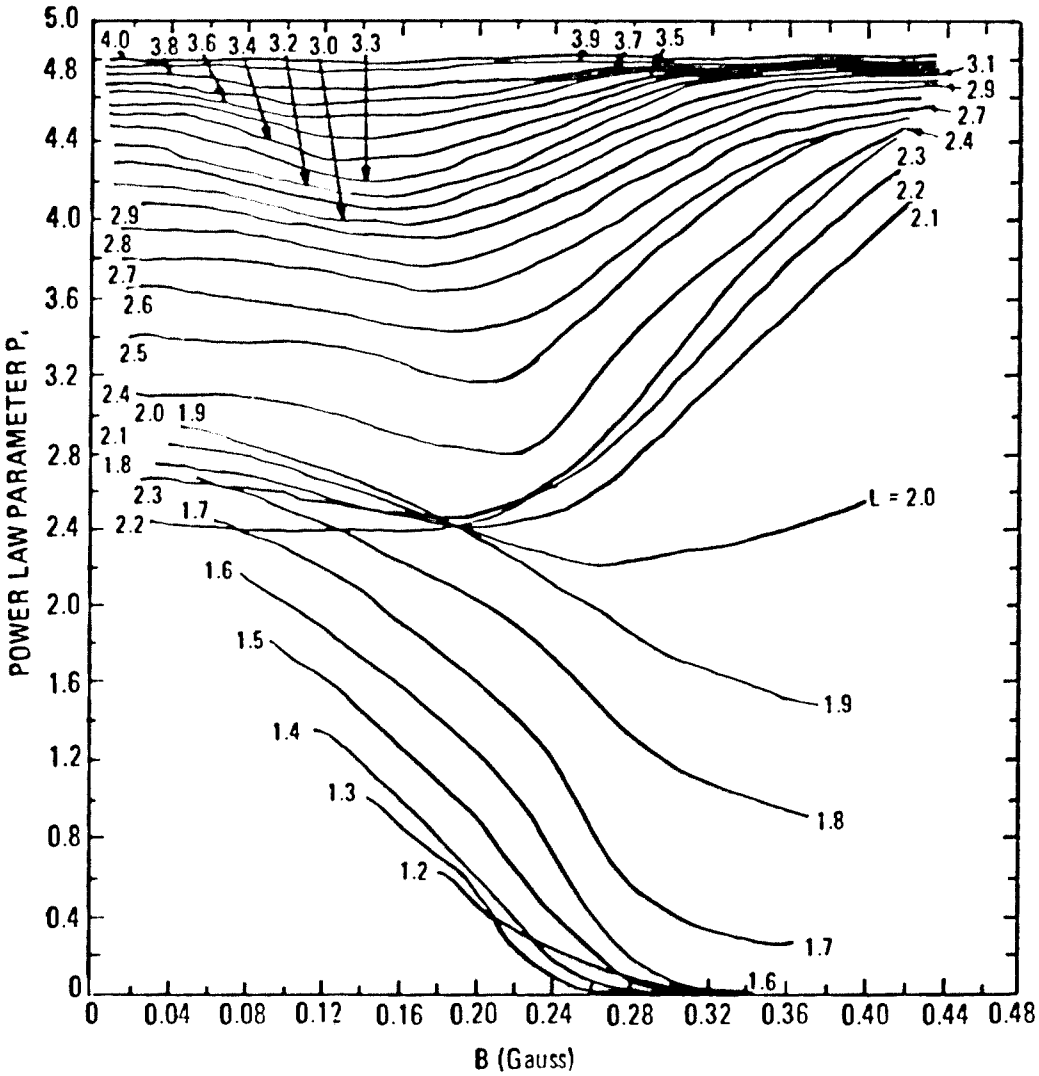

Figure 49.–Spectral parameter P for Model AP6 (ref. 117).

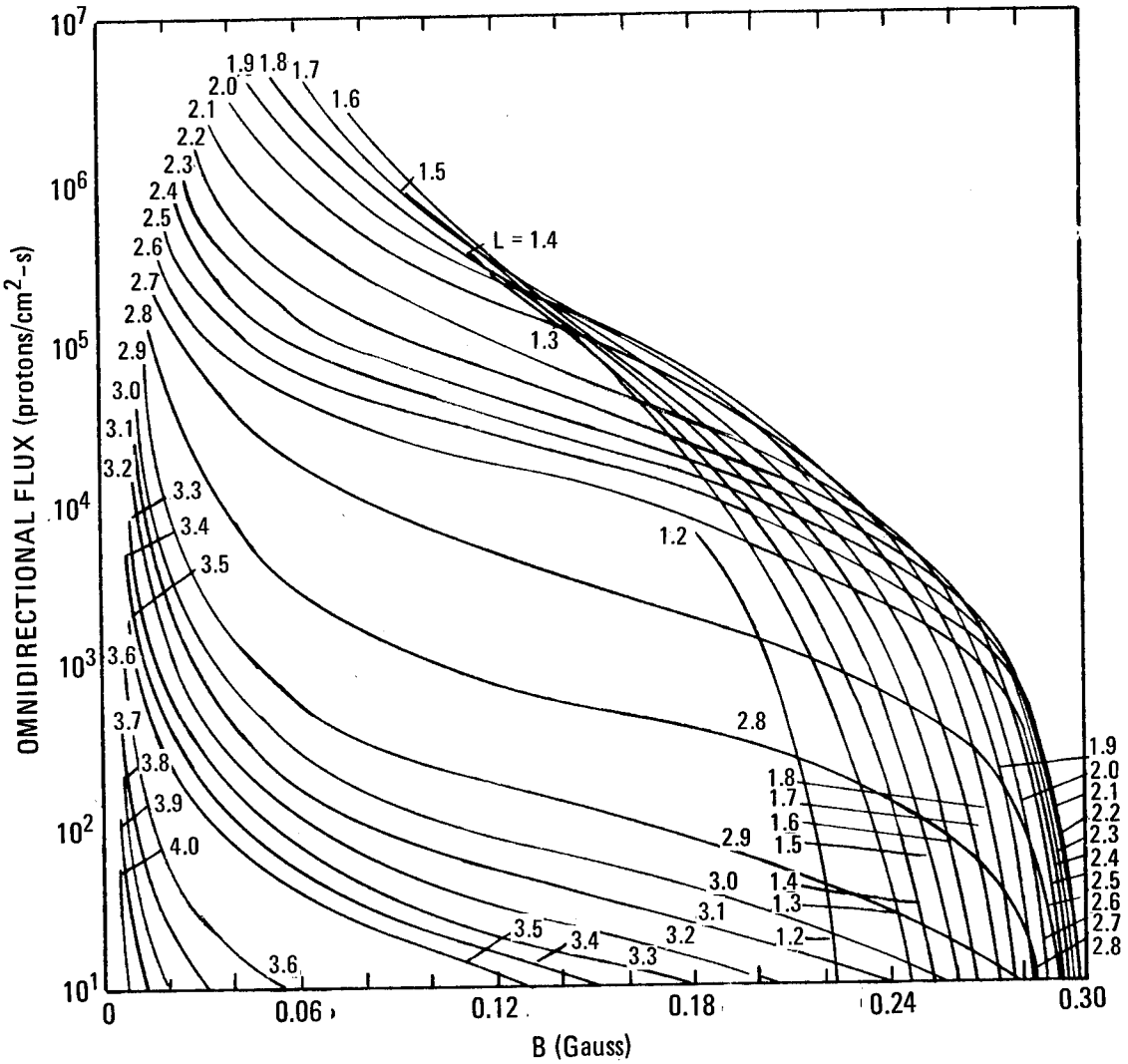

Figure 50.—Omnidirectional flux for Model AP6 (E > 4 MeV) (ref. 117).

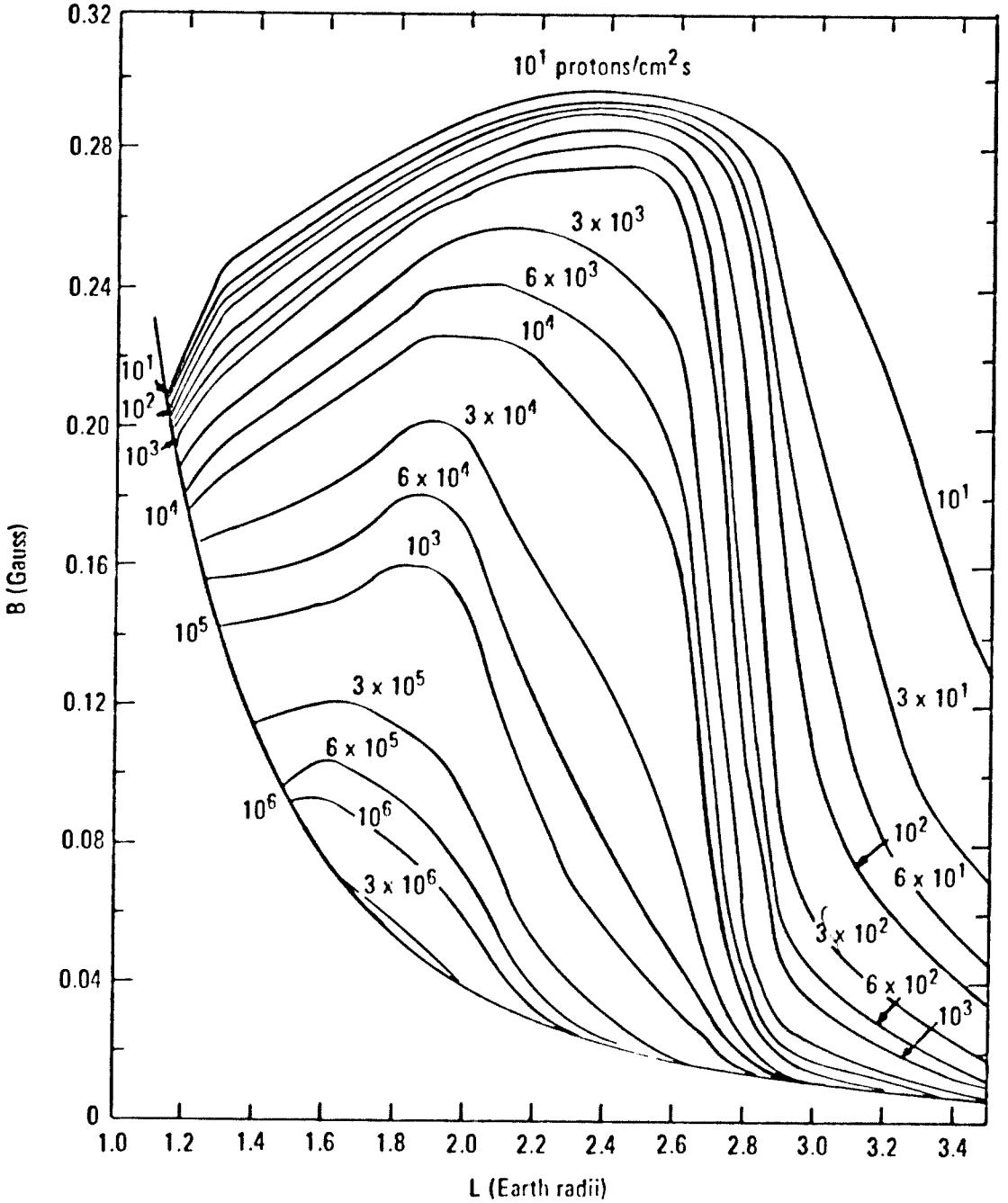

Figure 51.–Model AP6 omnidirectional proton flux ($E > 4$ MeV) as function of B and L (ref. 117).

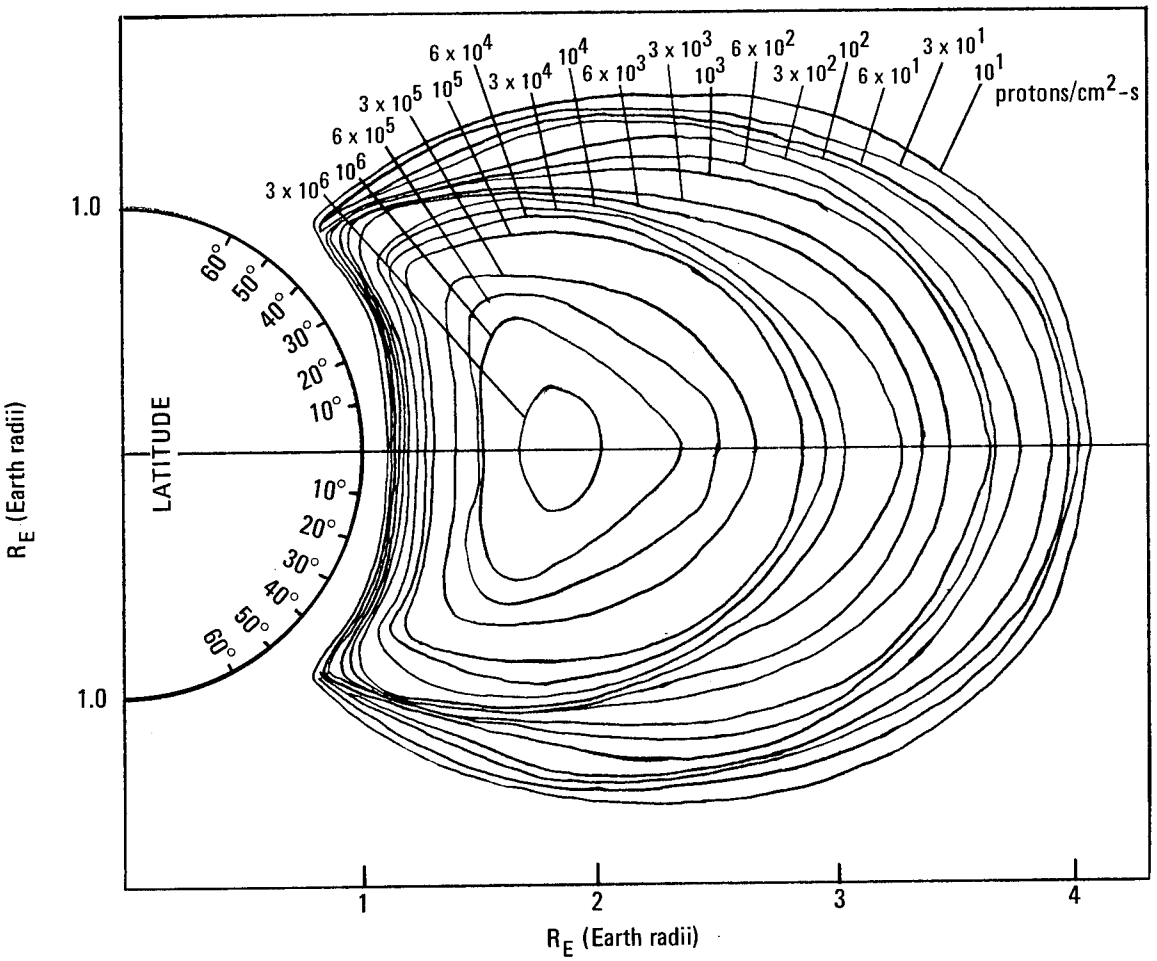

Figure 52.—Model AP6 omnidirectional proton flux ($E > 4$ MeV) as function of R_E and latitude (ref. 117).

3.2.4 Inner And Outer Belts, E < 4 MeV (Model AP5)

The proton environment between $L = 1.2$ and 6.6 for energy levels below 4 MeV is described by Model AP5. Spacecraft data up to April 1965 were used. Date coverage was best in the range between $L = 2.4$ and 4.0.

Both an exponential and a power law fit to the energy spectrum was found satisfactory; the exponential form was selected. The lower energy limit was found to vary with L. The recommended lower energy limit as a function of L is shown in figure 53. The exponential parameter E_0 is shown in figure 54 which shows that the spectrum shifts to lower energies with increasing L and generally does the same with increasing B. The omnidirectional proton flux is shown in figures 55 and 56 for $E > 0.4$ MeV. Tabulated values are given in table 2 of reference 116.

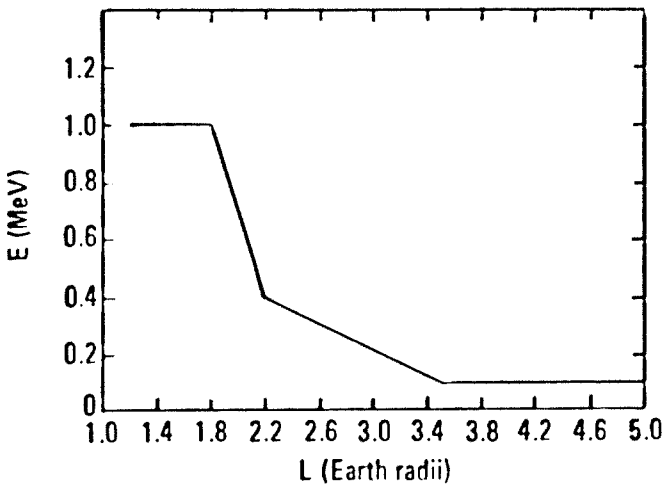

Figure 53.– Recommended low energy limit for Model AP5 (ref. 116).

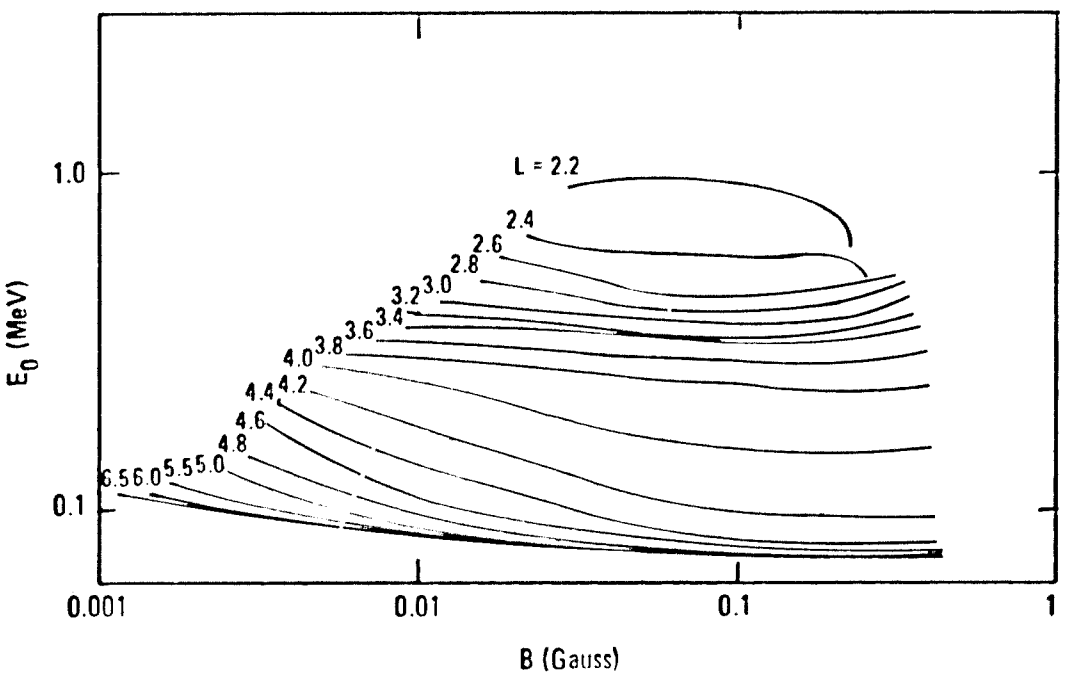

Figure 54.–Spectral parameter E_0 for Model AP5 ($L \leq 2.0$) (ref. 116).

Temporal variations were found to cause changes in the observed flux by as much as a factor of two. The variations are not taken into account so the accuracy of the model is subject to this limitation. In addition, for L greater than 5.0, magnetospheric distortion causes inaccuracies.

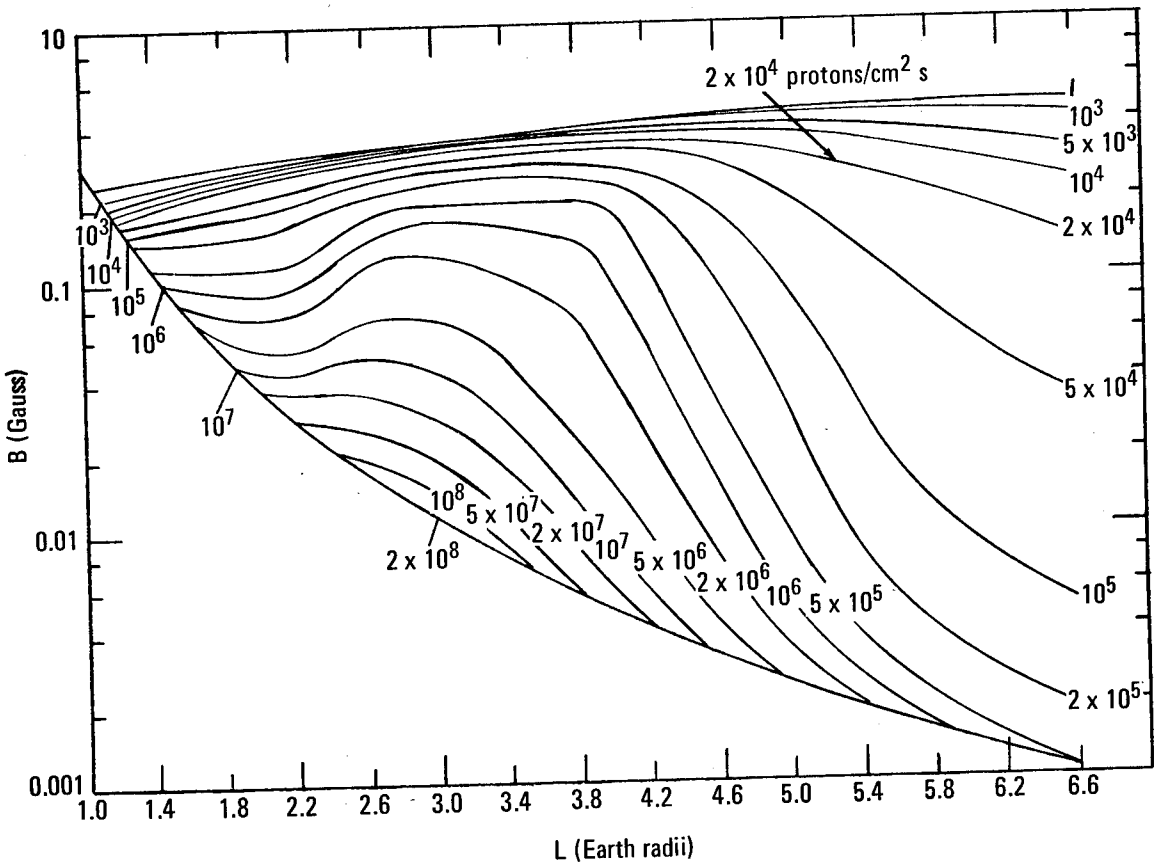

Figure 55.—Model AP5 omnidirectional proton flux ($E > 0.4$ MeV) as function of B and L (ref. 116).

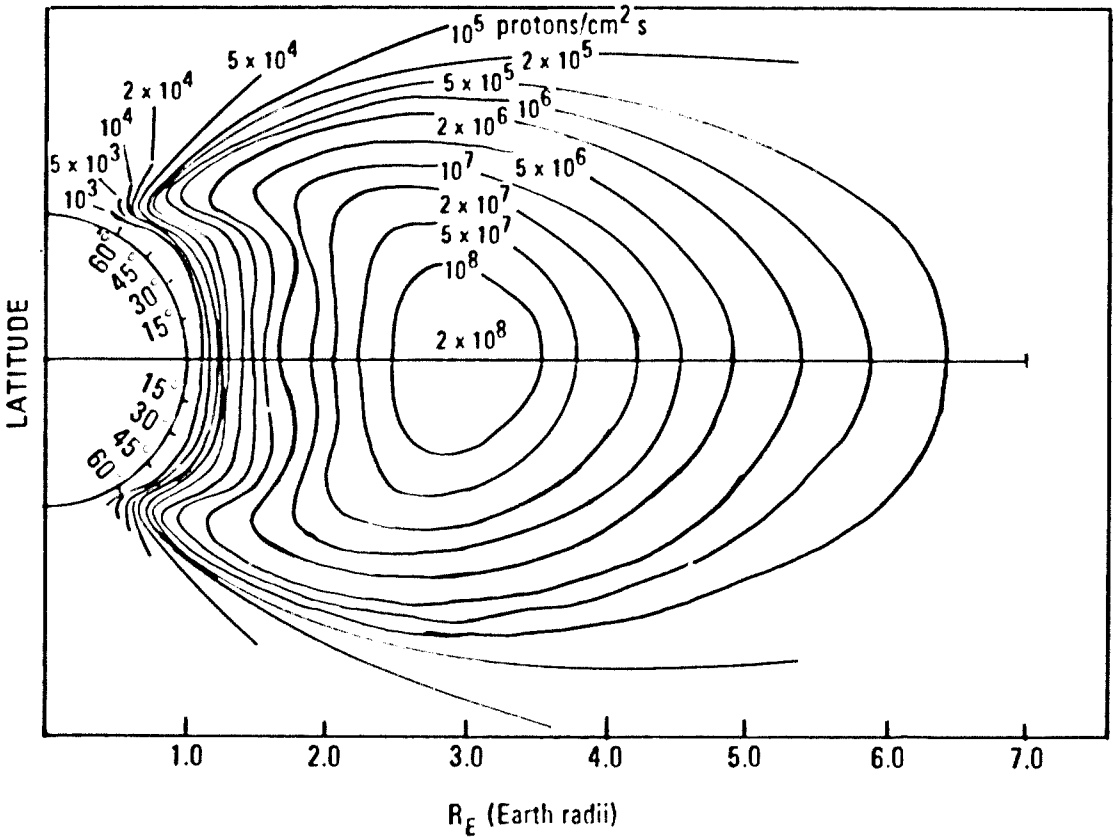

Figure 56.—Model AP5 omnidirectional proton flux ($E > 0.4$ MeV) as function of R_E and latitude (ref. 116).

3.2.5 Smoothed Proton Model

Combination of proton models AP1, AP5, AP6, and AP7 results in a discontinuous model at the boundaries of the individual model energy ranges. A smoothed model of the trapped proton environment on the basis of models AP5, AP6, and AP7 is presented in reference 121 and is shown in figure 57. An improved version of smoothed proton model interfaces that takes into account all available proton models is available from the National Space Science Data Center of the NASA Goddard Space Flight Center (ref. 115).

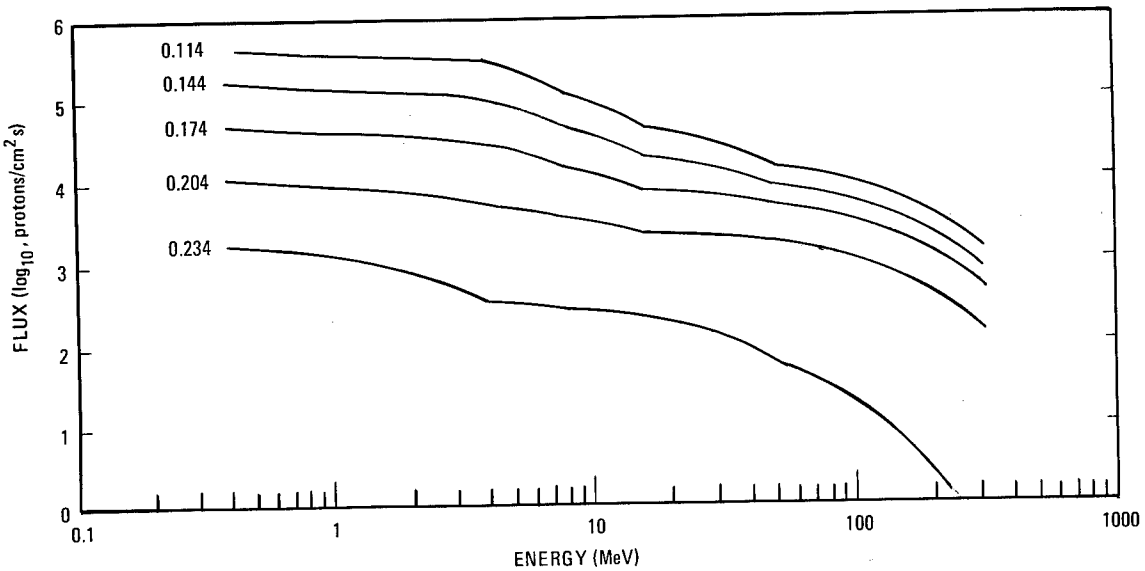

a. 0.114 to 0.234 Gauss

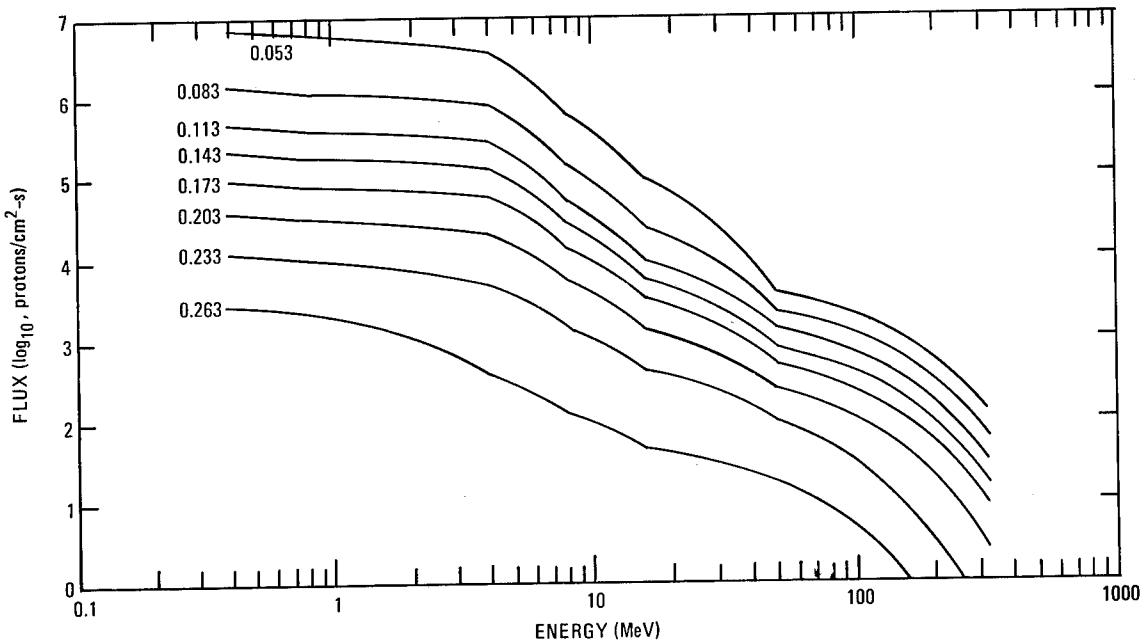

b. 0.053 to 0.263 Gauss

Figure 57.—Energy integrated omnidirectional proton flux from reference 121 (cont.).

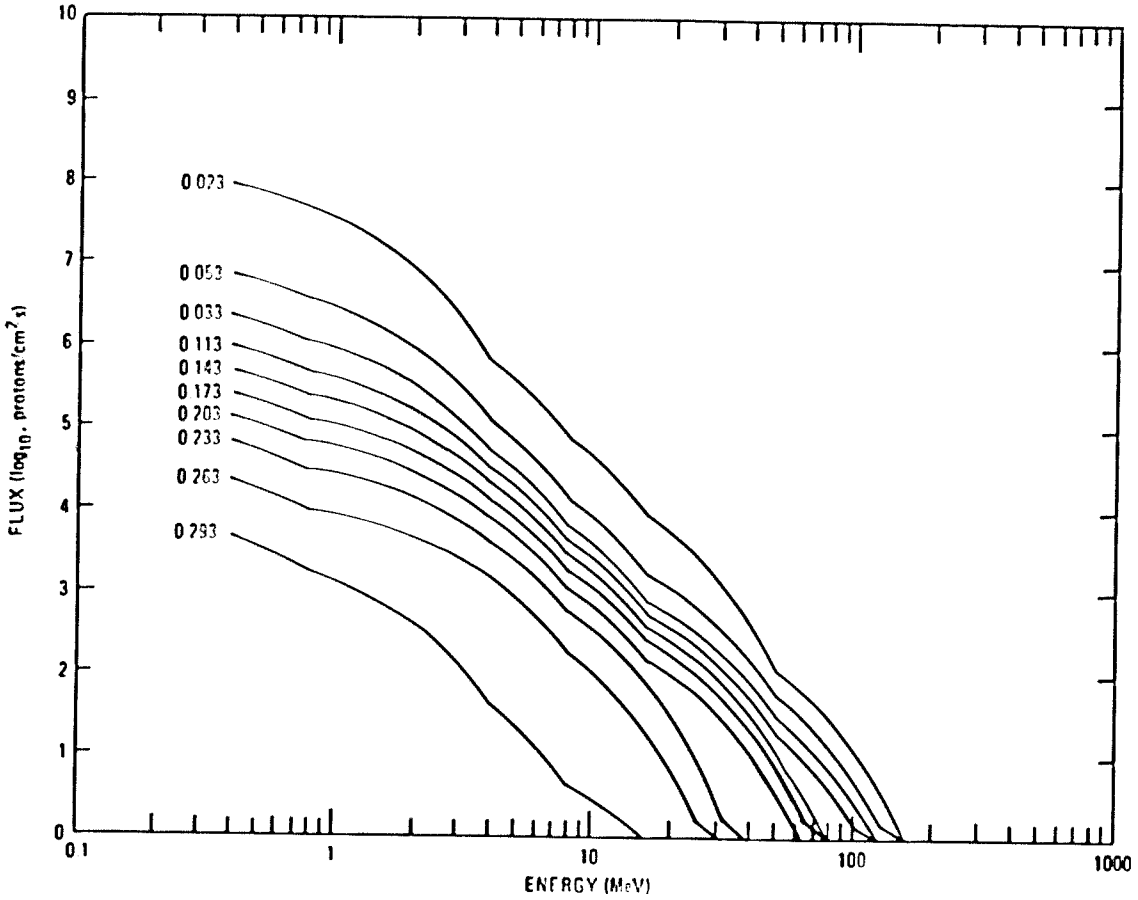

c. 0.023 to 0.293 Gauss

Figure 57.–Energy integrated omnidirectional proton flux (ref. 121).

REFERENCES

1. King, J. H.: Solar Proton Fluences for 1977-1983. Space Mission, J. of Spacecraft and Rockets, II, pp. 401-408, June 1974.

2. Anon.: Nuclear and Space Radiation Effects on Materials. NASA Space Vehicle Design Criteria (Structures), NASA SP-8053, June 1970.

3. Anon.: Magnetic Fields–Earth and Extraterrestrial. NASA Space Vehicle Design Criteria (Environment), NASA SP-8017, March 1969.

4. Van Allen, J. A.; et al.: Observation of High Intensity Radiation by Satellites 1958 Alpha and Gamma. Jet Propulsion, 1958, p. 588.

5. Van Allen, J. A.: The First Public Lecture on the Discovery of the Geomagnetically Trapped Radiation. State University of Iowa, Report 60-13, 1960.

6. Singley, G. W. and Vette, J. I.: The AE-4 Model of the Outer Radiation Zone Electron Environment. NASA GSFC National Space Science Data Center, NSSDC 72-06, August 1972.

7. Teague, M. J. and Vette, J. I.: The Inner Zone Electron Model AE-5. NASA GSFC National Space Science Data Center, NSSDC 72-10, November 1972.

8. Hess, W. N.: The Radiation Belt and Magnetosphere. Blaisdell Publishing Company (Waltham, Mass.), 1968.

9. Cladis, J. B.; Davidson, G. T.; and Newkirk, L. L. (editors): The Trapped Radiation Handbook. Defense Nuclear Agency, DNA 2524H, December 1971.

10. McCormac, B. M., ed.: Particles and Fields in the Magnetosphere. Springer-Verlog New York Inc., New York, D. Reidel Publishing Co., Dordrecht-Holland, 1970.

11. McCormac, B. M., ed.: Earth's Magnetospheric Processes. D. Reidel Publishing Co., Dordrecht-Holland, 1972.

12. Spreiter, J. R. and Alksne, A. Y.: Plasma Flow Around the Magnetosphere. Reviews of Geophysics, Vol. 7, Nos. 1, 2, February-May 1969, pp. 11-50.

13. Roederer, J. G.: Quantitative Models of the Magnetosphere. Reviews of Geophysics, Vol. 7, Nos. 1, 2, February-May 1969, pp. 77-96.

14. Frank, L. A.: Plasma in the Earth's Polar Magnetosphere. Journal of Geophysical Research, Vol. 76, No. 22, August 1, 1971, pp. 5202-5219.

15. Ness, N. F.: The Geomagnetic Tail. Reviews of Geophysics, Vol. 7, Nos. 1, 2, February-May 1969, pp. 97-128.

16. Vette, J. I.: Trapped Radiation Population. Section 4 of Trapped Radiation Handbook, Defense Nuclear Agency, DNA 2524H, December 1971.

17. Vette, J. I.: Summary of Particle Populations in the Magnetosphere. In Particles and Fields in the Magnetosphere, D. Reidel Publishing Co., Dordrecht-Holland, 1970, pp. 305-318.

18. Winckler, J. R.: The Origin and Distribution of Energetic Electrons in the Van Allen Radiation Belts. Particles and Fields in the Magnetosphere, B. M. McCormac, ed., D. Reidel Publishing Co., Dordrecht-Holland, 1970, pp. 332-352.

19. Anderson, K. A. and Ness, N. F.: Correlation of Magnetic Fields and Energetic Electrons on the IMP-1 Satellite. Journal of Geophysical Research, Vol. 71, No. 15, August 1966, pp. 3705-3727.

20. Gringauz, K. I.: Low-Energy Plasma in the Earth's Magnetosphere. Reviews of Geophysics, Vol. 7, Nos. 1, 2, February-May 1969, pp. 339-378.

21. Chappell, C. R.: Recent Satellite Measurements of the Morphology and Dynamics of the Plasmasphere. Review of Geophysics and Space Physics, Vol. 10, No. 4, November 1972, pp. 951-979.

22. Heikkila, W. J. and Winningham, J. D.: Penetration of Magnetosheath Plasma to Low Altitudes through the Dayside Magnetospheric Cusps. Journal of Geophysical Research, Vol. 76, No. 4, February 1, 1971, pp. 883-891.

23. Kivelson, M. G.: et al.: Dependence of the Polar Cusp on the North-South Component of the Interplanetary Magnetic Field. Journal of Geophysical Research, Vol. 78, No. 19, July 1, 1973, pp. 3761-3772.

24. Lanzerotti, L. J.: Solar Energetic Particles and the Configuration of the Magnetosphere. Review of Geophysics and Space Physics, Vol. 10, No. 1, February 1972, pp. 379-393.

25. West, H. I., Jr. and Vampola, A. L.: Simultaneous Observations of Solar Flare Electron Spectra in Interplanetary Space and Within the Earth's Magnetosphere. Physical Review Letters, Vol. 26, 1971, p. 458.

26. Axford, W. I.: Magnetospheric Convection. Reviews of Geophysics, Vol. 7, Nos. 1, 2, February-May 1969.

27. Hultqvist, B.: Auroras and Polar Substorms: Observations and Theory. Reviews of Geophysics, Vol. 7, Nos. 1, 2, February-May 1969, pp. 129-178.

28. Brice, N. and Lucas, C.: Influence of Magnetospheric Convection and Polar Wind on Loss of Electrons from the Outer Radiation Belt. Journal of Geophysical Research, Vol. 76, No. 4, February 1, 1971, pp. 900-908.

29. Frank, L. A. and Ackerson, K. L.: Observations of Charged Particle Precipitation into the Auroral Zone. Journal of Geophysical Research, Vol. 76, No. 16, June 1, 1971, pp. 3612-3643.

30. Cornwall, J. M.; Coroniti, F. V.; and Thorne, R. M.: Turbulent Loss of Ring Current Protons. Journal of Geophysical Research, Space Physics, Vol. 75, No. 25, September 1, 1970, pp. 4699-4709.

31. Murayama, T.: Spatial Distribution of Energetic Electrons in the Geomagnetic Tail. Journal of Geophysical Research, Vol. 71, 1966, pp. 5547-5558.

32. Yoshida, S.; Ludwig, G. H.; and Van Allen, J. A.: Distribution of Trapped Radiation in the Geomagnetic Field. Journal of Geophysical Research, Vol. 65, 1960.

33. Van Allen, J. A.; McIlwain, C. E.; and Ludwig, G. H.: Radiation Observations with Satellite 1958 E. Journal of Geophysical Research, Vol. 64, 1959.

34. Vernov, S. N. and Chudakov, A. E.: Terrestrial Corpuscular Radiation and Cosmic Rays. Space Research, Vol. 1, 1960.

35. Freden, S. C. and White, R. S.: Protons in the Earth's Magnetic Field. Physical Review Letters, Vol. 3, 1959.

36. Heckman, H. H.; Lindstrom, P. J.; and Nakano, G. H.: Long-Term Behavior of Energetic Inner-Belt Protons. In Models of the Trapped Radiation Environment, Vol. VII: Long Term Time Variations, NASA SP-3024, 1971, pp. 37-47.

37. White, R. S.: High Energy Proton Radiation Belt. Reviews of Geophysics and Space Physics, Vol. 11, No. 3, August 1973, pp. 595-632.

38. Pizzella, G.; McIlwain, C. E.; and Van Allen, J. A.: Time Variations of Intensity in the Earth's Inner Radiation Zone October 1959 through December 1960. Journal of Geophysical Research, Vol. 67, 1962.

39. Bostrom, C. O.; Beall, D. S.; and Armstrong, J. C.: Time History of the Inner Radiation Zone, October 1963 to December 1968. Journal of Geophysical Research, Space Physics, Vol. 75, No. 7, March 1, 1970, pp. 1246-1256.

40. Naugle, J. E. and Kniffen, D. A.: The Flux and Energy Spectrum of the Protons in the Inner Van Allen Belt. Physical Review Letters, Vol. 7, 1961.

41. McIlwain, C. E.: Coordinates for Mapping the Distribution of Magnetically Trapped Particles. Journal of Geophysical Research, Vol. 66, 1961.

42. Walt, M.: History of Artificial Radiation Belts. Section 6 of Trapped Radiation Handbook, Defense Nuclear Agency, DNA 2524H, December 1971.

43. Teague, M. J. and Stassinopoulos, E. G.: A Model of the Starfish Flux in the Inner Radiation Zone. NASA, Goddard Space Flight Center, X-601-72-487, December 1972.

44. Galperin, Yu. I. and Bulyunova, A. D.: Study of the Drastic Changes of the Radiation in the Upper Atmosphere in July 1962. USSR National Report to COSPAR, May 1964.

45. Elliot, H.: Some Cosmic Ray and Radiation Belt Observations Based on Data from the Anton 302 G-M Counter in Ariel I. In Radiation Trapped in the Earth's Magnetic Field (B. M. McCormac, ed.), D. Reidel Publishing Co., (Dordrecht), 1966, pp. 76-100.

46. West, H. I., Jr.; Mann, L. G.; and Bloom, S. D.: University of California Report UCRL-7659, TID-4500, (29th Ed.), 1964.

47. Brown, W. L.: Results of the Telstar Radiation Experiments. Bell System Technology Journal, July 1963.

48. Hess, W. N.: The Artificial Radiation Belt made on July 9, 1962. Journal of Geophysical Research, Vol. 68, 1963.

49. Imhof, W. L.; Gaines, E. E.; and Reagan, J. B.: Dynamic Variations in Intensity and Energy Spectra of Electrons in the Inner Radiation Belt. Journal of Geophysical Research, Vol. 78, No. 22, August 1, 1973, pp. 4568-4577.

50. Pizzella, G., and Frank, L. A.: Energy Spectrums for Proton (200 ev $\lesssim$ E $\lesssim$ 1 MeV) Intensities in the Outer Radiation Zone. Journal of Geophysical Research, Vol. 76, No. 1, January 1, 1971, pp. 88-91.

51. Williams, D. J.: Trapped Protons $\geq$ 100 keV and Possible Sources. In Particles and Fields in the Magnetosphere. D. Reidel Publishing Company, Dordrecht-Holland, 1970, pp. 396-409.

52. McIlwain, C. E.: Ring Current Effects on Trapped Particles. Journal of Geophysical Research, Vol. 71, 1966.

53. Paulikas, G. A. and Blake, J. B.: The Particle Environment at the Synchronous Altitude. In Models of the Trapped Radiation Environment, Vol. VII: Long Term Time Variations, NASA SP-3024, 1971, pp. 49-67.

54. Frank, L. A.; Van Allen, J. A.; and Hills, H. K.: A Study of Charged Particles in the Earth's Outer Radiation Zone with Explorer XIV. Journal of Geophysical Research, Vol. 69, 1964.

55. Mihalov, J. D.: Electron Injection Observed in the Outer Radiation Zone. Transactions of the American Geophysical Union, Vol. 49, Dec. 1968, p. 719.

56. Freeman, J. W., Jr.: The Morphology of the Electron Distribution in the Outer Radiation Zone and Near the Magnetospheric Boundary as Observed by Explorer XII. Journal of Geophysical Research, Vol. 69, 1964.

57. Williams, D. J. and Smith, A. M.: Daytime Trapped Electron Intensities at High Latitudes at 1100 Kilometers. Journal of Geophysical Research, Vol. 70, 1965.

58. Williams, D. J.: A 27-day Periodicity in Outer Zone Trapped Electron Intensities. Journal of Geophysical Research, Vol. 71, 1966.

59. O'Brien, B. J.: A Large Diurnal Variation of the Geomagnetically Trapped Radiation. Journal of Geophysical Research, Vol. 68, 1963.

60. Frank, L. A.; Van Allen, J. A.; and Macagno, E.: Charged-Particle Observations in the Earth's Outer Magnetosphere. Journal of Geophysical Research, Vol. 68, 1963.

61. Krimigis, S. M. and Van Allen, J. A.: Geomagnetically Trapped Alpha Particles. Journal of Geophysical Research, Vol. 72, 1967, pp. 5779-5797.

62. Blake, J. B. and Paulikas, G. A.: Measurements of Trapped α -Particles. In Particles and Fields in the Magnetosphere, D. Reidel Publishing Co., Dordrecht, Holland, 1970, pp. 381-386.

63. Krimigis, S. M.: Alpha Particles Trapped in the Earth's Magnetic Field in Particles and Fields in the Magnetosphere, D. Reidel Publishing Co., Dordrecht, Holland, 1970, pp. 364-379.

64. Scholar, M.; Hovestadt, D.; and Hausler, B.: Change of Solar Flare Proton to Alpha Ratios During an Energetic Storm Particle Event. Solar Physics, Vol. 24, 1972, pp. 475-482.

65. Paulikas, G. A.; Blake, J. B.; and Vampola, A. L.: Solar Particle Observations over the Polar Caps. In Particles and Fields in the Magnetosphere, D. Reidel Publishing Co., Dordrecht, Holland, 1970, pp. 141-147.

66. Anderson, K. A.: Entry of Solar Cosmic Rays into the Earth's Magnetosphere. In Particles and Fields in the Magnetosphere. D. Reidel Publishing Co., Dordrecht, Holland, 1970, pp. 3-17.

67. Fanselow, J. L. and Stone, E. C.: Geomagnetic Cutoffs for Cosmic-Ray Protons for Seven Energy Intervals between 1.2 and 39 MeV. Journal of Geophysical Research, Vol. 77, No. 22, August 1, 1972, pp. 3999-4009.

68. Teegarden, B. J.; Von Rosenvinge, T. T.; and McDonald, F. B.: Satellite Measurements of the Charge Composition of Solar Cosmic Rays in the $6 \leq Z \leq 26$ Interval. The Astrophysical Journal, Vol. 180, March 1, 1973, pp. 571-581.

69. Lingenfelter, R. E.; et al.: High-Energy Solar Neutrons, Parts I and II. Journal of Geophysical Research, Vol. 70, 1965.

70. Neugebauer, M. and Snyder, C. W.: Mariner 2 Observations of the Solar Wind: 1. Average Properties. Journal of Geophysical Research, Vol. 71, 1966.

71. Coon, J. H.: Vela Satellite Measurements of Radiation Trapped in Earth's Magnetic Field. D. Reidel (Holland), 1966.

72. Dragt, A. J.; Austin, M. M.; and White, R. S.: Cosmic Ray and Solar Proton Albedo Neutron Decay Injection. Journal of Geophysical Research, Vol. 71, 1966.

73. Hess, W. N. and Killeen, J.: Spatial Distribution of Protons from Neutron Decay Trapped by the Geomagnetic Field. Journal of Geophysical Research, Vol. 71, 1966.

74. Preszler, A. M.; Simnett, G. M.; and White, R. S.: Albedo Neutrons from 10 to 100 MeV. Physical Review Letters, 28, 15, April 10, 1972, pp. 982-984.

75. Lenchek, A. M.: On the Anomalous Component of Low-Energy Geomagnetically Trapped Protons. Journal of Geophysical Research, Vol. 67, 1962.

76. Axford, W. I.: On the Origin of Radiation Belt and Auroral Primary Ions. In Particles and Fields in the Magnetosphere. D. Reidel Publishing Co., Dordrecht, Holland, 1970, pp. 46-59.

77. Nakada, M. P. and Mead, G. D.: Diffusion of Protons in the Outer Radiation Belt. Journal of Geophysical Research, Vol. 70, 1965, pp. 4777-4791.

78. Walt, M.: Radial Diffusion of Trapped Particles and Some of Its Consequences. Reviews of Geophysics and Space Physics, Vol. 9, No. 1, February 1971, pp. 11-25.

79. Pai, G. L. and Sarabhai, V. A.: Periodic Fluctuations in the Geomagnetic Field During Magnetic Storms. Planetary and Space Sciences, Vol. 12, 1964, pp. 855-865.

80. Nishida, A.: Geomagnetic DP2 Fluctuations and Associated Magnetospheric Phenomena. Journal of Geophysical Research, Vol. 73, 1968, pp. 1795-1803.

81. Kennel, C. F.: Consequences of a Magnetospheric Plasma. Reviews of Geophysics, Vol. 7, Nos. 1, 2, February-May 1969, pp. 379-420.

82. Parker, E. N.: Geomagnetic Fluctuations and the Form of the Outer Zone of the Van Allen Radiation Belt. Journal of Geophysical Research, Vol. 65, 1960.

83. Tverskoy, B. A.: Main Mechanisms in the Formation of the Earth's Radiation Belts. Reviews of Geophysics, Vol. 7, Nos. 1, 2, February-May 1969, pp. 219-232.

84. Falthammer, C.-G.: Effects of Time-Dependent Electric Fields on Geomagnetically Trapped Radiation. Journal of Geophysical Research, Vol. 70, 1965, pp. 2503-2516.

85. Falthammer, C.-G.: Introductory Survey of Radiation Belt Diffusion. In Particles and Fields in the Magnetosphere. D. Reidel Publishing Co., Dordrecht, Holland, 1970, pp. 387-395.

86. Birmingham, T. J.; Northrop, T. G.; and Falthammer, C.-G.: Charged-Particle Diffusion by Violation of the Third Adiabatic Invariant. Physics of Fluids, Vol. 10, 1967, pp. 2389-2398.

87. Frank, L. A.: Further Comments Concerning Low Energy Charged Particle Distributions within the Earth's Magnetosphere and its Environs. In Particles and Fields in the Magnetosphere, D. Reidel Publishing Co., Dordrecht, Holland, 1970, pp. 319-331.

88. Walt, M.: Panel Report. In Particles and Fields in the Magnetosphere. D. Reidel Publishing Co., Dordrecht, Holland, 1970, pp. 431-441.

89. Farley, T. A.; Tomassian, A. D.; and Walt, M.: Source of High-Energy Protons in the Van Allen Radiation Belt. Physical Review Letters, Vol. 25, No. 1, July 1970, pp. 47-49.

90. Imhof, W. L.; Cladis, J. B.; and Smith, R. V.: Observation of an Energy-Selective Redistribution in the Inner Radiation Belt. Planetary and Space Sciences, Vol. 14, 1966, pp. 569-577.

91. Helliwell, R. A.: Low-Frequency Waves in the Magnetosphere. Reviews of Geophysics, Vol. 7, Nos. 1, 2, February-May 1969, pp. 281-304.

92. Akasofu, S. I.: The Development of the Auroral Substorm. Planetary Space Sciences, Vol. 12, 1964.

93. Van Allen, J. A.: Charged Particles in the Magnetosphere. Reviews of Geophysics, Vol. 7, Nos. 1, 2, February-May 1969, pp. 233-256.

94. Carovillano, R. L. and Siscoe, G. L.: Energy and Momentum Theorems in Magnetospheric Processes. Reviews of Geophysics and Space Physics, Vol. 11, No. 2, May 1973, pp. 289-353.

95. Feldstein, Y. I.: Polar Auroras, Polar Substorms, and Their Relationships with the Dynamics of the Magnetosphere. Reviews of Geophysics, Vol. 7, Nos. 1, 2, February-May 1969, pp. 179-218.

96. Eather, R. H. and Carovillano, R. L.: The Ring Current as the Source Region of Proton Auroras. Cosmic Electrodynamics, Vol. 2, 1971.

97. Roberts, C. S.: Pitch-Angle Diffusion of Electrons in the Magnetosphere. Reviews of Geophysics, Vol. 7, Nos. 1, 2, February-May 1969, pp. 305-338.

98. Roederer, J. G. and Welch, J. A.: Calculations of Longitude Dependence of Geomagnetically Trapped Electron Fluxes. Space Res. VI, Proceedings of the Sixth International Space Science Symposium, (Mar Del Plata, Argentina), May 11-19, 1965, MacMillan and Co., Ltd., London, 1966, pp. 148-164.

99. Dragt, A. G.: Effect of Hydromagnetic Waves on the Lifetime of Van Allen Radiation Protons. Journal of Geophysical Research, Vol. 66, 1961.

100. Spitzer, L.: Physics of Fully Ionized Gases. Interscience, New York, 1956.

101. Paulikas, G. A.: The Patterns and Sources of High-Latitude Particle Precipitation. Reviews of Geophysics and Space Physics, Vol. 9, No. 3, August 1971, pp. 659-701.

102. Eather, R. H.: Auroral Proton Precipitation and Hydrogen Emissions. Reviews of Geophysics, Vol. 5, 1967.

103. Vette, J. I.; Lucero, A. B.; and Wright, J. A.: Models of the Trapped Radiation Environment, Vol. II: Inner and Outer Zone Electrons. NASA SP-3024, Vol. II, 1966.

104. O'Brien, B. J.: High-Latitude Geophysical Studies with Satellite Injun 3, 3. Precipitation of Electrons into the Atmosphere. Journal of Geophysical Research, Vol. 69, 1964.

105. Rittenhouse, J. B. and Singletary, J. B. (editors): Space Materials Handbook: Supplement 1 to the Second Edition: Space Materials Experience. NASA SP-3025, 1966, pp. S-1 to S-84.

106. Anon.: Space Radiation Protection. NASA Space Vehicle Design Criteria (Structures), SP-8054, June 1970.

107. Shelton, R. D. and de Loach, A. C.: Analysis of Radiation Damage to ATM Film. NASA TM X-53666, October 20, 1967.

108. Anon.: Spacecraft Solar Arrays. NASA Space Vehicle Design Criteria (Guidance and Control), SP-8074, May 1971.

109. Rittenhouse, J. B. and Singletary, J. B. (editors): Space Materials Handbook, Third Edition. Air Force Materials Laboratory, AFML-TR-68-205, July 1968.

110. Crowther, D. L. and Harless, W. H., Jr.: Effects of Trapped Radiation on Spacecraft Systems. Section 8 of Trapped Radiation Handbook, Defense Nuclear Agency, DNA 2524H, December 1971.

111. Dye, D. L.: Current Status of Space Radiation Effects in Materials and Components. Proceedings of Symposium on Protection Against Space Radiation, NASA SP-169, 1968, pp. 19-32.

112. Vette, J. I.: Models of the Trapped Radiation Environment, Vol. I: Inner Zone Protons and Electrons. NASA SP-3024, Vol. I, 1966.

113. Vette, J. I.; Lucero, A. B.; and Wright, J. A.: Models of the Trapped Radiation Environment, Vol. III: Electrons at Synchronous Altitudes. NASA SP-3024, Vol. III, 1967.

114. Singley, G. W. and Vette, J. I.: A Model Environment for Outer Zone Electrons. NASA GSFC National Space Science Data Center, NSSDC 72-13, December 1972.

115. Teague, M. J. and Vette, J. I.: The Use of the Inner Zone Electron Model AE-5 and Associated Computer Programs. NASA GSFC National Space Science Data Center, NSSDC 72-11, November 1972.

116. King, J. H.: Models of the Trapped Radiation Environment, Vol. IV: Low Energy Protons. NASA SP-3024, Vol. IV, 1967.

117. Lavine, J. P. and Vette, J. I.: Models of the Trapped Radiation Environment, Vol. V: Inner Belt Protons. NASA SP-3024, Vol. V, 1969.

118. Lavine, J. P. and Vette, J. I.: Models of the Trapped Radiation Environment, Vol. V: Inner Belt Protons. NASA SP-3024, Vol. VI, 1970.

119. Teague, M. J. and Vette, J. I.: A Model of the Trapped Electron Population for Solar Minimum, NASA, GSFC, NSSDC 74-03, April 1974.

120. King, J. H.; and Stassinopoulos, E. G.: Energetic Solar Proton Vs Terrestrially-Trapped Proton Fluxes for Active Years 1977-1983, NASA GSFC X-601-74-221, 1974 (to be published in Journal of Spacecraft and Rockets in 1975).

121. Kluge, G. and Lenhart, K. G.: A Unified Computing Procedure for Trapped Radiation Models. ESRO European Space Operations Centre, ESOC Internal Note No. 78, March 1971.

NASA SPACE VEHICLE DESIGN CRITERIA MONOGRAPHS

ENVIRONMENT

SP-8005	Solar Electromagnetic Radiation, revised May 1971
SP-8010	Models of Mars' Atmosphere (1974) revised December 1974
SP-8011	Models of Venus Atmosphere (1972), revised September 1972
SP-8013	Meteoroid Environment Model–1969 (Near Earth to Lunar Surface), March 1969
SP-8017	Magnetic Fields–Earth and Extraterrestrial, March 1969
SP-8020	Mars Surface Models (1968), May 1969
SP-8021	Models of Earth's Atmosphere (90 to 2500 km), revised March 1973
SP-8023	Lunar Surface Models, May 1969
SP-8037	Assessment and Control of Spacecraft Magnetic Fields, September 1970
SP-8038	Meteoroid Environment Model–1970 (Interplanetary and Planetary), October 1970
SP-8049	The Earth's Ionosphere, March 1971
SP-8067	Earth Albedo and Emitted Radiation, July 1971
SP-8069	The Planet Jupiter (1970), December 1971
SP-8084	Surface Atmospheric Extremes (Launch and Transportation Areas), revised June 1974
SP-8085	The Planet Mercury (1971), March 1972
SP-8091	The Planet Saturn (1970), June 1972
SP-8092	Assessment and Control of Spacecraft Electromagnetic Interference, June 1972
SP-8103	The Planets Uranus, Nepture, and Pluto (1971), November 1972

SP-8105	Spacecraft Thermal Control, May 1973
SP-8111	Assessment and Control of Electrostatic Charges, May 1974
SP-8116	The Earth's Trapped Radiation Belts, March 1975
SP-8118	Interplanetary Charged Particles, March 1975

STRUCTURES

SP-9011	Buffeting During Atmospheric Ascent, revised November 1970
SP-8002	Flight-Loads Measurements During Launch and Exit, revised June 1972
SP-8003	Flutter, Buzz, and Divergence, July 1964
SP-8004	Panel Flutter, revised June 1972
SP-8006	Local Steady Aerodynamic Loads During Launch and Exit, May 1965
SP-8007	Buckling of Thin-Walled Circular Cylinders, revised August 1968
SP-8008	Prelaunch Ground Wind Loads, November 1965
SP-8009	Propellant Slosh Loads, August 1968
SP-8012	Natural Vibration Modal Analysis, September 1968
SP-8014	Entry Thermal Protection, August 1968
SP-8019	Buckling of Thin-Walled Truncated Cones, September 1968
SP-8022	Staging Loads, February 1969
SP-8029	Aerodynamic and Rocket-Exhaust Heating During Launch and Ascent, May 1969
SP-8031	Slosh Suppression, May 1969
SP-8032	Buckling of Thin-Walled Doubly Curved Shells, August 1969
SP-8035	Wind Loads During Ascent, June 1970
SP-8040	Fracture Control of Metallic Pressure Vessels, May 1970

SP-8042	Meteoroid Damage Assessment, May 1970
SP8043	Design–Development testing, May 1970
SP-8044	Qualification testing, May 1970
SP-8045	Acceptance testing, April 1970
SP-8046	Landing Impact Attenuation for Non-Surface-Planning Landers, April 1970
SP-8050	Structural Vibration Prediction, June 1970
SP-8053	Nuclear and Space Radiation Effects on Materials, June 1970
SP-8054	Space Radiation Protection, June 1970
SP-8055	Prevention of Coupled Structure-Propulsion Instability (Pogo), October 1970
SP-8056	Flight Separation Mechanisms, October 1970
SP-8057	Structural Design Criteria Applicable to a Space Shuttle, revised March 1972
SP-8060	Compartment Venting, November 1970
SP-8061	Interaction with Umblicals and Launch Stand, August 1970
SP-8062	Entry Gasdynamic Heating, January 1971
SP-8063	Lubrication, Friction, and Wear, June 1971
SP-8066	Deployable Aerodynamic Deceleration Systems, June 1971
SP-8068	Buckling Strength of Structural Plates, June 1971
SP-8072	Acoustic Loads Generated by the Propulsion System, June 1971
SP-8077	Transportation and Handling Loads, September 1971
SP-8079	Structural Interaction with Control Systems, November 1971
SP-8082	Stress-Corrosion Cracking in Metals, August 1971
SP-8083	Discontinuity in Metallic Pressure Vessels, November 1971

SP-8095 Preliminary Criteria for the Fracture Control of Space Shuttle Structures, June 1971

SP-8099 Combining Ascent Loads, May 1972

GUIDANCE AND CONTROL

SP-8015 Guidance and Navigation for Entry Vehicles, November 1968

SP-8016 Effects of Structural Flexibility on Spacecraft Control Systems, April 1969

SP-8018 Spacecraft Magnetic Torques, March 1969

SP-8024 Spacecraft Gravitational Torques, May 1969

SP-8026 Spacecraft Star Trackers, July 1970

SP-8027 Spacecraft Radiation Torques, October 1969

SP-8028 Entry Vehicle Control, November 1969

SP-8033 Spacecraft Earth Horizon Sensors, December 1969

SP-8034 Spacecraft Mass Expulsion Torques, December 1969

SP-8036 Effects of Structural Flexibility on Launch Vehicle Control Systems, February 1970

SP-8047 Spacecraft Sun Sensors, June 1970

SP-8058 Spacecraft Aerodynamic Torques, January 1971

SP-8059 Spacecraft Attitude Control During Thrusting Maneuvers, February 1971

SP-8065 Tubular Spacecraft Booms (Extendible, Reel Stored), February 1971

SP-8070 Spaceborne Digital Computer Systems, March 1971

SP-8071 Passive Gravity-Gradient Libration Dampers, February 1971

SP-8074 Spacecraft Solar Cell Arrays, May 1971

SP-8078 Spaceborne Electronic Imaging Systems, June 1971

SP-8086 Space Vehicle Displays Design Criteria, March 1972

SP-8096	Space Vehicle Gyroscope Sensor Applications, October 1972
SP-8098	Effects of Structural Flexibility on Entry Vehicle Control Systems, June 1972
SP-8102	Space Vehicle Accelerometer Applications, December 1972

CHEMICAL PROPULSION

SP-8025	Solid Rocket Motor Metal Cases, April 1970
SP-8039	Solid Rocket Motor Performance Analysis and Prediction, May 1971
SP-8041	Captive-Fired Testing of Solid Rocket Motors, March 1971
SP-8048	Liquid Rocket Engine Turbopump Bearings, March 1971
SP-8051	Solid Rocket Motor Igniters, March 1971
SP-8052	Liquid Rocket Engine Turbopump Inducers, May 1971
SP-8064	Solid Propellant Selection and Characterization, June 1971
SP-8073	Solid Propellant Grain Structural Integrity Analysis, June 1973
SP-8075	Solid Propellant Processing Factors in Rocket Motor Design, October 1971
SP-8076	Solid Propellant Grain Design and Internal Ballistics, March 1972
SP-8080	Liquid Rocket Pressure Regulators, Relief Valves, Check Valves, Burst Disks, and Explosive Valves, March 1973
SP-8081	Liquid Propellant Gas Generators, March 1972
SP-8087	Liquid Rocket Engine Fluid-Cooled Combustion Chambers, April 1972
SP-8088	Liquid Rocket Metal Tanks and Tank Components, May 1974
SP-8090	Liquid Rocket Actuators and Operators, May 1973
SP-8094	Liquid Rocket Valve Components, August 1973
SP-8097	Liquid Rocket Valve Assemblies, November 1973
SP-8100	Liquid Rocket Engine Turbopump Gears, March 1974
SP-8101	Liquid Rocket Engine Turbopump Shafts and Couplings, September 1972
SP-8110	Liquid Rocket Engine Turbines, January 1974

NASA-Langley, 1975